Titre: Title:	Uncertainty of Form and Size Measurement with On-Machine Tool Metrology
Auteur: Author:	Saeid Sepahi Boroujeni
Date:	2021
Type:	Mémoire ou thèse / Dissertation or Thesis
Référence: Citation:	Sepahi Boroujeni, S. (2021). Uncertainty of Form and Size Measurement with On-Machine Tool Metrology [Thèse de doctorat, Polytechnique Montréal]. PolyPublie. https://publications.polymtl.ca/6624/

POLYTECHNIQUE MONTRÉAL

affiliée à l'Université de Montréal

UNCERTAINTY OF FORM AND SIZE MEASUREMENT WITH ON-MACHINE TOOL METROLOGY

SAEID SEPAHI BOROUJENI

Département de Génie Mécanique

Thèse présentée en vue de l'obtention du diplôme de *Philosophie Doctor*

Génie Mécanique

Mai 2021

POLYTECHNIQUE MONTRÉAL

affiliée à l'Université de Montréal

Cette thèse intitulée:

UNCERTAINTY OF FORM AND SIZE MEASUREMENT WITH ON-MACHINE TOOL METROLOGY

présentée par **Saeid SEPAHI BOROUJENI**

en vue de l'obtention du diplôme de Philosophie Doctor

a été dûment acceptée par le jury d'examen constitué de :

Sofiane ACHICHE, président
René MAYER, membre et directeur de recherche
Farbod KHAMENEIFAR, membre et codirecteur de recherche
James GOULET, membre
José Antonio YAGÜE-FABRA, membre externe

ACKNOWLEDGEMENTS

I express my sincere gratitude towards

my directors, Professors René Mayer and Farbod Khameneifar, who were always there for me, tolerated my sense of adventure, and gave me the opportunity to learn from my mistakes;

the technicians of the Virtual Manufacturing Research Laboratory (VMRL), Mr. Guy Gironne, Mr. Vincent Mayer, and Mr. François Ménard, who were always welcoming and worked closely with me;

my friends, Dr. Kanglin Xing, Dr. Sareh Esmaeili, Dr. Elie Bitar-Nehme, Babak Beglarzadeh, and Hamid Ghaderi, who gave me their generous support;

the members of the jury, Professors Sofiane Achiche, James Goulet, and José Antonio Yagüe-Fabra for their precious time to evaluate this dissertation;

my family, my endless source of courage and inspiration;

and my sweetheart, Darly François-Gélin, who surrounded me with her genuine love.

RÉSUMÉ

Équipée d’un palpeur, une machine-outil devient également capable de servir d'appareil de mesure. Cela augmente à la fois l'efficacité et la précision de la fabrication et rend la machine-outil compétente pour remplacer la machine à mesurer tridimensionnelle. Bien qu'efficace, l'utilisation de machines-outils pour la mesure en cours de processus pose le défi de la traçabilité métrologique. L'évaluation de l'incertitude est le seul moyen de relever ce défi. Malgré l'utilisation croissante des techniques de mesure sur machines-outils, les informations sur son incertitude sont confinées aux méthodes spécifiquement développées pour les machines à mesurer tridimensionnelles, en particulier ISO 15530-3.

Cette étude concerne l'évaluation de l'incertitude des résultats de la mesure sur machine- outil avec une méthode de covariance sans utiliser d’étalon, contrairement à l'instruction spécifiée par l'ISO 15530-3. Le schéma d'évaluation de l'incertitude comprend deux approches principales, soit un estimateur de Monte Carlo adaptatif et un estimateur dans le cadre du Guide pour l'Expression de l'incertitude de mesure (GUM). La fonction de mesure pour le palpage sur machine-outil est le modèle cinématique de la machine-outil à cinq axes, qui reçoit cinq positions des axes et treize erreurs géométriques de la machine en tant que grandeurs d'entrée et renvoie trois coordonnées cartésiennes de la position compensée dans le repère de la pièce. En conséquence, la fonction de densité jointe requise pour démarrer la méthode de Monte Carlo adaptative encode les informations statistiques de ces grandeurs d'entrée.

La répétabilité des positions d’axe saisies détermine une partie de leurs incertitudes sous la forme d'une matrice de covariance. En faisant varier les positions des cinq axes de la machine et des deux composantes du vecteur unitaire d’approche, les mesures répliquées sur machine-outil sur deux sphères de précision donnent la variance et la covariance des positions enregistrées des articulations qui sont utilisées pour ajuster un modèle de répétabilité. Des expériences séparées sur une jauge annulaire déterminent les effets potentiels de l'orientation du palpage, de l'hystérésis du système, de la stratégie de la mesure et de la durée de la tâche sur la répétabilité de la mesure.

Puis, un simulateur de Monte Carlo adaptatif estime l’incertitude des treize erreurs géométriques de la machine avec l’artefact de l’échelle et des billes de référence. L’identification quotidienne (une fois par jour) des erreurs avec cette méthode donne des échantillons des centres des billes

mesurés sur machine-outil variant sur le long terme, dont la fonction de densité jointe est la grandeur d’entrée de l'estimateur de l'incertitude des paramètres de la machine. Cet évaluateur de l'incertitude valide également une méthode dans le cadre du GUM (« GUM uncertainty framework ») comme alternative efficace à l'approche de Monte Carlo qui exige beaucoup de temps de traitement.

Les matrices de covariance des positions d’axe enregistrées et celle des paramètres de la machine s’assemblent dans un simulateur de covariance. La matrice de covariance assemblée lance un estimateur Monte Carlo adaptif distinct basé sur le modèle cinématique de la machine, qui estime l’incertitude associée à la position compensée d’un ensemble de points. L'incertitude peut se propager plus à travers une fonction de GD&T et produire l'incertitude standard de propriétés géométriques. La mesure sur machine-outil des étalons à différentes positions d’axe de la machine valide le schéma d’incertitude développé. Enfin, une méthode de GUM validée avec l'estimateur de l'incertitude de Monte Carlo remplace cette dernière et augmente considérablement l'efficacité de l'évaluation de l'incertitude.

ABSTRACT

Equipped with a touch probe, a machine tool becomes able to serve as a measuring device, as well. This promotes both the efficiency and accuracy of manufacture and makes the machine tool competent to replace the coordinate-measuring machine. Although efficient, the use of machine tools for in-process measurement raises the challenge of measurement traceability. The uncertainty evaluation is the only means to address this challenge. Despite the growing use of the on-machine measurement techniques, the guidelines on its uncertainty have mostly remained confined to the standards specifically developed for coordinate-measuring machines, particularly ISO 15530-3.

This study concerns the uncertainty evaluation of the on-machine measurement results with a full-covariance matrix method without using a calibrated reference, unlike the instruction specified in ISO 15530-3. The uncertainty evaluation scheme includes two main approaches, an adaptive Monte Carlo estimator and the GUM framework. The measurement function in on-machine probing is the forward kinematic model of a five-axis machine tool, which receives five probed joint positions and thirteen geometric errors of the machine as input quantities and returns three Cartesian coordinates of the compensated position in the workpiece frame. Accordingly, the joint distribution required to start the adaptive Monte Carlo method encodes the requisite statistical information of these input variables.

The repeatability of the probed axis positions determines, in part, their uncertainty in the form of a covariance matrix. By varying the positions of the machine's axes and two components of the unit approach vector, replicated on-machine probing on two precision spheres gives the variance and covariance of the recorded joint positions to fit the repeatability model. Separate experiments on a ring gauge determine the potential effects on the probing repeatability of the probe orientation, system's hysteresis, measurement strategy, and task period.

Then, a Monte Carlo simulator estimates the uncertainty of thirteen geometric errors of the machine using the scale and master ball artifact. A day-to-day (once a day) error identification with this method gives samples of the on-machine probed ball centres varying over the long-term (15 days), whose joint distribution is the input of the uncertainty estimator of the machine parameters. This uncertainty evaluator also validates a GUM-framework method as an efficient alternative to the time-consuming Monte Carlo approach.

The covariance matrices of the recorded axis positions and the machine parameters assemble in a covariance matrix simulator. The assembled covariance matrix initiates a separate Monte Carlo estimator based on the machine's forward kinematic model, which evaluates the uncertainty associated with the compensated position of a probed point set. The uncertainty can propagate further through any GD&T function and yield the standard uncertainty of desirable geometric features. The on-machine measurement of calibrated references at various positions of the machine's axes validates the developed uncertainty scheme. Finally, a separate GUM framework, validated with the Monte Carlo uncertainty estimator, replaces this method and highly increases the efficiency of uncertainty assessment.

TABLE OF CONTENTS

ACKNOWLEDGEMENTS III

RÉSUMÉ IV

ABSTRACT VI

TABLE OF CONTENTS VIII

LIST OF TABLES XII

LIST OF FIGURES XIV

LIST OF SYMBOLS AND ABBREVIATIONS XXI

CHAPTER 1 : INTRODUCTION 1

1.1 Research problem 1

1.2 Objectives 2

1.3 Impact 2

1.4 Assumptions 3

CHAPTER 2 : LITERATURE REVIEW 4

2.1 On-machine measurement 4

2.2 Measurement uncertainty 9

2.3 Evaluation of measurement uncertainty 12

CHAPTER 3 : METHODOLOGY AND SYNTHESIS 23

3.1 Methodology 23

3.1.1 Uncertainty estimation schemes 23

3.1.2 On-machine probing repeatability 24

3.1.3 Machine geometric errors and associated uncertainty 24

3.1.4 Covariance of input quantities 25

3.1.5 Uncertainty assessment in on-machine probing and GD&T 25

3.2 Dissertation synthesis 25

CHAPTER 4 : ARTICLE 1: REPEATABILITY OF ON-MACHINE PROBING BY A FIVE-AXIS MACHINE TOOL 29

4.1 Abstract 29

4.2 Introduction 30

4.3 Methods and materials 34

4.4 Repeatability of on-machine probing 35

4.5 Hysteresis of the measurement system 39

4.6 Probing strategy and time span 41

4.7 Results and discussion 42

4.7.1 Probe orientation 42

4.7.2 Repeatability models of on-machine measurements 43

4.7.3 Probing hysteresis test and axis hysteresis test 58

4.7.4 Probing strategy and time span 60

4.8 Conclusions 64

4.9 Acknowledgements 65

4.10 Appendix A. Examples of data analysis 65

4.10.1 Standard deviation and covariance evaluation in the five-axis ball test 65

4.10.2 Hysteresis evaluation 67

4.10.3 Evaluation of probing strategy and time span effects 67

CHAPTER 5 : ARTICLE 2: EFFICIENT UNCERTAINTY ESTIMATION OF INDIRECTLY MEASURED GEOMETRIC ERRORS OF FIVE-AXIS MACHINE TOOLS VIA MONTE-CARLO VALIDATED GUM FRAMEWORK 69

5.1 Abstract 69

5.2 Introduction 70
5.3 Geometric error evaluation 74
5.4 Uncertainty estimation 78
5.5 Adaptive Monte Carlo method 78
5.6 GUM uncertainty framework 82
5.7 Results and discussion 83
5.8 Conclusions 93
5.9 Acknowledgments 94
CHAPTER 6 : ARTICLE 3: A FULL COVARIANCE MATRIX METHOD FOR UNCERTAINTY ASSESSMENT IN ON-MACHINE PROBING 95
6.1 Abstract 95
6.2 Introduction 96
6.3 Uncertainty estimation with an adaptive Monte Carlo method 99
6.3.1 Adaptive Monte Carlo method 100
6.3.2 Covariance of input quantities 102
6.3.3 Volumetric errors unexplained by SAMBA 110
6.4 Experimental verification 111
6.5 Results and discussion 114
6.5.1 Gauge block 114
6.5.2 Precision sphere 117
6.5.3 Verification of the uncertainty estimator 120
6.6 Summary and conclusions 123
6.7 Acknowledgements 124
6.8 Annex A. Positions of the machine’s rotary axes in validation experiments 124

CHAPTER 7 : PROMPT UNCERTAINTY ESTIMATION WITH GUM FRAMEWORK FOR ON-MACHINE TOOL COORDINATE METROLOGY 125

7.1 Uncertainty evaluation 126

7.1.1 Measurement function, input, and output quantities 126

7.1.2 Monte Carlo method 127

7.1.3 GUM uncertainty framework 127

7.2 Validation of GUF with an adaptive Monte Carlo method 129

7.3 Results and discussions 130

7.4 Summary and Conclusions 132

CHAPTER 8 : GENERAL DISCUSSION 135

CHAPTER 9 : CONCLUSIONS AND FUTURE WORKS 137

9.1 General conclusions 137

9.2 Future works 138

REFERENCES 140

LIST OF TABLES

Table 4-1: Variation ranges of the experimental factors in the repeatability evaluation of on-machine measurements. 38

Table 4-2: Validation of the standard deviation models of on-machine measurements. 47

Table 4-3: The average of standard deviation and the average of absolute gradient of the standard deviation model with respect to the experimental factors. For each row, the variable other than the indicated factor is fixed so that the machine axes are fixed at their central values (Table 4-1) and the approach direction is [φ,θ]=[45°,45°]. 49

Table 4-4: Validation of the covariance models of on-machine measurements. 55

Table 4-5: The average of standard deviation and the average of absolute gradients of the covariance with respect to the experimental factors. For each row the variable other than the indicated factor is fixed so that the machine axes are fixed at their central values (Table 4-1) and the approach direction is [φ, θ]=[45°, 45°].....57

Table 5-1: Geometric errors of the machine tool according to the nomenclature specified in [102]. The first subscript is the nature of the error, the numeral 0 (zero) as the middle subscript indicates that it is an axis position or an orientation error (not an error motion) and the third subscript is the axis of motion with this error. 77

Table 5-2: Error estimates y and standard uncertainty u_y evaluated by the adaptive MCM, the experimental replications (Exp.) and GUF (results with one digit more than the number of significant digits presented in Table 5-1). 86

Table 5-3: The maximum eigenvalue $\lambda_{\max}$ of the correlation matrix and coverage factor k_p of hyper-ellipsoidal coverage region for coverage probability 0.95 obtained by the adaptive MCM, the experimental replications (Exp.), and GUF. 86

Table 5-4: Superposition of the correlation and the covariance matrices obtained by the adaptive MCM. The upper triangular part of the matrix includes the correlation coefficients and the lower triangular part together with the diagonal elements include the covariance values. The color spectrum denotes the absolute values of the correlation coefficients. 88

Table 6-1: Geometric errors of the machine tool according to the nomenclature specified in [102]. The first subscript is the nature of the error, the numeral 0 (zero) as the middle subscript indicates that it is an axis position or orientation error (not an error motion) and the third subscript is the axis of motion with this error. 101

Table 6-2: Standard deviation (Std.) of: estimates y, standard uncertainties u_y, maximum eigenvalue $\lambda_{\max}$ of the associated correlation coefficient matrix, and coverage factor k_p after h=10 sequences (M=10^5 trials) of MCM for the six coordinates of a point set collected on the gauge block and for its length estimate. 121

Table 7-1: The adaptive MCM and GUF results for best estimates y and associated standard uncertainty $u(y)$ together with their absolute differences obtained for the compensated coordinates of two points probed on a gauge block and its estimated length. 132

Table 7-2: The adaptive MCM and GUF results for the largest eigenvalue $\lambda_{\max}$ of the output correlation matrix and coverage factor k_p along with their absolute differences obtained for the compensated coordinates of two points and the estimated length listed in Table 7-1. ..132

LIST OF FIGURES

Figure 2-1: Steps of on-machine measurement [13]. 5

Figure 2-2: Principles of the workpiece-referred control system. If the tool-holder moves towards or away from the workpiece, the microtool servo compensates the movement [19]. 6

Figure 2-3: Schematic illustration of the compensation for systematic error. 10

Figure 2-4: Dependence of the tolerance zone on measurement uncertainty [43]. 11

Figure 2-5: a) Propagation of possible values ξ_i of X_i through measurement function f and the creation of the output's distribution describing the possible values η of Y, and b) the normal PDF for output quantity Y. Best estimate y of measurand Y is assumed to be the expected value of Y. The standard deviation is the standard uncertainty $u(y)$ associated with y. The expanded uncertainty U includes 95% of possible values of y, corresponding to a coverage factor of 2 [49]. 15

Figure 2-6: a) The application of MCM for the approximation of the value of π; a) 2000 points chosen at random within a unit square illustrated in different colours, denoting whether they lie in the quarter circle or not, and b) estimate of π converging to its true value by increasing the number of MCM trials. 17

Figure 3-1: Data flow in the uncertainty assessment in on-machine measurement. Also shown are best estimates and the covariance matrices obtained at certain steps when processing a point set of size n. 27

Figure 3-2: Synthesis of Chapters four to seven and the subjects covered by each chapter. 28

Figure 4-1: On-machine probing and the uncertainty evaluation of measurement results. In orange, the subject addressed in this paper. 35

Figure 4-2: a) Experimental setup of five-axis ball tests including the precision spheres and the touch-trigger probe mounted on the five-axis machine tool. b) The target pose coordinates X_{T}, Y_{T}, and Z_{T} in the machine frame as well as the indexations of rotary axes B_{T} and C_{T} considered as machine factors in the design of experiments for the repeatability evaluation of on-machine measurements. Also shown are c) the polar φ and azimuthal angle θ of the

approach direction, and d) the probing strategy of the probe orientation tests used to study the effects of probe orientation ω, around the probe axis, on measurement repeatability. 38

Figure 4-3: Schematic illustration of the effect of relative translation of the tool with respect to the workpiece on the approach distance along the nominal approach direction. 39

Figure 4-4: Target points in a) the probing hysteresis and axis hysteresis tests (For the axis hysteresis tests, only the target points at $\psi = 0°, 90°, 180°,$ and $270°$ were probed), and b) the simple, shuffled and ordered ring gauge. 41

Figure 4-5: Measurement strategy adopted in each cycle of a) the probing hysteresis test and b) the axis hysteresis test. After each measurement, the probe retracts to the ring centre. 41

Figure 4-6: The repeatability of on-machine measurements versus the probe orientation ω in the probe orientation tests (Figure 4-2d). 43

Figure 4-7: Typical X and Y coordinates recorded in the replicate measurements for the five-axis ball tests obtained for nominal target pose $X_T = -68.8$, $Y_T = 69.7$, $Z_T = 110.6$, $B_T = -54°$, $C_T = -180°$, $\varphi = 90°$ and $\theta = 144°$. The polar angle of the approach direction is $\varphi = 90°$, thus the probe moves in the XY plane resulting in no variation in Z coordinate. 44

Figure 4-8: Regression plots of the values measured versus the values predicted by the probing standard deviation models for: a) the X coordinate, b) the Y coordinate, and c) the Z coordinate. The non-filled and filled markers represent the measurement results used to fit and to validate the probing repeatability models, respectively. The residual histograms obtained by fitting the standard deviation models to the: d) X coordinate, e) Y coordinate, and f) Z coordinate. Normal probability plots obtained for the recorded g) X coordinate, h) Y coordinate, and i) Z coordinate. 46

Figure 4-9: Regression plot of the values measured versus the values predicted by the probing standard deviation model a) perpendicular to the target surface and b) tangent to the target surface. The non-filled and filled markers represent the measurement results used to fit and to validate the probing repeatability models, respectively. The residual histograms obtained by fitting the standard deviation model c) perpendicular to the target surface and d) tangent to the

target surface. Normal probability plot e) perpendicular to the target surface and f) tangent to the target surface 47

Figure 4-10: The standard deviation of on-machine measurements versus the positions of the workpiece branch axes: a-c) B and C; d-f) B and X; and g-i) X and C. The other independent parameters are fixed at their central values (Table 4-1) and the approach direction is [φ,θ]=[45°,45°]. 50

Figure 4-11: The standard deviation of on-machine measurements versus the positions of the tool branch axes Z and Y. The other independent parameters are fixed at their central values (Table 4-1) and the approach direction is [φ,θ]=[45°,45°]. 51

Figure 4-12: The polar plots of the standard deviation predictions from the model versus the polar φ and azimuthal θ angle of the approach direction for the a) X coordinate, b) Y coordinate, c) Z coordinate, d) normal (radial) projection, and e) tangential projection of the Cartesian readings. The other independent parameters are fixed at their central values (Table 4-1). ...52

Figure 4-13: Regression plots of the values measured versus the values predicted by the covariance models between: a) the X and Y coordinates cov(X,Y), b) the X and Z coordinates cov(X,Z), and c) the Y and Z coordinates cov(Y,Z). The non-filled and filled markers represent the measurement results used to fit and to validate the covariance models, respectively. The residual histograms obtained by fitting the models to the: d) cov(X,Y), e) cov(X,Z), and f) cov(Y,Z). Normal probability plots obtained for the measured g) cov(X,Y), h) cov(X,Z), and i) cov(Y,Z). 54

Figure 4-14: a) Regression plot of the values measured versus the values predicted by the covariance model between the values projected perpendicular to the target surface and tangent to the target surface cov(N,T). The non-filled and filled markers represent the measurement results used to fit and to validate the covariance models, respectively. b) The residual histograms obtained by fitting the model and c) corresponding normal probability plot. 55

Figure 4-15: The polar plots of the absolute values of covariance predictions from the model versus the polar φ and azimuthal θ angle of the approach direction for the a) cov(X, Y), b) cov(X, Z), c) cov(Y, Z) and, d) cov(N, T). The other independent parameters are fixed at their central values (Table 4-1).....57

Figure 4-16: a) Polar presentation of the differences between the radii measured for indexations $\psi = 0°, 30°, \ldots, 330°$ (Figure 4-4a), with and without hysteresis being involved; b) hysteresis errors identified for each indexation together with the associated standard uncertainty, and c) the standard deviations of the radial projections recorded for each indexation. 59

Figure 4-17: a) Hysteresis errors of machine axes X and Y with premovements along the positive and negative directions of the cross axis together with the associated standard uncertainty and b) the standard deviations of probing results with the premovements. 59

Figure 4-18: Typical trends of replicate measurements done in different ring gauge tests along with temperature variations measured during the shuffled and ordered tests. The presented data is the normal (radial) projections recorded at 90° ($\psi_0 = 7.5°$ in Figure 4-4b). 61

Figure 4-19: The repeatability of on-machine measurements obtained based on the fitting residuals in the ordered and shuffled ring gauge tests for a) the X coordinate, b) the Y coordinate, and c) the normal projection of the Cartesian readings at the 24 points (with $\psi_0 = 7.5°$ in Figure 4-4b). The angle ψ (Figure 4-4b) corresponding to each indexation in Figure 4-4b is shown on top of each graph. 62

Figure 4-20: The probing repeatability along the X and Y axes by sliding a 10-iteration wide frame between the 26th and the 50th iterations shown in Figure 4-18. Results obtained through the a) simple, b) ordered, and c) shuffled ring gauge tests. 62

Figure 4-21: 50 replicate measurements recorded in simple ring gauge test with an approach direction lying in the XY plane of the machine frame and making an angle of a) 67.5° and b) 262.5° with the positive direction of the X-axis of the machine (δ=0.5 μm is the machine resolution and the labels indicate the number of duplicate results). 63

Figure 5-1: a) Experimental setup of SAMBA on a Mitsui Seiki HU40-T machine tool equipped with a Renishaw® MP 700 touch-trigger probe. b) Schematic of the five-axis machine tool with topology WCBXFZYST (W: workpiece; C and B: rotary axes around axes Z and Y, respectively; X, Y, and Z: machine linear axes; F: foundation; S: spindle, and T: tool). 77

Figure 5-2: Flowcharts of a) SAMBA calibration process and b) uncertainty evaluation by means of the adaptive Monte Carlo. 78

Figure 5-3: Numerical differentiation of the SAMBA calibration function at $\boldsymbol{X} = \boldsymbol{x}$ with respect to X_j, the jth input quantity. 82

Figure 5-4: Variations of the centre coordinates of ball 3 around their average (the zero line) measured in the experimental replications of SAMBA. 83

Figure 5-5: Error estimates (absolute values) and the associated standard uncertainty evaluated through the adaptive MCM. Errors are grouped into three categories; the angular errors, the translational errors, and the linear terms (slopes) of the linear positioning errors. 86

Figure 5-6: The gradient magnitudes of the geometric errors and their partial derivatives with respect to the SAMBA scale bar length. The green columns represent the absolute values of the partial derivatives whose numerical values are shown as data labels. 87

Figure 5-7: a) Ellipsoidal and rectangular coverage regions obtained by the experiments (Exp.), the adaptive MCM, and the GUF analyses for E_{XX1} and E_{YY1} (for coverage probability p =0.95) together with 2,000 points drawn at random from the joint PDF of the outputs and the 15 outputs obtained experimentally. b) 3D histogram of the outputs based on the adaptive MCM, and comparison between the adaptive MCM and the GUF histograms for c) E_{XX1} and d) E_{YY1}. 89

Figure 5-8: a) Ellipsoidal and rectangular coverage regions obtained by the experiments (Exp.), the adaptive MCM, and the GUF analyses for E_{C0B} and E_{C0Y} (for coverage probability p =0.95) together with 2,000 points drawn at random from the joint PDF of the outputs and the 15 outputs obtained experimentally. b) 3D histogram of the outputs based on the adaptive MCM, and comparison between the adaptive MCM and the GUF histograms for c) E_{C0B} and d) E_{C0Y}. 91

Figure 5-9: a) Ellipsoidal and rectangular coverage regions obtained by the experiments (Exp.), the adaptive MCM, and the GUF analyses for E_{Y0S} and E_{X0S} (for coverage probability p =0.95) together with 2,000 points drawn at random from the joint PDF of the outputs and the 15 outputs obtained experimentally. b) 3D histogram of the outputs based on the adaptive MCM, and comparison between the adaptive MCM and the GUF histograms for c) E_{Y0S} and d) E_{X0S}. 92

Figure 6-1: Data flow for the on-machine assessment of a geometric feature from a point set consisting of n probed points. The matrices in colour schematically represent the covariance matrices associated with the input and output quantities of the different steps. 100

Figure 6-2: Data flow of a) the covariance simulator for input quantities, which provides a full covariance matrix for b) the adaptive Monte Carlo method that evaluates a large sample of input quantities through c) the on-machine measurement function. 103

Figure 6-3: Data flow for the simulation of the covariance matrix of the input quantities consisting of probed axis positions $\boldsymbol{\Gamma}$ and machine parameters $\boldsymbol{\Delta}$. The process includes calculating compensated positions $\boldsymbol{\Psi}$ through forward kinematic model f with an estimate of current machine parameters $\boldsymbol{\delta}$, then simulating long-term repeatability of on-machine measurement by evaluating the compensated positions $\boldsymbol{\Psi}$ through the inverse kinematic model f^{-1} with a sample of machine parameters $\boldsymbol{\delta}^q$ $(q = 1, \dots, Q)$. For illustrative purposes, the distributions are univariate. 106

Figure 6-4: The data flow of the covariance simulation for a single-point probing on a single-axis (axis Φ) machine tool with a positioning error of δ. The green distribution describes the population of short-term repeatability of probed positions Φ (Population I). The purple histogram represents the population of corresponding compensated positions Ψ (Population II). The orange distribution describes the population of machine parameter Δ varying in the long-term (Population III). Evaluating Population II through the inverse kinematic model with population III gives the blue histogram representing the population of long-term repeatability of probed positions Γ (Population IV). Combining Populations III and IV provides a joint distribution for input random variables Γ and Δ. Analyzing the combined population reveals a correlation coefficient of -0.7, a high interdependence that is evident in the orientation of 2,000 random points drawn from the joint distribution. 109

Figure 6-5: The experimental procedure where a) a Mitsui Seiki HU40-T five-axis horizontal machining centre (shown with its axis location errors) measures b) a gauge block and c) a precision sphere. Also shown are d) the target points probed on the precision sphere and e) the calculation of the coverage probability in the experimental verification where the red area

is the coverage probability provided by the expanded uncertainty interval $y \pm U_y$ for measurand η. 113

Figure 6-6: a) Compensation error versus measurement error for 225 measured gauge's lengths, where the average expanded uncertainty interval is denoted by the blue zone, and b) 20 (out of 225) samples of the probed (before compensation) and compensated gauge's lengths with the associated expanded uncertainty (shown by error bars) and the calibrated length. 116

Figure 6-7: The compensated outputs with associated expanded uncertainties, the probed measurand (before compensation), and calibrated value of the measurand for a) the diameter and b) the sphericity of the precision sphere for each of 10 point sets. 118

Figure 6-8: The coverage probability, the average of output estimates (after compensation) with the associated average expanded uncertainties, the average of probed measurands (before compensation), and the calibrated value of the measurand vs. the number of pooled point sets k, shown for a) the diameter and b) the sphericity of the precision sphere. 120

Figure 7-1: a) Data flow for uncertainty assessment in on-machine measurement using an adaptive Monte Carlo method, and on-machine measurement of b) gauge block and c) precision sphere. 128

Figure 7-2: Numerical differentiation of the output quantities $\boldsymbol{Y}$ of on-machine measurement function at $\boldsymbol{X} = \boldsymbol{x}$ with respect to X_j, the j^{th} input quantity. 129

Figure 7-3: a-c) Ellipsoidal and rectangular coverage regions (for coverage probability p=0.95) obtained by the adaptive MCM and GUF for the compensated coordinates of a point probed on the gauge block. Also shown are 2,000 random output points. d-f) Comparison between the marginal histograms given by the adaptive MCM and GUF. 133

Figure 7-4: The computation time of GUF for uncertainty evaluation of the sphere's diameter from the point sets with different sizes and the time ratio of the adaptive MCM to GUF. 134

LIST OF SYMBOLS AND ABBREVIATIONS

List of symbols

$\boldsymbol{C_x}$	Sensitivity matrix of measurement model to input quantities	u_α	Uncertainty associated with thermal expansion coefficient α
$\boldsymbol{d}$	Uncalibrated dimensions of SAMBA	$u_{\Delta T}$	Uncertainty associated with temperature difference ΔT
$\boldsymbol{E}$	Vector $[\boldsymbol{e}_1, \dots, \boldsymbol{e}_n]^{\mathrm{T}}$ of unexplained volumetric errors associated with a point set of size n	X_i	i^{th} input quantity, regarded as a random variable
$\boldsymbol{e}_s$	Vector $[e_{\mathrm{X}}, e_{\mathrm{Y}}, e_{\mathrm{Z}}]^{\mathrm{T}}$ of unexplained volumetric error associated with the s^{th} point of a point set	$\boldsymbol{X}$	Vector $[X_1, \dots, X_N]^{\mathrm{T}}$ of input quantities
$f(\boldsymbol{X})$	Measurement (forward kinematic) model	$\boldsymbol{x}$	Estimate $[x_1, \dots, x_m]^{\mathrm{T}}$ of $\boldsymbol{X}$
$f^{-1}(\boldsymbol{X})$	Inverse kinematic model	Y_j	j^{th} output quantity, regarded as a random variable
$\boldsymbol{G_X}$	Matrix storing $\boldsymbol{x}_1, \dots, \boldsymbol{x}_M$	y_j	Estimate of Y_j
$\boldsymbol{G_Y}$	Matrix storing $\boldsymbol{y}_1, \dots, \boldsymbol{y}_M$	$\boldsymbol{Y}$	Vector $[Y_1, \dots, Y_m]^{\mathrm{T}}$ of output quantities
h	Number of MCM sequences	$\boldsymbol{y}$	Estimate $[y_1, \dots, y_m]^{\mathrm{T}}$ of $\boldsymbol{Y}$
$\boldsymbol{J}$	Sensitivity Jacobian matrix of residuals $\boldsymbol{r}$ to machine parameters $\boldsymbol{y}$	$\boldsymbol{y}^0$	Initial guess for Newton-Gauss solver in SAMBA calibration
$\boldsymbol{J}^+$	pseudoinverse matrix of $\boldsymbol{J}$	y_{cal}	Calibrated value of a measurand
k	Number of pooled point sets probed on the precision sphere	$y_{\mathrm{cal,20°C}}$	Calibrated value of a measurand indicated at 20°C
$\boldsymbol{L}$	Cholesky factor (upper triangular matrix)	$\boldsymbol{Z}$	Matrix consisting of M vectors drawn at random from a standard normal distribution
k_p	Coverage factor for a coverage region in the form of a hyper-ellipsoid for coverage probability p	α	Thermal expansion coefficient

List of symbols

m	Number of output quantities $Y_1, \dots, Y_m$	$\boldsymbol{\Gamma}$	Probed axis positions recorded in the long-term replications, regarded as a random variable
M	Number of MCM trials	$\boldsymbol{\xi}$	Vector $[\xi_1, \dots, \xi_N]^{\mathrm{T}}$ of random variables describing possible values of $\boldsymbol{X}$
n	Size of a probed point set	$\boldsymbol{\Delta}$	Machine parameters identified periodically in the long-term, regarded as a random variable
N	Number of input quantities $X_1, \dots, X_N$	$\boldsymbol{\delta}$	Best estimate of the machine parameters $\boldsymbol{\Delta}$ approximating the current values of machine parameters
p	Coverage probability	$\boldsymbol{\delta}^q$	Estimate of parameters $\boldsymbol{\Delta}$ during the q^{th} short-term pseudo-repeatability test
$\boldsymbol{P}_{\mathrm{ball}}$	SAMBA ball position in machine frame	$\boldsymbol{\sigma}$	Covariance matrix of the joint distribution of $\boldsymbol{\Delta}$
$\boldsymbol{P}_{\mathrm{tool}}$	Tool position in machine frame	$\boldsymbol{\delta y}$	Adjustments $[\delta y_1, \dots, \delta y_m]^{\mathrm{T}}$to output estimate $\boldsymbol{y}$
Q	Number of short-term pseudo-repeatability tests done in long-term	ΔT	Temperature difference between the calibration and measurement processes
q	Random variable	η	Random variable describing possible values of output quantity Y
$\boldsymbol{r}$	Residuals of tool position prediction relative to SAMBA ball position	δ	Dirac delta function
${}^{\mathrm{ball}}\boldsymbol{T}_{\mathrm{tool}}$	Homogeneous transformation matrix mapping positions from tool frame onto a SAMBA ball frame	$\boldsymbol{\tau}$	Convergence threshold of Newton-Gauss solver in SAMBA calibration
$\boldsymbol{U}_{\boldsymbol{x}}$	Covariance matrix associated with estimate $\boldsymbol{x}$ of input quantity $\boldsymbol{X}$	$\lambda_{\max}$	Largest eigenvalue of correlation matrix
$\boldsymbol{U}_{\boldsymbol{y}}$	Covariance matrix associated with estimate $\boldsymbol{y}$ of output quantity $\boldsymbol{Y}$	$\boldsymbol{\phi}$	Probed axis positions during a short-term repeatability test, regarded as a random variable

List of symbols

$\boldsymbol{u_y}$	Standard uncertainty associated with estimate $\boldsymbol{y}$ of output quantity $\boldsymbol{Y}$	$\boldsymbol{\varphi}$	Probed axis positions reported by the machine, regarded as a best estimated for $\boldsymbol{\phi}$
$u(x_j)$	Standard uncertainty associated with estimate x_j of input quantity X_j	$\boldsymbol{\phi^q}$	Probed axis positions during the q^{th} short-term pseudo-repeatability test, regarded as a random variable
$u(y_j)$	Standard uncertainty associated with estimate y_j of output quantity Y_j	$\boldsymbol{\varphi^q}$	Estimate of machine's axis positions $\boldsymbol{\phi}_q$
u_{cal}	Standard uncertainty associated with calibrated value y_{cal}	$\boldsymbol{v^q}$	Repeatability covariance matrix of the probed axis positions during the q^{th} short-term pseudo-repeatability test
$u_{\text{cal,20°C}}$	Standard uncertainty associated with calibrated value $y_{\text{cal,20°C}}$	$\boldsymbol{\Psi}$	Compensated positions in the workpiece frame, regarded as a random variable
$u(y_j)$	Standard uncertainty associated with estimate y_j of output quantity Y_j	$\boldsymbol{\psi}$	Best estimate of compensated positions $\boldsymbol{\Psi}$
		$\boldsymbol{w}$	Covariance matrix of the joint distribution of $\boldsymbol{\Psi}$

List of abbreviations

AFM	Atomic electron microscope	MCM	Monte Carlo method
CDF	Cumulative density function	OMV	On-machine verification
CMM	Coordinate-measuring machine	PDF	Probability density function
ECMM	Expert coordinate-measuring machine	RUMBA	reconfigurable uncalibrated master ball artifact
GD&T	Geometrical dimensioning and tolerancing	SAMBA	Scale and master ball artifact
GUF	GUM uncertainty framework	SEM	Scanning electron microscope
GUM	Guide to the expression of uncertainty in measurement	TANGO	Touch and go
HIPOSS	high-precision optical surface sensor	VIM	International vocabulary of metrology
HTM	Homogenous transformation matrix	WORFAC	workpiece-referred form accuracy control

CHAPTER 1 : INTRODUCTION

The synergy between measurement and manufacture is well established. A precise product is not obtainable unless with a capable measurement integrated into manufacture. A reliable measurement, however, dictates that the measurement section be isolated from the production line so that it functions under a strictly controlled environment. Therefore, merging these two tasks triggers both the challenge and opportunity of on-machine tool measurement, where the same machine performs the whole measurement and machining tasks, including probing a target point set on the machined part and the geometrical dimensioning and tolerancing (GD&T) confirmation. On-machine measurement increases efficiency by preventing inspection bottlenecks at the quality control section of the production process. This technique is also capable of meeting high-precision manufacturing requirements. On the other hand, the uncontrolled environment of the shop floor is associated with a wide range of influential factors contributing to measurement accuracy. Dividing these effects into systematic and random calls for detailed knowledge of the machine, workpiece, and environment. These factors are most likely correlated and sometimes inseparable due to their strongly coupled behaviour. Aiming at converting machine tools to coordinate-measuring machines (CMMs), researchers primarily resort to the existing standards for the uncertainty evaluation in CMMs. However, these specifications apply to stiff, precise, and environmentally isolated equipment and include a simplified methodology that neglects the correlations between the uncertainty contributors. Moreover, additional degrees of freedom provided by rotary axes of a machine tool bring about more complexity and imperfections.

1.1 Research problem

The current trend in the uncertainty evaluation of on-machine measurement results lies in the methods established specifically for the uncertainty evaluation in CMMs, such as those given in ISO 15530 [1, 2]. This study attends to three main concerns over this application. First, the differences between CMMs and machine tools regarding the working conditions, maintenance, and environment require detailed studies on dominant uncertainty contributors to on-machine measurement. Second, since the methodology specified in ISO 15530-3 [1] requires using a calibrated counterpart for the target part, fabricating and calibrating such a reference would be costly, especially for large part manufacture. Third, the methodology given in this standard

originates from the law of propagation of uncertainty specified by the Guide to the expression of uncertainty in measurement (GUM). This formulation, however, excludes any covariance effect between the input quantities, which can falsify uncertainty estimates.

1.2 Objectives

The main objective is to convert a machine tool to a traceable coordinate measuring machine (CMM). To approach this goal, considering the concerns clarified above, this research aims at meeting the following sub-objectives.

1- Define an uncertainty zone for all the points of a point set measured by a five-axis machine tool serving as a measuring device. The zone must establish the traceability of the measurement results. That is, true value of the measurand is likely to lie inside the zone with the desired probability.

2- Quantify the uncertainty sources that contribute to the uncertainty associated with the final probing results. The uncertainty contributors are much more diverse compared to those of CMMs kept under controlled environmental conditions.

3- Evaluate the correlation between the input quantities since the uncertainty sources are not necessarily independent and their correlations influence the uncertainty of measurement results.

4- Verify the uncertainty scheme through exemplary GD&T analysis.

1.3 Impact

One can consider implementing the methodology of this study to transform a machine tool into a traceable measuring device. Such an evolution would be achievable in a relatively short period and only by conducting inexpensive inspections on the machine tool. As a result of this project, any production line can be economically equipped with a reliable in-situ measuring device that considerably increases the efficiency and productivity of manufacturing cycle. Today, although CMMs are mostly inseparable from precision manufacturing, the future machine tools can independently cope with both the machining and measuring tasks, which gradually marginalizes CMMs owing to this study and similar research works. Moreover, the current research will be a benchmark for investigating more efficient and more accurate uncertainty estimators.

1.4 Assumptions

1- The machine's geometric errors used to compensate for the systematic effects are optimum.

2- The joint positions recorded through replicated probing tasks in the short and long term are distributed to normal distributions.

3- The variations of the machine's status remain within the range obtained by periodic monitoring over two weeks and they do not change dramatically in the course of this study.

CHAPTER 2 : LITERATURE REVIEW

2.1 On-machine measurement

The practice of integrating measurement into manufacture has brought about higher production efficiency. Thanks to this technique, the manufacturing process can readjust and adapt to changes in external conditions [3, 4]. Excluding capable measurement from manufacturing cycle dramatically reduces production efficiency. By its classical application, measurement within a manufacturing environment aims to provide a realization of a product's geometric features against its design drawings and specifications. Expert measurement directs industries towards high-precision manufacturing characterized by low batch, high variety, tight tolerance, and high-value products [5].

Owing to their capability and flexibility, CMMs play an important role in dimensional measurements [6]. Equipped with touch probes, machine tools also contribute to measurement procedures in different ways. They effectively respond to the needs of manual gauging through on-machine probing [7], where the operators of machine tools use this technique to position and align the machine's and the workpiece's datum. A machine tool also serves as a comparator between manufactured parts and their calibrated counterparts [8]. Today, however, the application of on-machine probing grows further to on-machine verification (OMV) [9], where the GD&T confirmation occurs in situ and on the machine.

Dimensional measurement can happen at different stages of a manufacturing line, from the initial alignment and setup of the part on the machine's table to the final part verification in the GD&T unit. Historically, manufacturers ensure the product quality only during the last step, i.e. the product measurement [10]. This "gate-keeping" strategy that stems from a defect detection (not prevention) policy, fails to guarantee or to enhance effectively product quality [8]. On the other hand, CMMs, which are known to be the only measurement apparatus capable of providing an acceptable level of uncertainty [11], should function independently of manufacturing department for metrological reasons. As a result, these precise systems are major sources of process bottleneck and inefficiency [9, 12]. Moreover, in the case of closed-loop manufacturing, delayed feedback from the measurement unit (or CMM) to the machining section notably decelerates the manufacturing cycle.

The idea of reducing the production's dependency on CMMs has triggered the idea of on-machine measurement whose steps are shown in Figure 2-1.

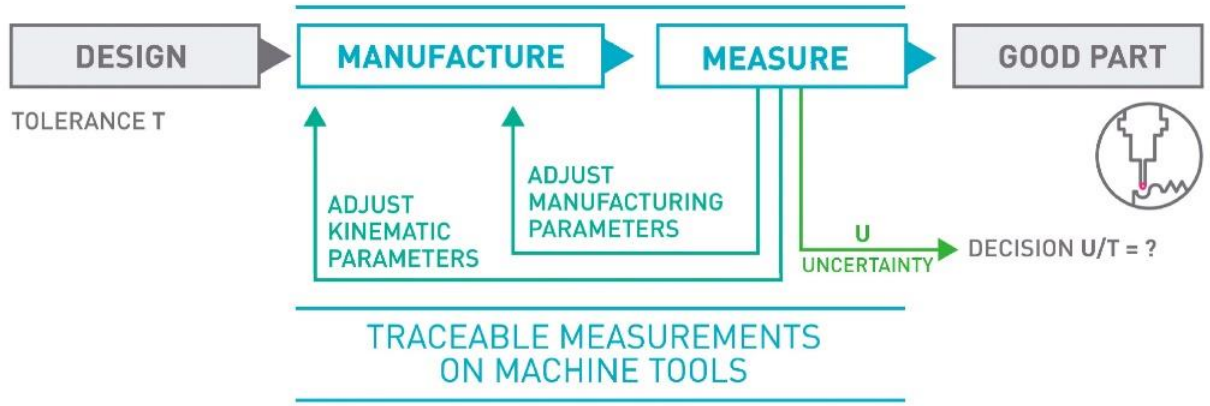

Figure 2-1: Steps of on-machine measurement [13].

On-machine measurement applications have emerged over the recent decades. Shiraishi summarizes the journey of on-machine measurement between the years 1961 and 1985 [14]. Yadayan and Burdekin review the applications of this method developed between 1986 and 1996 [15], and Vacharnukul and Kekid cover the advances introduced before 2003 [16]. In-process measurement for machining, including monitoring and control, becomes a research topic in 1989 [14, 17, 18]. At the same time, in-process measurement and workpiece-referred form accuracy control (WORFAC) improve the repeatability and stability of diamond turning processes [19]. In this system, unlike the conventional techniques that focus on mechanical elements of the machine, the controlling actions correspond to the real-time status of the workpiece. Using WORFAC, Kohno et al. [20] monitor the relative distance between the workpiece and the cutting tool to retain the desired accuracy (Figure 2-2). To read the distance, they use a high-precision optical surface sensor (HIPOSS), which works based on point autofocus with an accuracy of less than 1 nm. They adopt the same technique to create a freeform surface using an absolute reference.

In a closed-loop manufacturing system, the measurement unit provides feedback to apply an incremental modification of the process. Particularly, the measurement section of a production line can in situ evaluate the tool's condition, monitor the real-time tool-workpiece positioning (error

analysis), and measure the geometric features of the workpiece [21]. Certain methods of on-machine measurement call for external equipment such as sensors and interferometers. Others can come to function more easily by installing touch or non-touch probes on the machine.

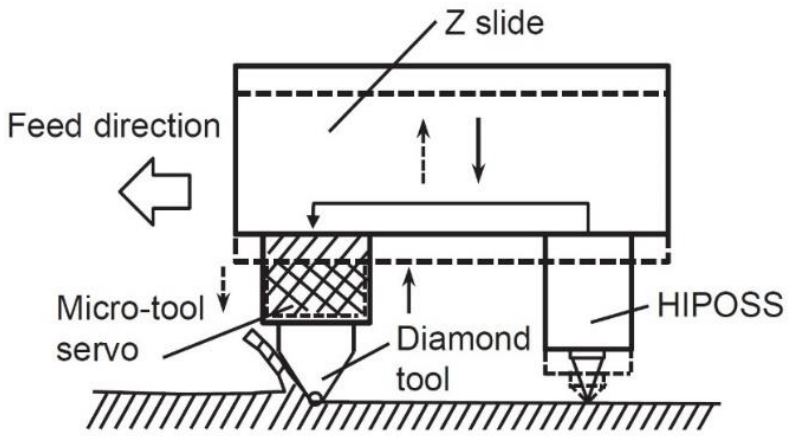

Figure 2-2: Principles of the workpiece-referred control system. If the tool-holder moves towards or away from the workpiece, the microtool servo compensates the movement [19].

On-machine measurement of a machine's geometric errors includes direct and indirect methods. Direct techniques attend to intrinsic errors of each of the machine's axis such as positioning and scaling imperfections. Indirect methods, on the other hand, primarily characterize volumetric errors [21]. Ibaraki undertakes a detailed review on the indirect identification of geometric errors [22]. Among others, Ball-bar is an indirect technique vastly used for measuring the machine's volumetric errors [23]. R-test [24], reconfigurable uncalibrated master ball artifact (RUMBA) [25], scale and master bar artifact (SAMBA) [26], and touch and go (TANGO) [27] are other indirect methods developed recently. All these methods analyze the volumetric errors obtained via on-machine measurement through the forward kinematic model of the machine to identify the link imperfections and error motions.

The applications of on-machine measurement can go beyond the identification of geometric errors. The on-machine monitoring of the tool wear phenomenon is another important practice to control the tool's geometric features and maintain its cutting edge during the machining process. Similar to the indication of the machine's error, the methods for tool wear monitoring split into direct and

indirect approaches. Acceptable direct monitoring of the tool's conditions dictates that measuring equipment, such as scanning electron microscopes (SEMs) and atomic force microscopes (AFMs), be independent of the manufacturing line. Particularly, the vacuum chamber of SEMs requires an environment isolated from the machining section. Besides, the time-consuming accurate alignment of an AFM's cantilever probe causes significant inefficiency [28, 29]. On the other hand, the tool's quality is economically detectable via in-process and on-machine indirect methods by measuring process variables such as acoustic emissions [30], cutting force [31], cutting chips [32], and surface finish [33].

A summary of the main advantages of on-machine measurement is as follows.

- In-process measurement: measuring deviations from the desirable part geometry provides feedback to readjust the process parameters. The collected data can be directly used in the machine controller for a real-time self-adapted manufacturing process [34].
- Post-process control: programming and using a machine tool as a CMM provides a complete inspection report of the machine's conditions. This archive includes the history of the process parameters, which can facilitate process optimization and allow for intelligent process control [4].
- Part setup: almost all machining programmes assume certain positioning of the workpiece relative to the machine's table. On-machine measurement considerably reduces the setup time, processing time, and material loss by cutting the parts from optimally positioned blocks [34].
- Monitoring machine tool's performance: the machine's geometry and the tool's conditions change during the machining procedure. Periodic on-machine measurement can capture these variations, prevent unacceptable parts, and schedule the machine maintenance [34].

Some of the most important limitations of on-machine measurement are:

- Cost: the machine tool time is more expensive than the CMM time.
- Lack of accuracy: machine tools are under the influence of various error sources such as thermal issues and geometric errors, which are propagated through the machine's links.

These effects deviate measurement results from true value of the measurand (the quantity intended to be measured).

- Metrology software insufficiencies: the assessment of product quality for real-time decision-making requires in-situ complex mathematical calculations. Various types of metrology software developed for CMMs conveniently perform the GD&T tasks. However, these programmes are inadequate for on-machine applications.
- Environmental variations: unstable conditions of an industrial environment cause unwanted variations in the machine's performance. Not only does this issue affect the accuracy of on-machine measurement, but it also makes the evaluation of measurement uncertainty more complex.

The implementation of on-machine measurement techniques for OMV purposes requires taking two main steps: eliminating the error (bias) associated with the probing outcomes and assigning an uncertainty interval to the measurement results. Dealing successfully with these two steps converts a machine tool to a traceable CMM [13, 35-37]. To detect the measurement bias, high-precision optical methods firstly appeared. Despite their high accuracy, the interferometric methods are susceptible to external disturbances such as vibration and air turbulence in the optic path [21]. For instance, Nomura et al. [38], use a Fizeau interferometer for on-machine measurement of the workpiece's shape and report that it is impossible to exploit the full capacity of the device due to vibrations of the machine tool. Compared with non-contact measurement equipment, contact tools, e.g. touch-trigger probes, have become more commercialized and industrially common. The touch probes are usually spindle-mounted on machining centers and turret-mounted on lathes.

Takaya [21] divides the measurement bias into systematic and random effects. He asserts that the systematic effects mainly stem from the machine's geometric errors, while the random effects are due to the tool's varying position relative to the workpiece. The main challenge of on-machine measurement is that the machine might fail to observe the measurement bias as the same machine carries out both the machining and measurement tasks. Moreover, the thermal effect is known to be a strong environmental and internal factor affecting the machine's accuracy [39-41]. For large-scale production, this issue becomes more evident since a small variation in temperature causes a large thermal deflection in the part, which demands more consideration in the measurement

procedure. It is also possible that the low repeatability of machine tools caused by the poorly controlled environment of the shop floor considerably affects the precision of measurement results.

2.2 Measurement uncertainty

According to the International vocabulary of metrology (VIM), the measurement result is a set of values, together with any other information attributed to the quantity intended to be measured, i.e. the measurand [3]. The measurement result is only an estimate of true value of the measurand [42]. Since the measurement is always an inaccurate procedure due to physical conditions, any measurement procedure requires evaluation. In other words, the value obtained as the measurement result differs from its true value, even if the result is the best possible estimate for the measurand. The measure of this difference is the measurement accuracy [3]. The measurement result in the form of single value has little practical significance unless it comes with a quantified metric of its accuracy. The difference between a measured quantity value and a reference quantity value is the measurement error. VIM [3] divides the measurement error into two components: systematic and random. The systematic measurement error is “the component of the measurement error that in replicate measurement remains constant or varies in a predictable manner”. In the definition of this group of measurement errors, the reference quantity value is “a true quantity value, or a measured quantity value of a measurement standard of negligible measurement uncertainty, or a conventional quantity value” [3]. On the other hand, the random measurement error is the “component of the measurement error that in replicate measurements varies in an unpredictable manner”. The reference quantity value in the identification of random error is “the average that would ensue from an infinite number of replicate measurements of the same measurand” [3]. The two types of measurement error can appear as quantified terms in the mathematical model of the measurement task. This model converts the input quantities to a best estimate of the measurand. This model might include correction: the value algebraically added (Figure 2-3) or multiplied to the input quantities to compensate for the systematic error. However, the correction cannot completely eliminate the systematic error, but can reduce it [42].

The uncertainty of measurement is defined as a parameter reflecting the dispersion of the values reasonably attributed to the measurand [3, 42]. This parameter implies the lack of knowledge about true value of the measurand. After the correction for determining systematic effect, the

measurement result remains only an estimate because of two main uncertainty sources: random variations of the input quantities and imperfect corrections for the systematic effect [42]. The uncertainty associated with the systematic error correction is not itself a systematic error. This incomplete knowledge of the required correction value contributes to measurement uncertainty. The compensated measurement result can lie accidentally very close to true value of the measurand, although it might come with a large value of uncertainty. Thus, measurement uncertainty is different from the remaining unknown error (Figure 2-3) [42].

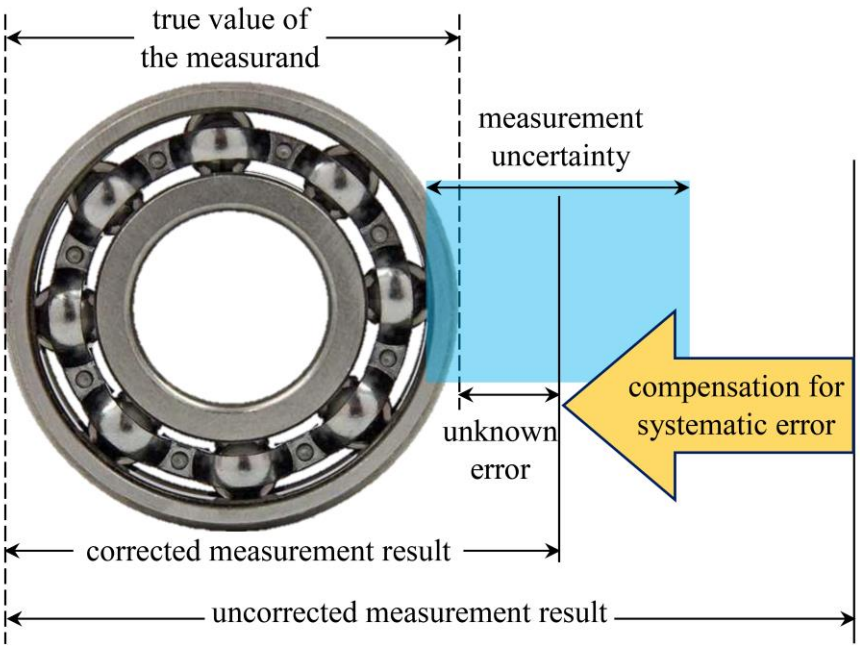

Figure 2-3: Schematic illustration of the compensation for systematic error.

In general, various sources contribute to measurement uncertainty. An incomplete definition or an imperfect realization of the measurand is an uncertainty source, termed “definitive” and “intrinsic” uncertainty by VIM [3] and GUM [3], respectively. For example, defining the measurand as the thickness of a sheet or the flatness of a surface triggers intrinsic uncertainty resulting respectively from an infinite number of true values of the measurand (thickness) and insufficient data about the measurand (flatness). Non-representative sampling, limited knowledge of environmental conditions, finite instrument resolution, and non-identical measurement replications are among

other uncertainty sources. Depending on the measurement task, different uncertainty factors might come into effect, which might originate from dependent (correlated) sources [42].

ISO 14253-1 [43] clarifies the role of uncertainty assessment in decision-making and conformity check of a fabricated part. Although technical drawings specify certain geometric tolerances, measurement uncertainty narrows the tolerance zone. This standard [43] elaborates on this issue by defining two zones, namely conformance, and non-conformance zone (Figure 2-4). Part conformity requires that the measurement result lie within the conformance zone. In one-dimensional metrology, the conformance zone and the uncertainty interval sum up to the tolerance zone. That is, the larger the uncertainty interval, the narrower the conformance zone. The uncertainty interval defines the area where the compliance is indeterminable. This implies that specifying as small an uncertainty interval as possible to the measurement result increases the conformity chance of the manufactured part [43].

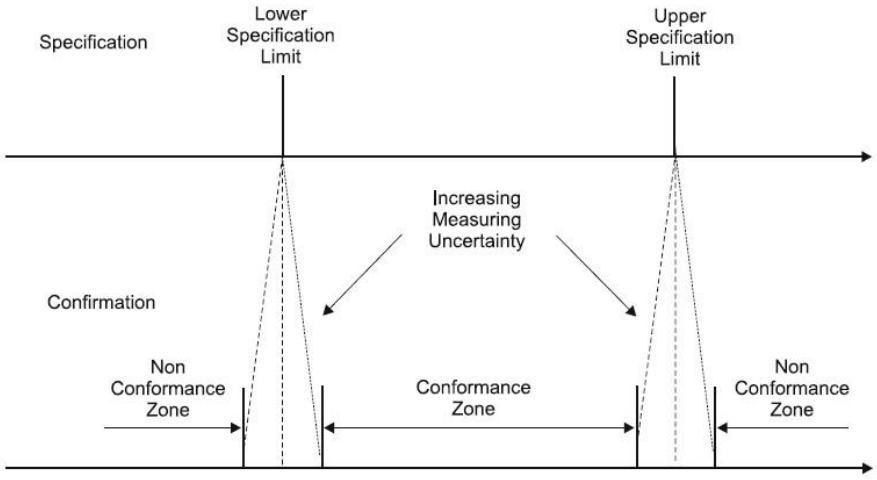

Figure 2-4: Dependence of the tolerance zone on measurement uncertainty [43].

In the case of coordinate measurements, where a spatial vector describes the measurement accuracy, specifying an uncertainty interval to each coordinate gives an ellipsoidal uncertainty zone, characterized by the three diameters representing the three orthogonal uncertainty intervals.

Since most of the measuring systems suffer from systematic errors, the evaluation of the uncertainty associated with an imperfect correction of the measurement result is crucial. That is,

the uncertainty associated with the measurement results obtained by a certain measurement system depends on its calibration procedure. ISO 15530 [1, 2] includes the uncertainty evaluation methods for coordinate measurement with CMMs. ISO 15530-3 [1] specifies the details of an uncertainty evaluation procedure, known as the "substitution method", using a calibrated workpiece nominally similar to the part under measurement. According to this standard, the measurement task must hold certain similarities to the calibration process, in terms of part's dimension and geometry, sampling strategy, and environmental conditions. ISO 15530-3 includes many effects such as repeatability and geometric errors, temperature and drift, random and systematic errors of probing device, measurement strategy, and scale resolution, as uncertainty effects arising from CMM and the measurement procedure [1]. Nevertheless, this standard assumes that these numerous effects appear through four main uncertainty terms: measurement procedure, calibration of counterpart, calibration of measurement process, and the differences between the measured part and the calibrated counterpart (in roughness, form, coefficient of thermal expansion, and elasticity) [1]. These factors together with environmental considerations are the sources that contribute to the uncertainty associated with the measurement result.

The "substitution method" is the approach used most for uncertainty evaluation in on-machine measurement [36, 44-47]. The first disadvantage of this application is its dependence on a calibrated counterpart. Manufacture and calibration of a reference workpiece for any new part is costly, especially for large part machining. Moreover, the methodology specified in ISO 15530-3 [1] gives the uncertainty associated with "task-specific" measurements, which only suits the intended measurement procedure. Therefore, this method can be efficient only if the sampling task and other factors influencing measurement uncertainty remain unchanged throughout the measurements done for quality control purposes. However, the uncontrolled work environment of machine tools causes variations in both the machine's and part's status. The exclusion of any correlation analyses between the uncertainty budgets is another important limitation of this method.

2.3 Evaluation of measurement uncertainty

GUM [42] is the internationally accepted master document for uncertainty evaluation in the measurement of physical objects. Instead of classifying the uncertainty components, this guide categorizes the methods of evaluating them. Accordingly, the evaluation methods of uncertainty

split into type A and type B. The type A evaluation (of uncertainty) includes "the statistical analysis of series of observations" [42]. In most cases, the best available estimate for the expectation or expected value μ_w of random variable W is the average or arithmetic mean $\overline{w}$ of n independent observations obtained under the same measurement conditions. Individual observation w_i differ from others because of random effects. GUM defines the experimental standard deviation of the observations as standard uncertainty $u(w)$ of best estimate μ_w:

$$u(w) = \sqrt{\frac{1}{(n-1)}\sum_{i=1}^{n}(w_i - \overline{w})^2} \qquad 2\text{-}1$$

The type B evaluation of uncertainty is "by means other than the statistical analyses of series of observations" [42]. In this type, a scientific assessment based on all available knowledge of the variability of the parameter evaluates standard uncertainty. Usually, quantifying an uncertainty component using an external source is a type B evaluation of uncertainty. For instance, in ISO 15530-3 [1], the uncertainty associated with the calibrated value is a type B evaluation, whereas the uncertainty associated with the measurement bias and the repeatability of the recorded data is of type A.

Usually, instead of determining measurand Y directly from the outcomes of the measuring instrument, measurement function f estimates the measurement results. This function has N input quantities $X_1, \dots, X_N$:

$$Y = f(\boldsymbol{X}) = f(X_1, \dots, X_N) \qquad 2\text{-}2$$

The vector of input quantities $\boldsymbol{X}$ includes values whose uncertainty comes from either the current measurement or external sources.

The evaluation of measurement uncertainty relies on the propagation of uncertainty of the input quantities through the measurement function. This means, the distribution of the output quantity, which encodes the standard uncertainty associated with the output estimate, is obtainable by propagating the distributions of input quantities through the measurement function. In Figure 2-5b, the propagation of joint probability density function (PDF) $g_{\boldsymbol{X}}(\boldsymbol{\xi})$ through measurement function f gives PDF $g_Y(\eta)$ for measurand Y. In this figure, $\boldsymbol{\xi}$ and η denote possible values for the input vector and output scalar quantity, respectively. Joint PDF $g_{\boldsymbol{X}}(\boldsymbol{\xi})$ includes the information about the

statistical behaviour of input vector $\boldsymbol{X}$ together with the correlations between each pair of random variables X_i and X_j. In a metrological context, the distribution of input quantities carries the required information on uncertainty sources such as measured values, calibrated values, and expert knowledge about other uncertainty budgets. Then, input joint PDF $g_{\boldsymbol{X}}(\boldsymbol{\xi})$ includes even those input quantities that possess Type-B standard uncertainty. If all or several input quantities have strong correlations, $g_{\boldsymbol{X}}(\boldsymbol{\xi})$ is not decomposable. On the other hand, if all input variables are mutually independent, the joint PDF of $\boldsymbol{X}$ can be replaced by the product of PDFs $g_{Xi}(\xi_i)$ for the individual input variable X_i [42]. PDF $g_Y(\eta)$ stores statistical information of the measurand, from which measurement uncertainty is obtainable.

One can adopt three main approaches of propagation of distributions to evaluate measurement uncertainty:

1) First, so-called the "Markov formula" analytically gives the PDF of the output quantity as below [48]:

$$g_Y(\eta) = \int_{-\infty}^{\infty} \dots \int_{-\infty}^{\infty} g_{\boldsymbol{X}}(\boldsymbol{\xi})\, \delta\big(\eta - f(\boldsymbol{\xi})\big) d\xi_1 \dots d\xi_N \qquad 2\text{-}3$$

where δ represents the Dirac delta function. Analyzing PDF $g_Y(\eta)$ for the output variable can then specify a suitable coverage interval that contains true value of the measurand with desirable coverage probability p. GUM refers to this interval as expanded uncertainty U. The expanded uncertainty can be expressed as $U = \eta_{\max} - \eta_{\min}$, where $\eta_{\max}$ and $\eta_{\min}$ are possible values of Y, which satisfy

$$G_Y(\eta_{\max}) - G_Y(\eta_{\min}) = p \qquad 2\text{-}4$$

and are obtainable from $G_Y(\eta)$, cumulative distribution function (CDF) of Y. In other words, $\eta_{\max}$ and $\eta_{\min}$ create a 100 p% coverage interval for Y. Such an interval is not unique and, considering the necessity of choosing the smallest possible uncertainty interval, expanded uncertainty U is the shortest possible 100 p% coverage interval. If Y is distributed to certain distributions such as normal, the expanded uncertainty for output quantity Y is derivable without determining $\eta_{\max}$ and $\eta_{\min}$. In Figure 2-5a, the half-width of the light grey area is the standard uncertainty $u(y)$, associated with best estimate y for measurand Y, which is a measure of the dispersion of the values

attributable to Y. The half-width of the light grey zone and the adjacent dark grey area denote expanded uncertainty U, which can be expressed as $U = k_p u(y)$ for certain distributions, where k_p is the coverage factor. For a normal distribution, coverage factors 2 and 3 give 95% and 99% coverage probability, respectively.

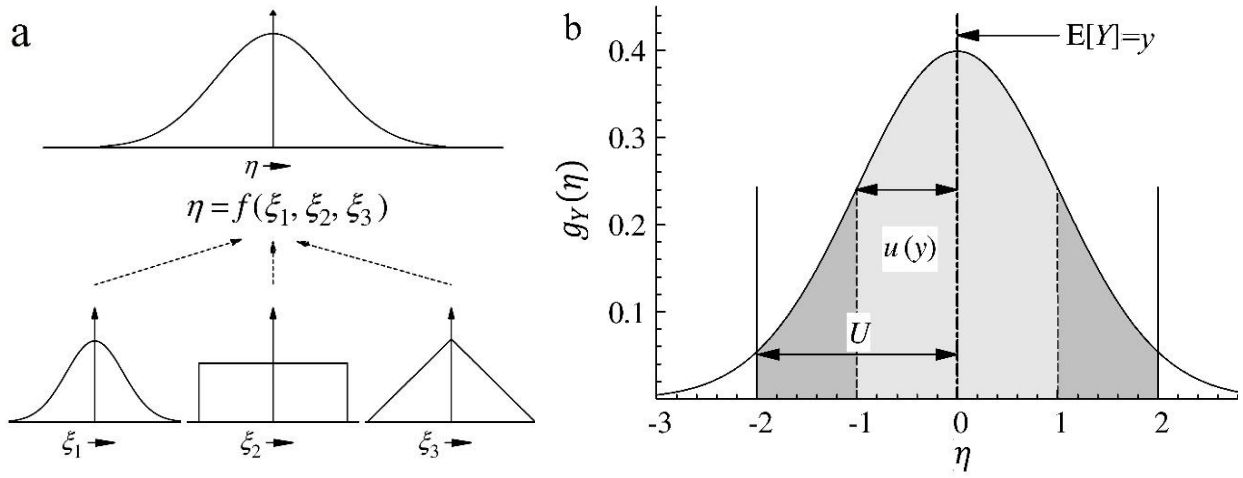

Figure 2-5: a) Propagation of possible values ξ_i of X_i through measurement function f and the creation of the output's distribution describing the possible values η of Y, and b) the normal PDF for output quantity Y. Best estimate y of measurand Y is assumed to be the expected value of Y. The standard deviation is the standard uncertainty $u(y)$ associated with y. The expanded uncertainty U includes 95% of possible values of y, corresponding to a coverage factor of 2 [49].

Although the analytical method based on Eq. 2-3 provides a PDF for the output quantity, it remains a feasible solution merely for simple measurement models with untangled PDFs for their input quantities. In on-machine measurement, where the compensation for systematic effects occurs through a chain of homogeneous transformation matrices (HTMs), adopting this analytical approach can be demanding. Moreover, the possible high correlations between the inputs of the on-machine measurement function can raise further complexity for this method. Besides, the covariance matrix and, in turn, the joint PDF of the input quantities vary from point to point on the machine tool, which requires separate solutions of Eq. 2-3 to calculate the uncertainty associated with a set of points. These disadvantages besides being single-output make this approach unsuitable for uncertainty estimation in on-machine measurement.

2) The second approach is the "law of propagation of uncertainty" specified by GUM. According to VIM, the uncertainty associated with best estimate y of measurand Y, termed "combined standard uncertainty" $u_c(y)$, is obtainable based on the individual standard uncertainty associated with each input quantity. In this method, approximating y about its expected value with a Taylor series leads to the combined standard uncertainty of y:

$$u_c(y) = \sqrt{\sum_{i=1}^{N} \left(\frac{\partial f}{\partial x_i}\right)^2 u^2(x_i) + 2\sum_{i=1}^{N-1}\sum_{j=i+1}^{N} \frac{\partial f}{\partial x_i}\frac{\partial f}{\partial x_j} u(x_i, x_j)} \qquad 2\text{-}5$$

where $u^2(x_i)$ is the square of standard uncertainty associated with best estimate x_i of input quantity X_i and $u(x_i, x_j)$ is the covariance between x_i and x_j. If input quantities $X_1, \dots, X_N$ are mutually independent, the second term under the radical in Eq. 2-5 equals zero. Each $u(x_i)$ is a standard uncertainty obtained with a Type A or Type B evaluation. The combined standard uncertainty $u_c(y)$ is an estimate for standard deviation of the output quantity and determines the dispersion of values attributable to measurand Y. Eq. 2-5 is the law of propagation of uncertainty, referred to as the "delta method" in statistics. Unlike Eq. 2-3, this method does not provide any PDF for the output quantity. Then, the expanded uncertainty corresponding to a stipulated coverage probability is not obtainable by Eq. 2-4. If the PDF of Y is normal, the expanded uncertainty can be specified by $U = k_p u_c(y)$, providing 95% and 99% coverage probability for coverage factors 2 and 3, respectively.

The law of propagation of uncertainty specified by GUM is limited to multi-input single-output measurement models. Supplement 2 to GUM [50] extends this method for multivariate problems, known as the "GUM uncertainty framework" (GUF). Supposing implicit multivariate measurement model $h(\boldsymbol{Y}, \boldsymbol{X}) = \boldsymbol{0}$, where $\boldsymbol{X} = (X_1, \dots, X_N)$ and $\boldsymbol{Y} = (Y_1, \dots, Y_m)$ are respectively the input and output quantity vectors, the relation between the covariance matrix of input quantities $\boldsymbol{U_x}$ and that of output variables $\boldsymbol{U_y}$ is [50]

$$\boldsymbol{U_y} = \boldsymbol{C}\boldsymbol{U_x}\boldsymbol{C}^{\mathrm{T}}, \qquad \boldsymbol{C} = \boldsymbol{C_y}^{-1}\boldsymbol{C_x} \qquad 2\text{-}6$$

in which, $\boldsymbol{C_x}$ and $\boldsymbol{C_y}$ are the sensitivity matrices of dimension $m \times N$ and $m \times m$, which include the partial derivatives of the measurement model with respect to the input and output quantities, respectively.

3) The third approach to address the propagation of distributions is the Monte Carlo method (MCM). This method uses pseudo-random numbers to draw at random from the joint PDF of input quantities. Evaluating a drawn set of input quantities through measurement model f creates the corresponding values of the measurand. Repeating this process for M times results in the same number of vectors of the output quantities. A telling example of an application of this method is in the approximation of the value of π. Supposing a quarter circle inscribed in a unit square (Figure 2-6a), the probability that a random point chosen within the unit square lies within the quarter circle is equals the ratio between their areas, $A_{\text{quarter-circle}}/A_{\text{square}} = \pi/4$. Using MCM, this probability (and, in turn, an approximation of the value of π) is obtainable by drawing at random the coordinates of a large number of points from the uniform distribution U(0,1) (Figure 2-6b).

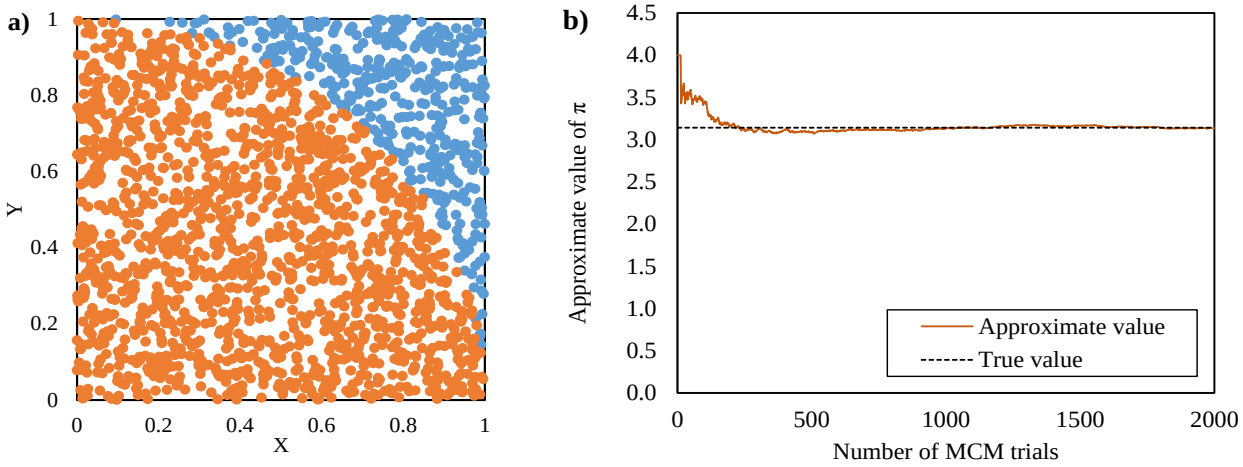

Figure 2-6: a) The application of MCM for the approximation of the value of π; a) 2000 points chosen at random within a unit square illustrated in different colours, denoting whether they lie in the quarter circle or not, and b) estimate of π converging to its true value by increasing the number of MCM trials.

The competitive advantage of MCM is its reasonable convergence properties. According to the central limit theorem, the average $\boldsymbol{y}$ of the M values attributed to measurand $\boldsymbol{Y}$ converges to the expectation of $\boldsymbol{Y}$ proportional to $M^{-0.5}$ [51]. That is, to improve the numerical accuracy of $\boldsymbol{y}$ by one binary digit, it suffices to increase M fourfold [52]. As a result, the convergence properties of MCM is independent of the number of input quantities N.

A multivariate sample generator serves as the engine of an MCM simulator. In univariate cases, a common approach to create a sample of a random variable is to use its inverse CDF. To this end, the sample generator draws a random number between 0 and 1 from uniform distribution U(0,1), then converts it to a random sample using the inverse CDF. However, drawing a multivariate random sample from a joint PDF might be delicate. Supplement 1 to GUM proposes the following equation to draw M random vectors from an N-dimensional multivariate normal distribution:

$$\boldsymbol{G_X} = \boldsymbol{\mu}\mathbf{1}_{M\times 1}{}^{\mathrm{T}} + \boldsymbol{R}^{\mathrm{T}}\boldsymbol{Z} \qquad 2\text{-}7$$

where $\boldsymbol{G_X}$ is an $N \times M$ matrix whose the j^{th} column is a random draw from the multivariate normal distribution, $\boldsymbol{\mu}$ is the vector of expectations (means) of dimension $N \times 1$, and $\mathbf{1}_{M\times 1}$ is a vector of ones of dimension $M \times 1$. In this equation, matrix $\boldsymbol{Z}$ of dimension $N \times M$ includes M draws from the N-dimensional standard normal distribution, and $\boldsymbol{R}$ is the Cholesky factor (a lower triangular matrix) of covariance matrix $\boldsymbol{U_x}$ of dimension $N \times N$, which satisfies the following equation

$$\boldsymbol{U_x} = \boldsymbol{R}\boldsymbol{R}^{T} \qquad 2\text{-}8$$

To evaluate the uncertainty of m measurands with respect to N input parameters, matrix $\boldsymbol{G_Y}$ of dimension $m \times M$ stores the set generated for output quantities. Matrices $\boldsymbol{G_X}$ and $\boldsymbol{G_Y}$ are discrete representations of input and output parameters [50] The i^{th} row of $\boldsymbol{G_X}$ and the j^{th} row of $\boldsymbol{G_Y}$ are the discrete representations of marginal distributions for scalar quantities X_i and Y_j, respectively [52]. $\boldsymbol{G_Y}$ encodes statistical information about the output values. Taking the average of each row of $\boldsymbol{G_Y}$ provides $\boldsymbol{y}$, a best estimate for $\boldsymbol{Y}$, as follows.

$$\boldsymbol{y} = \frac{1}{\boldsymbol{M}}\mathbf{G_Y}\mathbf{1}_{M\times 1} \qquad 2\text{-}9$$

The covariance matrix associated with best estimate $\boldsymbol{y}$ is

$$\boldsymbol{U_y} = \frac{1}{M-1}\mathbf{G'_Y}(\mathbf{G'_Y})^{\mathrm{T}}, \qquad \mathbf{G'_Y} = \mathbf{G_Y} - \boldsymbol{y}(\mathbf{1}_{M\times 1})^{\mathrm{T}} \qquad 2\text{-}10$$

The i^{th} diagonal element of $\boldsymbol{U_y}$ is the square of standard uncertainty associated with the i^{th} output quantity. The off-diagonal value on the i^{th} row and the j^{th} column of this matrix represents the covariance between the corresponding output values.

The $100p\%$ coverage interval bounded by $\eta_{\min}$ and $\eta_{\max}$ of the single output scalar Y_i is easily achievable using MCM. To this end, after sorting the values on the i^{th} row of $\boldsymbol{G_Y}$ in non-decreasing order, the values whose indices differ by pM are $\eta_{\min}$ and $\eta_{\max}$ [52]. In a multivariate case, the determination of coverage interval is more complicated as it requires sorting multivariate data. In this regard, Supplement 2 to GUM [50] indicates three main forms of coverage regions: hyper-ellipsoidal, hyper-rectangular, and the smallest coverage region.

Considering the convergence of the MCM results, Supplement 2 to GUM [50] specifies the details of an "adaptive MCM" procedure by incorporating convergence criteria into the MCM algorithm. The effectiveness of MCM in estimating the statistical metrics of output quantities depends on the number of conducted trials. The convergence criteria set the desirable stability and precision of the MCM numerical results. Supplement 2 to GUM [50] suggests that after h sequences of MCM (each sequence includes M trials), convergence holds if the standard deviations associated with h accumulative estimates for $\boldsymbol{y}$, standard uncertainties $\boldsymbol{u}(\boldsymbol{y})$, the maximum eigenvalue $\lambda_{\max}$ of the associated correlation matrix, and coverage factor k_p, are smaller than stipulated numerical tolerances. Otherwise, the MCM simulator runs one more sequence and continues until the convergence occurs.

MCM has a wide range of application in various areas of science and industry. Particularly, this method has been adopted for the evaluation of measurement uncertainty in CMMs. Balsamo et al. [53] introduce "expert CMM" (ECMM) aiming at the uncertainty evaluation of the CMM results. Adhering to GUM, they conduct task-oriented measurement strategies with minimum involvement of the user. For both on-line (immediate check) and off-line (comparative evaluation) measurement, they also examine the possibility of decomposition of error contributors. They estimate the CMM parameters (only geometric errors) by a self-calibration procedure introduced in [54]. Their measurement procedure includes probing a calibrated artifact at 100 different positions in the working volume of the CMM. For 93 measurements, true value of the measurand lies within the estimated 95% expanded uncertainty. Schwenke et al. [55] use an MCM uncertainty

evaluator in complex dimensional measurements. They develop a software package including a library of uncertainty contribution modules. To verify them, they conduct complex tasks on a CMM including the surface roughness measurements with a stylus, roundness measurement with form testers, and geometric feature measurements. Their experiments result in 96% and 97% coverage probability for an estimated 95% expanded uncertainty interval.

In another application of MCM, Sladek and Gaska [56] develop a virtual CMM simulator to evaluate the measurement uncertainty of probed coordinates. This scheme focuses on the volumetric error caused by the CMM joint errors and the probe's deviations assuming that the system has an effective thermal compensator consisting of at least two temperature sensors and that it works under controlled environmental conditions specified by the manufacturer for best performance. They use a laser tracer to indicate the kinematic errors of the CMM equipped with a retro-reflector. Then, they estimate the volumetric errors caused by the identified joint errors at asset of target points uniformly distributed within a grid. They also quantify the contribution of the probe to volumetric error by probing a precision sphere under different probing strategies. To verify their model, they use a cylindrical standard and a double bar artifact and measure them at different positions and with varying probing strategies. They validate their model by reporting considerable overlaps between the expanded uncertainty intervals of the probed features and those of the calibrated values.

The MCM uncertainty estimators are also practical for measuring form features. Wen et al. [57] apply this technique to investigate the uncertainty associated with cylindricity. Employing a quasi-partial swarm optimization algorithm, they solve a mathematical equation for the minimum cylindricity zone, which serves as measurement function. Then, they evaluate the uncertainty of cylindricity through MCM and GUF. Along with the parameters that appear in the cylindricity equation, they also consider the effects of the measurement repeatability, thermal variations, thermal expansion coefficient, drift and hysteresis, and sampling strategy. Comparing with the adaptive MCM results, they find GUF invalid to quantify the uncertainty of cylindricity errors. In another investigation on the uncertainty of form features, Kruth et al. [58] particularly study roundness, though their approach can cover various types of form features. They incorporate an error simulator in a CMM software, which provides their MCM with feature imperfections including position, orientation, size, and form features. Suitably bounding these features, they

compare the uncertainty associated with form deviations of circular profiles with and without the form effects. They show that the uncertainty of form deviations considerably affects measurement uncertainty so that by excluding this effect, true values of the measurand (diameter and center distance of circular profiles) lie off the expanded uncertainty interval. Ren et al. [59] use MCM to quantitatively analyze the measurement uncertainty associated with the profile of freeform surfaces. They first develop a measurement model by establishing a mathematical relation for the target features of freeform surfaces. Then, they introduce a generator of random form errors into an MCM simulator. They also develop an analytical model for measurement uncertainty, which allows for the uncertainty estimation in the freeform measurement tasks. Using an ultra-precision freeform mould insert of a bifocal optical lens, they verify the model by studying the uncertainty associated with the pick-to-valley height of the freeform surface.

Many researchers apply MCM to address the machine tool's accuracy and volumetric error. Bringmann and Knapp [60] estimate the uncertainty associated with the calibration technique "chase-the-ball" using MCM. In their algorithm, a virtual machine tool receives a set of volumetric errors randomly drawn from uniform distributions. They define the error PDFs based on various specifications and standards. Then, they calculate the machine parameters based on the simulated calibration procedure. Comparing the calculated and predefined error values, they estimate the uncertainty associated with the machine parameters. They adopt the same approach to estimate the uncertainty of the parameters obtained by another calibration procedure called "3-D ball plate" [61]. Andolfatto et al. [62] use the non-contact measuring instrument "CapBall" to identify the machine's link errors and then implement MCM to estimate the associated uncertainty. Considering the uncertainties of the CapBall's sensors, transformation matrices, and the drift of the closed kinematic chain, they estimate the uncertainty of 8 link errors and 6 setup errors. They compare two different methods to model the thermal drift of the machine: statistical and cyclic. They conclude that the statistical method results in smaller confidence intervals, while the cyclic method is more reliable because it better quantifies the cyclic behaviour of the dimensional alternations caused by thermal changes. They argue that including the effect of drift in uncertainty evaluations results in less normality in the output distribution because the MCM trials do not hold the identical conditions required for replicated experiments. Los and Mayer [63] implement an adaptive MCM to evaluate the uncertainty associated with 8 link errors and 3 error motions

denoting the slope of the positioning errors of the three prismatic axes of a five-axis machine tool. They identify the machine's geometric errors via the SAMBA method. The inputs of their measurement model are the coordinates probed on SAMBA. While the machine is cold or is cooling down from 27 to 23 °C, repeating the SAMBA test over 24 h gives the probability distribution of the input quantities. The obtained joint PDF covers the covariance between the input quantities caused by interdependencies of error sources. They report smaller rectangular coverage intervals without the warm-up cycle, although this poorly represents the real performance conditions of the machine.

When it comes to the uncertainty evaluation of on-machine tool probing, the literature is lacking an inclusive approach that includes a full covariance analysis between the input quantities. The very few related studies concern the dominant uncertainty sources in on-machine measurement and eliminating the need for a calibrated reference as specified by ISO 15530-3. Using a task-specific method for uncertainty evaluation, Mutilba et al. [45] quantify the major uncertainty budgets in on-machine probing. They fabricate a workpiece possessing certain geometric features and then calibrate each feature with a CMM. Carrying out on-machine probing on the machined part, they study the contribution of each uncertainty factor suggested by ISO 15530-3. They report the repeatability of on-machine measurement to be the most dominant uncertainty source. They find this term even more influential for the on-machine probing following the machining process. They detect a strong correlation between the machine's geometric errors and volumetric error. In another study [44], they examine the feasibility of excluding the calibrated reference required by ISO 15530-3. For each target point, they indicate volumetric error and the associated uncertainty using a laser tracer before starting on-machine measurement. This enables them to approximate the volumetric error at any position on the machine tool. Accordingly, they calculate the measurement bias of a calculated feature and validate their results by showing the possibility of excluding the calibrated workpiece.

CHAPTER 3 : METHODOLOGY AND SYNTHESIS

3.1 Methodology

The methodology of this study includes the following steps. Figure 3-1 also shows the data flow of this project.

3.1.1 Uncertainty estimation schemes

The measurement uncertainty schemes consist of an adaptive MCM and a GUF estimator. Supplements 1 and 2 to GUM are the bases of the uncertainty schemes. Each input quantity is regarded as a random variable. In the adaptive MCM, a joint PDF encodes the required statistical information including best estimates and correlations of the input quantities. The MCM estimator generates a set of input vectors by drawing at random from the input joint PDF. Each MCM trial includes the evaluation of one input vector stored in the input set with a measurement function. When estimating the uncertainty of the machine's geometric errors, this function is the SAMBA algorithm, an iterative solution to tune the machine's forward kinematic model so that the predicted volumetric errors fit those collected with the on-machine probing of SAMBA. When estimating the uncertainty associated with on-machine probed positions, the measurement function is the machine's forward kinematic model. The statistical analysis of the MCM output set provides an assessment of the uncertainty associated with the measurand.

The second scheme analytically evaluates measurement uncertainty through GUF, which considers a Taylor series approximation of the measurement function. Supplement 2 to GUM specifies this method based on the law of propagation of uncertainty for multi-input multi-output measurement functions. This method is supposedly less precise and more efficient compared to MCM. Then, the MCM estimator validates the GUF scheme. This requires knowing the sensitivity coefficients of the measurement function with respect to the input quantities. To this end, we use numerical differentiation.

Considering the machine's forward kinematic model as the measurement function of on-machine probing of a single point, the input quantities are the five joint positions recorded at the moment the probe's tip touches the target surface, plus the thirteen machine's geometric errors used to

compensate for the measurement bias with a 13-error model. A suitable joint PDF embodies the statistical behaviour of these input parameters.

3.1.2 On-machine probing repeatability

Part of the uncertainty associated with the on-machine probed joint positions includes the repeatability of the probing results. Accordingly, carrying out replicated on-machine probing tasks, a mathematical model is fitted to the covariance values of the recorded joint positions collected by varying the effective factors expected to influence the repeatability of on-machine probing results. These factors are the five positions of the machine's axes and two spherical coordinates defining the unit vector of the approach direction. This repeatability model estimates the on-machine probing repeatability in the form of 5×5 covariance matrices (the blue matrices in Figure 3-1) with respect to these effective factors. Since the rotary axis positions remain immobile when the probe approaches the target, the positions reported for these axes are constant and equal to the commanded values. As a result, the corresponding elements of the covariance matrix equal zero.

3.1.3 Machine geometric errors and associated uncertainty

Besides the probed joint positions, the machine's geometric errors are the other inputs of the on-machine measurement function, i.e. the machine's forward kinematic model. The SAMBA technique identifies these parameters. The iterative solver of this method receives 328 input quantities, including 327 coordinates of ball centre indications (including three Cartesian coordinates for each of 109 ball measurements done during one SAMBA test) plus the length of the SAMBA's calibrated scale bar. This function returns 13 machine parameters including eight inter axis imperfections and three error motions of the prismatic axes. A separate adaptive MCM and the corresponding GUF scheme estimate the uncertainty associated with the machine parameters. Replicated SAMBA tests provide a quantitative picture of the variations of the machine's status through the covariance matrix of the 328 input parameters. The adaptive MCM estimates the 13 machine parameters along with their associated uncertainty in the form of a 13×13 covariance matrix (the orange matrix in Figure 3-1). The MCM estimator then examines the feasibility of the GUF application in the identification of machine's errors with SAMBA. Unlike the repeatability tests that concern the short-term variations of the reported joint positions, the

replicated SAMBA tests reflect the long-term random behaviour of the machine. This enables the uncertainty schemes to take into account the day-to-day variations of the machine tool and include this effect in the estimated uncertainty for on-machine measurement.

3.1.4 Covariance of input quantities

Since the quantifications of the two input sets of the on-machine measurement function, discussed in 3.1.2 and 3.1.3, occur separately, a complementary treatment is required to assemble them in the form of a joint PDF defined by a full covariance matrix. To this end, for a point set (point cloud) of size n, a covariance simulator receives n repeatability covariance matrices (each of dimension 5×5) and the covariance matrix of the machine parameters (of dimension 13×13) and simulates a $5n$+13×$5n$+13 covariance matrix for the input quantities of the on-machine measurement function.

3.1.5 Uncertainty assessment in on-machine probing and GD&T

The covariance matrix and best estimates of the input quantities initiate the adaptive MCM estimator. The concerned outputs of the machine's kinematic function are three compensated Cartesian coordinates of the probe's tip in the workpiece frame for each probed point. The MCM scheme estimates $3n$ compensated coordinates and the associated joint PDF, specified by a $3n$×$3n$ covariance matrix (the green matrix in Figure 3-1). Including a geometric-feature function as an add-on in the MCM estimator also enables the scheme to assess the GD&T results. The output of this function is a scaler value of a geometric feature such as length, flatness, sphericity, etc. The experimental validation of estimated uncertainty includes the on-machine probing of calibrated references, such as a gauge block and a precision sphere, at several positions of the machine's work envelope. The portion of the experimental results whose estimated expanded uncertainties encompass the calibrated value should be as large as the desired coverage probability (for a speculated coverage factor).

3.2 Dissertation synthesis

After defining the scope of this study in the first two chapters, the four following chapters present the steps towards the objectives defined in 1.2. Chapter 4 includes the repeatability analysis of on-machine measurement. This chapter covers the repeatability models in on-machine probing and the

influence of other factors such as hysteresis and resolution. Chapter 5 concerns the machine parameters and the associated uncertainty (covariance matrix). An adaptive MCM is the main approach to this goal and then, its results validate the GUF application as an efficient alternative. Chapter 6 addresses the uncertainty assessment in on-machine measurement via an adaptive MCM estimator. This chapter specifies the details on the covariance matrix simulator and the experimental validation of estimated expanded uncertainty. Chapter 7 discusses the validation of GUF for the on-machine probing results. Figure 3-2 presents the synthesis of the four following chapters. Figure 3-1 also categorizes the subjects covered by articles (chapter).

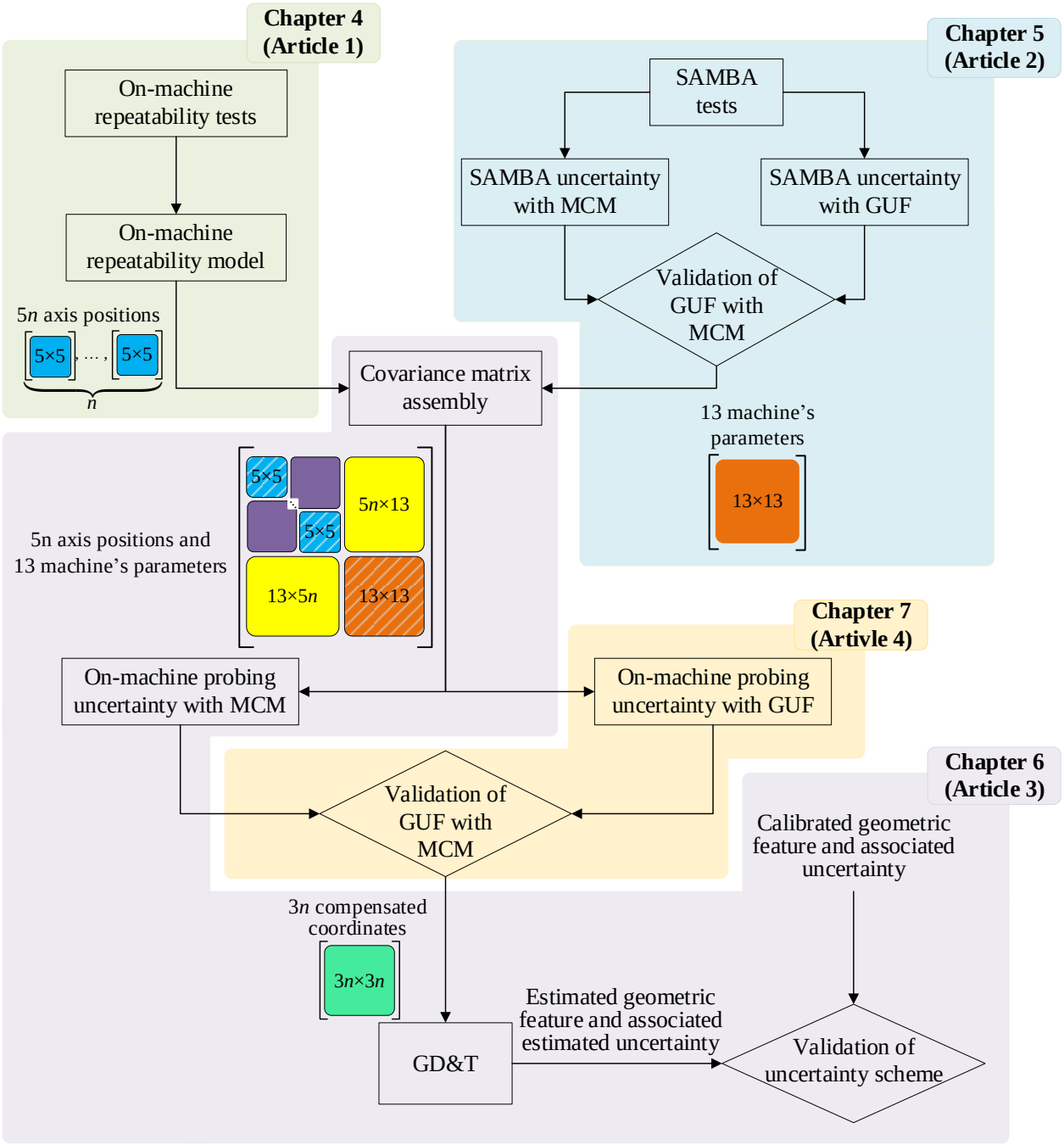

Figure 3-1: Data flow in the uncertainty assessment in on-machine measurement. Also shown are best estimates and the covariance matrices obtained at certain steps when processing a point set of size n.

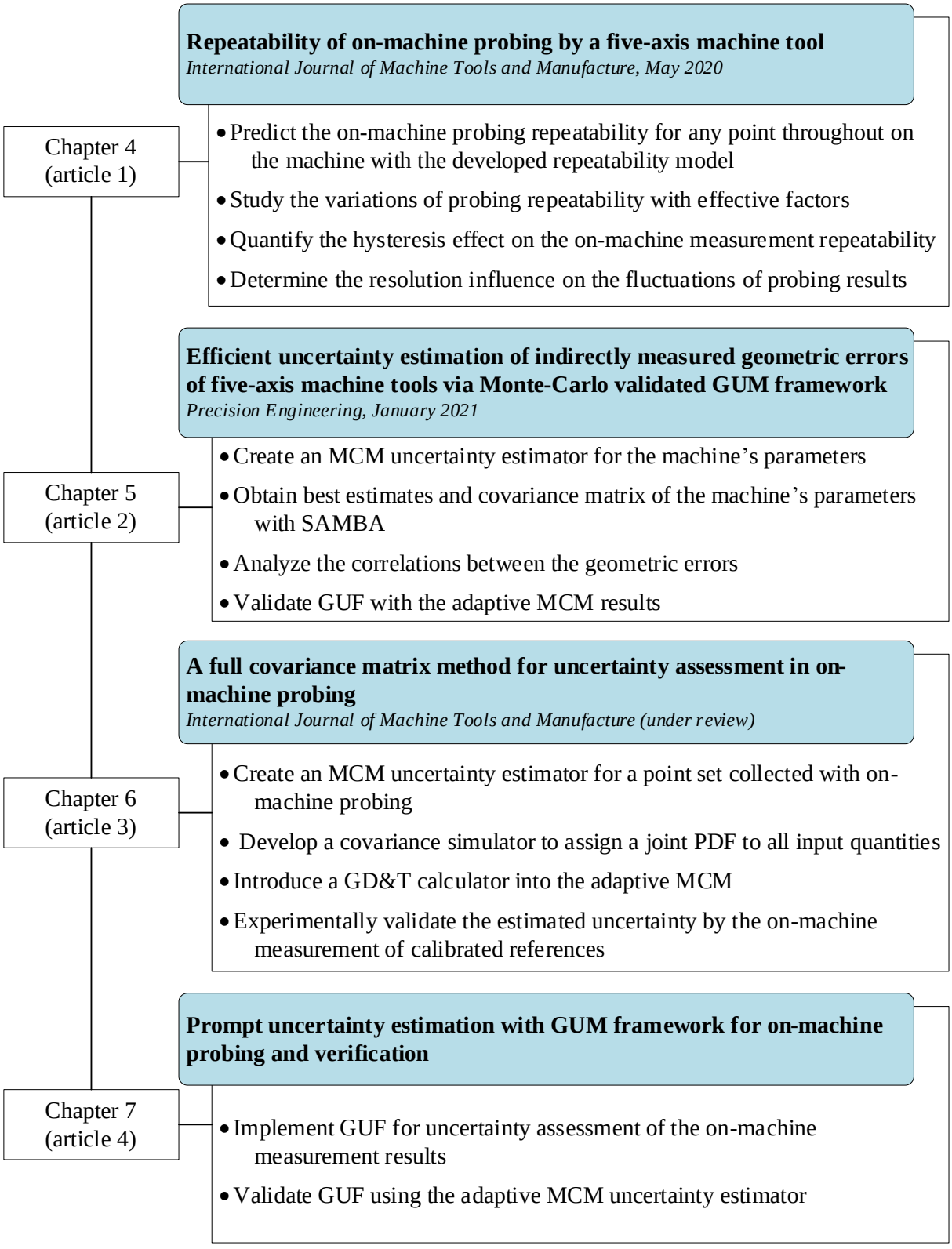

Figure 3-2: Synthesis of Chapters four to seven and the subjects covered by each chapter.

CHAPTER 4 : ARTICLE 1: REPEATABILITY OF ON-MACHINE PROBING BY A FIVE-AXIS MACHINE TOOL

Published in: International Journal of Machine Tools and Manufacture, March 2020

Authors: Saeid Sepahi-Boroujeni[*a]; J.R.R. Mayer[a]; Farbod Khameneifar[a]

4.1 Abstract

Assessing the repeatability of on-machine probing is required to estimate the measurement uncertainty. Currently, standards such as ISO 230-2:2014 and ISO 230-6:2002 include approaches only for a single-axis or a diagonal-path evaluation of the machine repeatability. Also, ISO 230-10:2016 is limited to the evaluation of the probing repeatability at a specific position of the machine for single-point surface measurement as well as for measuring the circle and sphere centre location. In this paper, a general model capable of predicting the measurement repeatability, considered as a covariance matrix, for a five-axis machine in any probing situation is sought from replicate measurements on a spherical artifact at various positions and with different probing directions. Polynomial functions fitted to the X, Y and Z recorded coordinates as well as to the normal (radial) and tangential projection values respectively perpendicular and tangent to the target surface estimate the standard deviations, i.e. the square roots of the diagonal elements of the covariance matrix, of on-machine probing in terms of experimental factors. Separate polynomials were fitted to the covariance quantities obtained between the recorded components as well as the normal and the tangential projections to estimate the off-diagonal elements of the covariance matrix. The factors include the positions of all five machine axes at the target point as well as the measurement direction. The repeatability models are validated by comparing measured and predicted values for a separate validation data set, which shows that a quantitative prediction of the randomness of on-machine measurement is achievable. The potential effects of the probe orientation, the hysteretic behaviour of the measurement system, the measurement strategy and the time span on the on-

---

[*] Corresponding author
[a] Department of Mechanical Engineering, Polytechnique Montreal, Montreal, QC H3T 1J4, Canada

machine probing are also studied through different experiments on a ring gauge. The effect of hysteresis on probing repeatability was found negligible but biases were detected.

Keywords: On-machine probing; Repeatability; Covariance matrix; Machine tool; Random errors; Hysteresis.

4.2 Introduction

On-machine probing is the practice of using a machine tool to measure parts while they are still on the machine rather than moving them to the metrology room. This allows manufacturers to correct the process mistakes and rectify the geometric errors on the part before removing the part from the machine tool. Such closed-loop machining process increases the productivity and decreases the scrap machined parts, which makes on-machine probing appealing to the part manufacturers. However, the geometric and dynamic errors of the machine tool, the errors of the probing system, as well as the thermal effects can adversely affect the quality of the on-machine measurement [4]. This gives rise to the complexity and, at the same time, the importance of studying the random behaviour and the repeatability of machine tools in the probing mode.

VIM defines random error as “component of the measurement error that in replicate measurements varies in an unpredictable manner” [3]. Then, random effects are characterized by two main attributes: variability and unpredictability. Although any observable error can have a systematic cause, the trade-off between compensation for all detectable errors and the costs of evaluation leads to classifying part of the errors as random effects. According to VIM, a difference between systematic and random errors is that systematic effects are measured with respect to a reference quantity value, which is usually provided by a calibrated artifact. Unlike systematic errors, the random effects of a system are quantified against the most probable outcome of the system. VIM refers to this reference as “the average that would ensue from an infinite number of replicate measurements of the same measurand”. As a result, random errors can be measured without using any calibrated reference.

The random behaviour of a system can be quantified by statistical analysis of a population made of a finite number of its possible outcomes. A randomness evaluation is based on the practice of repeating independent trials. Since the number of trials or population members is finite, any

assessment of the random behaviour of the system is an estimate. Statistical measures describing how outcomes are dispersed around a reference value comply with the definition of random errors and can give a quantified picture of the random behaviour of a system [3]. In this regard, standard deviation is typically used to evaluate the randomness of a phenomenon based on a finite number of trials [42]. When it comes to measurement systems, an incorrect estimate of random effects can lead to wasted time, effort and material. Making a reliable assessment of the system repeatability is necessary for uncertainty evaluation of any measurement result.

The current standards for machine tool testing have certain limitations that do not allow a reliable assessment of the repeatability of on-machine probing. ISO 230-2:2014 [64] proposes instructions to measure the positioning repeatability of a single axis of a machine tool. ISO 230-6:2002 [65] extends the repeatability evaluation from single-axis movements to diagonal paths traveled by the simultaneous movements of two or three linear axes. Based on these standards and mostly by using laser interferometers, the accuracy and repeatability of axis positioning in CNC machines have been studied [63, 66, 67]. However, these standards exclude addressing the various positioning of the tool with respect to the workpiece resulting from the movement of all machine axes in a 5-axis machine tool. ISO 230-10:2016 [68] includes instructions for the evaluation of probing repeatability, computed as the range of recorded values in the X, Y, and Z-axis coordinates in a specific position of the machine, for single-point surface measurement as well as for measuring circle and sphere centre location. This definition of repeatability, however, is not appropriate for measurement uncertainty evaluation purposes, for which the system repeatability must be estimated through standard deviation and covariance analysis [1, 42]. In addition, it is desirable to develop methods for estimating the repeatability of on-machine probing at any position of the working volume of the machine tool with different probing directions. Such investigation is missing in the current standards and the literature of machine tool testing.

For decades, the contact probe on a coordinate measuring machine (CMM) has been a de facto standard of data acquisition for off-line part inspection in manufacturing. Due to the similarities between a CMM and a machine tool, it is worth reviewing the related works on the evaluation of the repeatability of the CMM measurements. Compared with the studies conducted on the repeatability of CMMs, metrological capacities of machine tools have been less considered. ISO 15530-3:2011 [1] specifies the evaluation of measurement uncertainty associated with the

outcomes of a CMM measurement using an uncertainty evaluation technique known as “substitution method”, which is a part-centred approach that reveals little information about the random behaviour of the measurement system (i.e., CMM). In this standard, measurement uncertainty is calculated as a function of machine repeatability as well as the uncertainties of calibrated values, error compensations, and the similarities assumed between the part and the calibrated artifact. Woźniak and Jankowski [69] defined a new parameter describing the repeatability of angular positioning by a CMM articulated head. They determined the repeatability of the articulated head by comparing the errors occurring by engaging the articulated head and those occurring when only the probe was employed. They repeated five times a 25-point sampling on a reference sphere with and without turning the articulated head between the measurements. Determining the repeatability of the articulated head for different stylus lengths, they showed that these values are larger than the errors specified by the manufacturer. Woźniak [70] also proposed a procedure to determine the repeatability of the magnetic joint performance used in the automatic stylus or probe module change racks of a CMM by measuring a sphere centre with and without magnetic joint effects. For automatic and manual replacement of magnetic joints, they proposed different test and assembly procedures to examine the effects of replacement direction and the length of stylus. They observed that the automatic replacement for large probes with heavy and long styli might improve the repeatability in comparison with manual replacement.

As a prerequisite for uncertainty estimation, the repeatability of CMMs can be evaluated via different techniques and equipment. The Lasertracer, based on linear interferometry technology and the quadrilateration principles, is used to measure both the accuracy and the repeatability of positioning of a CMM [56, 71]. In the setup of a Lasertracer, the probe of a CMM is replaced with a retro-reflector. As a result, the associated uncertainty component is not considered. Accordingly, the errors of the probe must be evaluated separately [72, 73]. The repeatability of a CMM can also be evaluated by probing artifacts through various measurement strategies that engage both the CMM and the probing system at the same time [74-76]. Balsamo et al. [53] introduced the Expert CMM (ECMM) project aiming to evaluate the measurement uncertainty using the Monte Carlo (MC) method. They first estimated the geometric errors of CMM by a self-calibration procedure and then repeatedly measured an artifact in 100 different positions in the working volume of the CMM. Sladek and Gaska [56] developed an MC simulator for measurement uncertainty estimation.

Their algorithm evaluates the volumetric errors caused by CMM joint errors and probing deviations. They used a Lasertracer to estimate the geometric errors of the CMM. Residual errors (the systematic volumetric errors that remain uncompensated) caused by kinematic errors are determined at positions uniformly distributed at the nodes of a 3D Cartesian grid. They investigated the contribution of the probe head to the volumetric errors by probing a precision sphere under different probing strategies. They considered many parameters such as the angle between measurement direction and the normal vector of the measured surface, the roughness and form errors of the target surface, ball deformation, and stylus deflection. Zhong et al. [77] established a new S trajectory for R-test measurements to evaluate the dynamic accuracy of five-axis machine tools. They considered the repeatability of the machine tool, the measurement uncertainty of the R-test and the repeatability of set-up operation to be the main contributors to the uncertainty of the new method. They conducted a thousand-trial MC simulation for measurement uncertainty evaluation. In another work, Zhong et al. [78] present a spherical strategy for double ball-bar measurement to evaluate the volumetric accuracy of a five-axis machine tool. They evaluate the uncertainty of the calibration process through the law of the propagation of uncertainties specified by the Guide to the Expression of Uncertainty in Measurement (GUM). Taking into account the same uncertainty sources including the machine repeatability and set-up operation as well as the ball-bar uncertainty, they validate the uncertainty evaluation by an MC method.

In this study, two precision spheres are used to quantify the repeatability (covariance matrix) of on-machine probing of a five-axis horizontal machining centre equipped with a touch-trigger probe. The spheres are probed repeatedly at multiple positions within the machine’s working volume with various approach directions. Polynomial functions are then fitted to the measured points that enable the standard deviations of on-machine probing to be estimated at any desired position and with any probing direction. Covariance models, including the polynomials of degree five, also are fitted to the covariance values measured between the recorded coordinates and projected components. In order to gain a better understanding of the sources of non-repeatability, the potential effects of the hysteresis behaviour of the measurement system are then studied through on-machine measurements of 24 points on the inner wall of a ring gauge with ordered and shuffled replicate measurements.

4.3 Methods and materials

Implementing on-machine measurement techniques to verify the geometric parameters of a machined product requires two main steps: eliminating systematic errors and evaluating the uncertainty of measurement results (Figure 4-1). Successfully dealing with these two steps can convert a machine tool to a traceable CMM [37]. However, many challenges have to be faced before meeting these conditions. Compensation for various kinematic errors propagated through the kinematic chain of a machine tool requires a periodic calibration of the machine. Variable machine thermal status with its level of activity and changes in the industrial environment condition also might cause variations in machine systematic errors. Moreover, probing repeatability must be quantified.

The uncertainty of measurement result is defined as a parameter reflecting the dispersion of the values that could be reasonably attributed to the measurand [3, 42]. This parameter reflects the lack of knowledge of true value of the measurand. After correction for determined systematic effects, measurement results remain only an estimate because of two uncertainty sources: random effects and imperfect corrections of the measurement result for the systematic effects [42]. Supplement 1 to the GUM [79] specifies the measurement uncertainty evaluation based on an MC method. Supplement 2 to the GUM [50] is a modification of the GUM uncertainty framework applicable to a multi-input multi-output measurement function. Regardless of employing either method, both variance and covariance evaluations of the uncertainty contributors are required. In an MC method, a joint probability density function (PDF) describes the random behaviour of measurement function inputs based on the covariance matrix of the inputs. Drawing input vectors at random, an MC simulator evaluates the random inputs through the measurement function and generates an output population, which encodes crucial statistical information about the output quantities, including measurement uncertainty and output covariance. The GUM uncertainty framework, which approximates measurement uncertainty through the Taylor-series linearization of measurement function, also requires the covariance matrix of the input values. As a result, any evaluation of measurement uncertainty must address the covariance matrix of considered contributors (Figure 4-1).

When the axes of a machine tool are driven to a position, due to a combination of systematic and random errors, the relative position of the tool with respect to the workpiece differs from the nominal relative position. The systematic portion of this deviation is not observable by the machine tool since it simply reports the coordinates based on its axes positions. To evaluate systematic errors, calibrated measuring equipment [67, 80] or calibrated artifacts [26, 81] are employed. Evaluating the random errors of on-machine probing, however, does not require calibrated artifacts because these errors are evaluated against the mean of repeated trials. Random deviations in the relative position of the tool frame with respect to the relevant workpiece feature frame manifest themselves in the recorded touch coordinates.

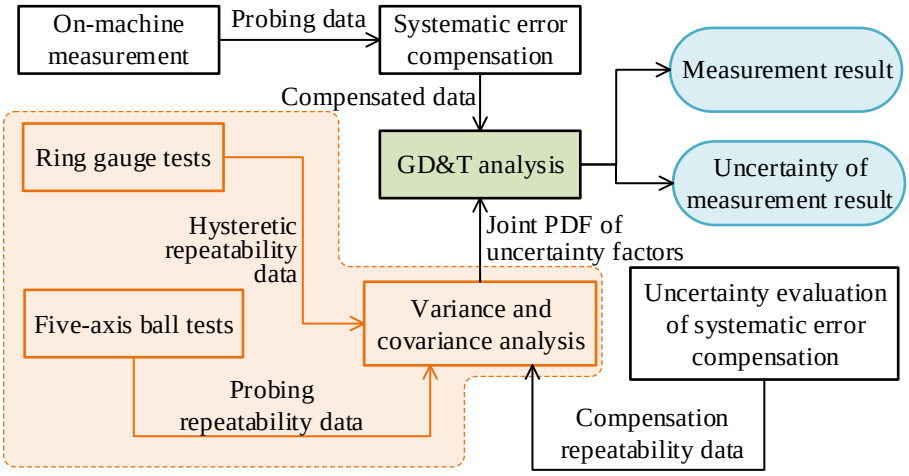

Figure 4-1: On-machine probing and the uncertainty evaluation of measurement results. In orange, the subject addressed in this paper.

4.4 Repeatability of on-machine probing

The repeatability of on-machine probing is evaluated as a covariance matrix of dimension 3×3, including the standard deviations (square roots of diagonal components) of recorded touch coordinates in a finite number of probing tasks and the covariance (off-diagonal components) between the recorded Cartesian coordinates. In case of employing the normal and the tangential projections of probed points, the measurement repeatability can be presented in the form of a covariance matrix of dimension 2×2. The repeatability of on-machine probing was investigated in

a five-axis ball test where two precision spheres of nominal diameter 25.400 mm and nominal stem lengths (from the mounting base to the ball centre) 76.20 and 152.40 mm are chosen as artifact. Target points on the balls were measured on a five-axis horizontal machining centre model HU40-T from Mitsui Seiki equipped with a Renishaw® MP 700 touch-trigger probe (Figure 4-2a). In order to evaluate the repeatability of on-machine probing, target point coordinates X_T, Y_T, and Z_T in the machine frame as well as rotary axes indexations B_T and C_T are chosen as experimental factors in the design of experiments (Figure 4-2b). In addition, the spherical coordinates θ and φ of a unit approach vector, expressed in a spherical coordinate system located at the artifact centre (Figure 4-2c) are also considered as experimental factors that would influence the probing performance. The polar and azimuthal axes of the spherical coordinate system are respectively parallel to the machine's Z and Y axes, i.e. Z_m and Y_m (Figure 4-2c). Before the design of experiments, the effects of probe orientation ω (Figure 4-2c) was investigated by probing the machine's pallet, in a "probe orientation" test. In this experiment, varying angle ω (spindle indexation) from 0° to 360° by increments of 45°, each measurement is repeated 50 times while the machine probing movement is kept unchanged along the X-axis of the machine, X_m (Figure 4-2d). This test led to small variations ($\approx$ 0.1 μm) in the standard deviation of the measurement results. Then, the probe orientation was disregarded in on-machine repeatability analyses.

The variation ranges of the experimental factors are listed in Table 4-1. Experimental factors were combined to form a total number of 50 target poses. Each target point was probed 30 times before moving to the next target point so that 1500 on-machine measurements were carried out. The standard deviation of the 29 values recorded for each of the X, Y and Z coordinates and probing angles at a target point as well as the covariance between the recorded values were taken as the repeatability of on-machine measurements for those conditions.

In order to obtain mathematical models capable of estimating the repeatability of on-machine measurements at any desired position, polynomial functions were fitted, in a least-square sense, to the standard deviations of the recorded X, Y, and Z coordinates at 50 positions as well as to the same results but projected normal and tangential to the target surface. Similarly, quintic polynomials were fitted to the covariance values between each pair of the recorded coordinates, including cov(X, Y), cov(X, Z) and cov(Y, Z), as well as those of the normal and tangential projections cov(N,T). These repeatability models use as independent input variables, the five

quantities representing the target pose X_T, Y_T, Z_T, B_T, and C_T (Figure 4-2b) as well as angles θ and φ defining the measurement direction (Figure 4-2c). Each standard deviation model f consists of 22 coefficients that can be expressed as:

$$f = \alpha_{f,0} + \alpha_{f,1}\varphi + \beta_{f,1}\varphi^2 + \alpha_{f,2}\theta + \beta_{f,2}\theta^2 + \gamma_{f,2}\theta^3 + \delta_{f,2}\theta^4 + \sum_{i=3}^{7} \alpha_{f,i}P_i + \beta_{f,i}{P_i}^2 + \gamma_{f,i}{P_i}^3 \quad 4\text{-}1$$

A covariance model g, consisting of 36 coefficients, is formulated as:

$$g = \alpha_{g,0} + \sum_{i=1}^{7} \alpha_{g,i}P_i + \beta_{g,i}{P_i}^2 + \gamma_{g,i}{P_i}^3 + \delta_{g,i}{P_i}^4 + \varepsilon_{g,i}{P_i}^5 \quad 4\text{-}2$$

where, in Eq. 4-1, P_i $(i = 3, \dots, 7)$ take on five experimental factors X_T, Y_T, Z_T, B_T, and C_T. In Eq. 4-2, P_i $(i = 1, \dots, 7)$ take on seven experimental factors X_T, Y_T, Z_T, B_T, C_T, θ, and φ. In these equations, $\alpha_{f,i}$, $\beta_{f,i}$, $\gamma_{f,i}$, and $\delta_{f,i}$ are the coefficients of standard deviation model f, and $\alpha_{g,i}$, $\beta_{g,i}$, $\gamma_{g,i}$, $\delta_{g,i}$, $\varepsilon_{g,i}$ are the coefficients of covariance model g.

To validate the models, eight additional target poses were randomly chosen within the working space of the machine. The points were repeatedly measured and the repeatability values of the recorded coordinates were compared with the values predicted by the models.

The spherical geometry of the artifacts provides the opportunity to approach the target surface in any desired direction. For machine tools, imperfections in the positioning of machine axes can result in deviations in both the relative translation and the relative orientation of the tool with respect to the workpiece. Having a three-dimensionally axisymmetric geometry, the spherical artifact decouples the direction of probing from the angular position of the sphere generated by the rotary axes, which ensures the isotropy of the approach direction to the target surface. However, the variable deviation from nominal in the relative position of the tool frame with respect to the stylus tip position is likely to affect the recorded coordinates in replicate measurements. The relative translation when triggering occurs, including both the systematic and random errors, can be described by a longitudinal component a and a lateral component b, respectively aligned with and perpendicular to the nominal approach direction (Figure 4-3). The longitudinal component manifests itself directly in the coordinates recorded by the machine. Although the machine is

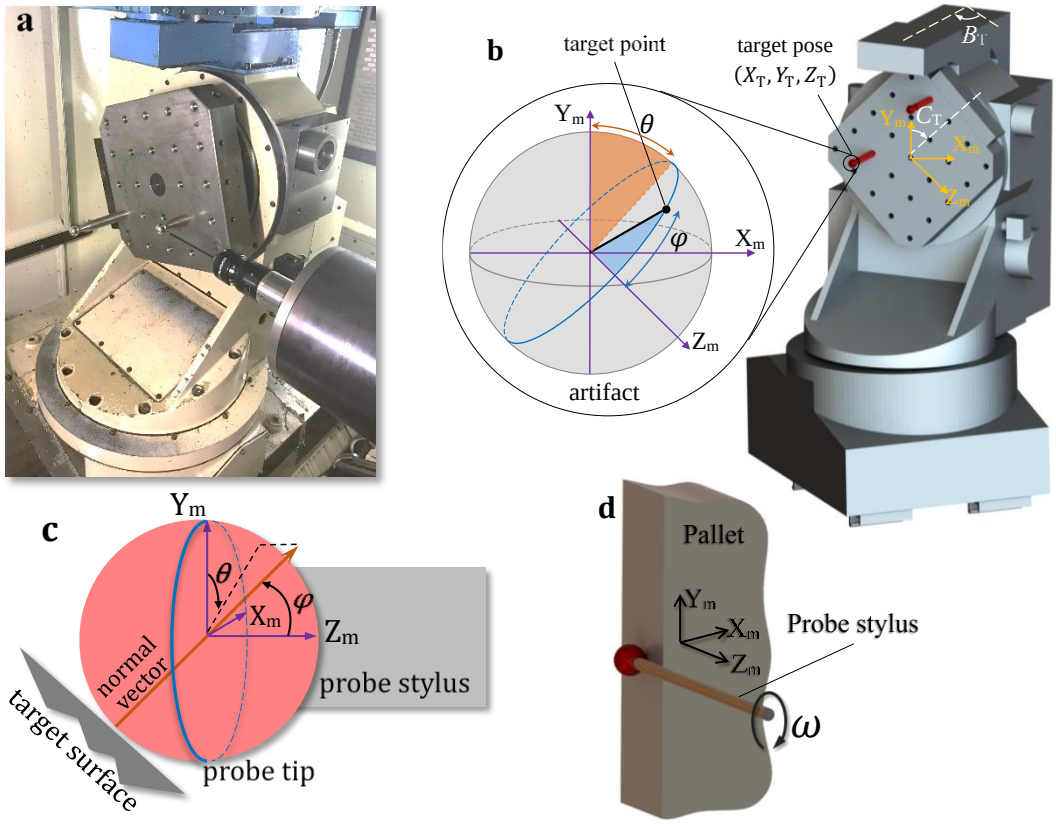

Figure 4-2: a) Experimental setup of five-axis ball tests including the precision spheres and the touch-trigger probe mounted on the five-axis machine tool. b) The target pose coordinates X_T, Y_T, and Z_T in the machine frame as well as the indexations of rotary axes B_T and C_T considered as machine factors in the design of experiments for the repeatability evaluation of on-machine measurements. Also shown are c) the polar φ and azimuthal angle θ of the approach direction, and d) the probing strategy of the probe orientation tests used to study the effects of probe orientation ω, around the probe axis, on measurement repeatability.

Table 4-1: Variation ranges of the experimental factors in the repeatability evaluation of on-machine measurements.

	φ (degree)	θ (degree)	B_T(degree)	C_T (degree)	X_T (mm)	Y_T (mm)	Z_T (mm)
Min	0	0	-90	-180	-220	-170	-110
Max	+90	+360	+90	+180	+230	+180	+220

of the relative lateral deviation b' in the touch position, this component might affect the recorded coordinates because of the resulting change in the longitudinal position at trigger time. Considering the radii of employed artifact and stylus tip with respectively nominal values of 12.700 and 3.000 mm, a lateral translation of $b' = 125.3$ µm is required to change the approach distance along the nominal approach direction by $d = 0.5$ µm, which is equal to the machine resolution. That is, the random lateral deviation of the tool frame with respect to the workpiece frame in replicate measurements must be significantly large to affect the coordinates recorded by the machine, which is less likely to occur in reality. Although the probe would already deviate laterally by up to 100 µm due to the machine systematic errors, findings of this research show that the variation range of lateral deviations caused by random errors rarely exceeds 4 µm. Therefore, sphere is a suitable artifact for repeatability evaluation due to its isotropy of probing directions and its insensitivity to the relative rotation and the randomness of relative lateral translation of the stylus tip with respect to the master sphere in replicate measurements.

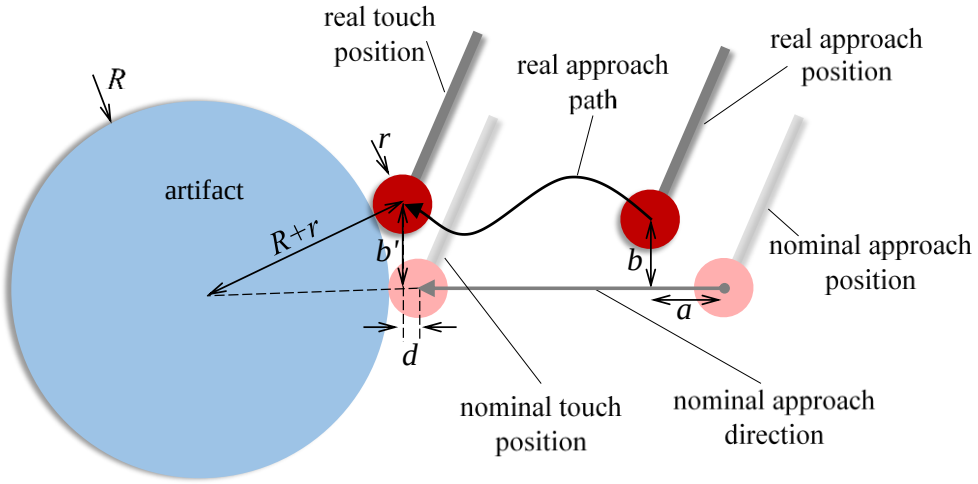

Figure 4-3: Schematic illustration of the effect of relative translation of the tool with respect to the workpiece on the approach distance along the nominal approach direction.

4.5 Hysteresis of the measurement system

Hysteresis is an error source arising from the fact that a system response to an input can be affected by the preceding inputs [82]. For example, touch probe hysteresis mainly results from friction at

the sitting contact in a touch-trigger probe structure and can be magnified by elastic deflection of the stylus [83]. This phenomenon occurs when there is a change in the measurement direction, where the friction in the sitting contacts prevents the probe stylus from recovering its neutral position when the contact ends [84]. Backlash on machine tools is another example. Both systematic and random effects of hysteresis are measured by means of a "probing hysteresis test", which includes the hysteresis effects of both the machine axes and the touch-trigger probe. In this test, 12 target points uniformly distributed ($\psi = 0°, 30°, \dots, 330°$ in Figure 4-4a) around the inner wall of a ring gauge of the nominal diameter of 63.50 mm were measured. The ring gauge centre was positioned at the x=y=0 position of the machine. For each target point, two probing results, as the X, Y and Z-axis machine readings were recorded: the first probing follows the probing of the same target point, while the second follows the probing of the ring wall on the opposite side of the target point (Figure 4-5a). By doing so, the two recorded results are different by the hysteresis being involved. The probe retracts to the ring centre after each probing. This procedure is repeated 24 times. The effect of hysteresis is then investigated by calculating the average radial projections and the corresponding standard deviations obtained for each of the two data sets.

In this test, the potential hysteretic effect of the machine axes on changing the previously measured point might be partially erased by the approach motion to the point to be probed. Then, to study the hysteresis effect of the X and Y axes, only the four target points ($\psi = 0°, 90°, 180°, 270°$ in Figure 4-4a) along these axes were probed for the "axis hysteresis test". In this experiment, two probing results were recorded for each target point: the first follows approaching (without touch) the ring wall along the positive direction of the cross axis, and the second follows approaching (without touch) the ring wall along the negative direction of the cross axis (Figure 4-5b). For the two data sets, the hysteresis effect of the X and Y axes are then investigated by calculating the average radial projections and the corresponding standard deviations.

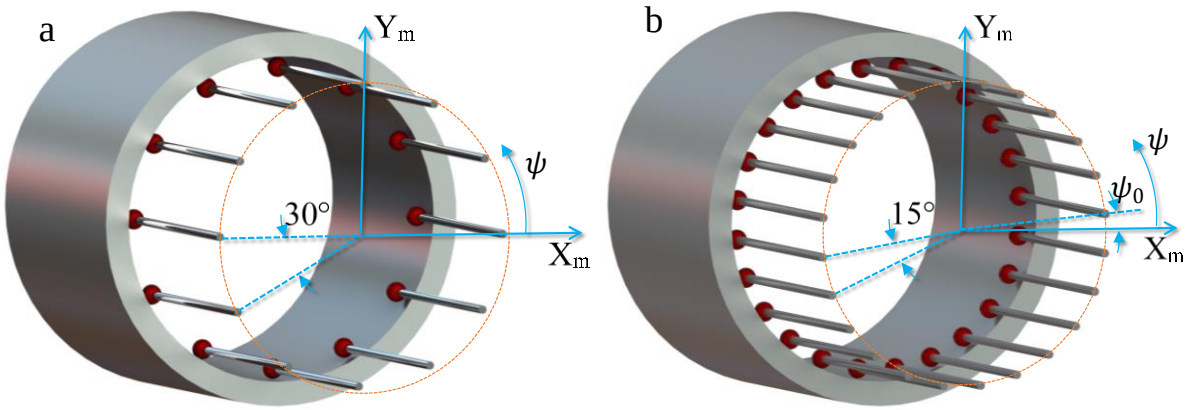

Figure 4-4: Target points in a) the probing hysteresis and axis hysteresis tests (For the axis hysteresis tests, only the target points at $\psi = 0°, 90°, 180°, \text{and } 270°$ were probed), and b) the simple, shuffled and ordered ring gauge.

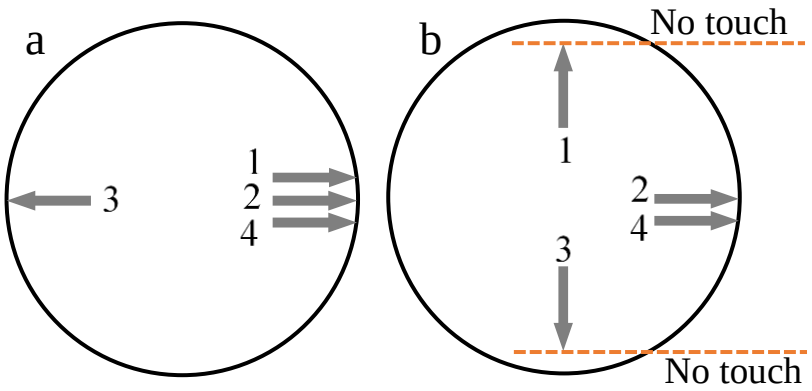

Figure 4-5: Measurement strategy adopted in each cycle of a) the probing hysteresis test and b) the axis hysteresis test. After each measurement, the probe retracts to the ring centre.

4.6 Probing strategy and time span

It is well understood that thermal effects systematically influence machine accuracy. However, the effect of thermal variations of the machine tool on its random behaviour in both machining and probing still needs to be addressed in more detail. Depending on the strategy adopted for replicate measurements in repeatability evaluation, probing duration might vary between a few minutes to a few hours. During this period, the machine performance gradually alters due to the thermal loadings caused by the heat generated by the various machine sub-systems as well as the thermal exchanges

with the environment. Moreover, the machine axes might move differently between two replicate probing tasks. To study the effect of probing strategy and the time span of repeated measurements, the 24 points shown in Figure 4-4b were measured under three different measurement strategies. For the first strategy, each target point was probed 50 times before moving to the next target point so that all measurements at a target point are gathered in a relatively short time. In this measurement strategy, referred to as "simple ring gauge" test, replicate measurements of each point are completed in almost 12 min. Then for the second strategy, the 24 points were measured once one after another and this cycle was repeated 50 times, referred to as "ordered ring gauge" test. The third strategy involves measuring the 24 points in a randomly shuffled order until each point is probed 50 times, referred to as "shuffled ring gauge" test. The three ring gauge tests were conducted with two indexations of the initial target point $\psi_0 = 0°$ and $\psi_0 = 7.5°$ (Figure 4-4b). In the three ring gauge tests, the approach position was at the centre of the ring gauge and the probe retracts to the centre after each probing. The ordered and shuffled ring gauge tests each lasted almost five hours to complete the replicate measurements of each target point. The temperature of the machine chamber was measured during the ordered and the shuffled ring gauge tests. The resolution of the employed thermometer is one °F. The standard deviation of the repeated measurements was calculated to quantify the measurement repeatability.

4.7 Results and discussion

4.7.1 Probe orientation

The probe orientation test (Figure 4-2d) was carried out to study the effect of spindle indexation, and thus probe orientation around its axis, on the repeatability of recorded data. Changing the probe orientation ω from 0° to 360° results in small changes in the repeatability of on-machine measurements with a peak-to-valley variation of 0.08 μm (Figure 4-6). Part of these variations can be explained by the random behaviour of the touch-trigger probe. Pre-travel variation causes the majority of touch-trigger probe errors [85]. This error is the distance traveled by the probe between the points where the probe touches a target and where triggering occurs. Although treated as the systematic behaviour of a touch-trigger probe, pre-travel also has a random nature [86]. Wozniak and Jankowski [87] showed that although smaller than systematic errors, random errors contribute

to the unidirectional repeatability of touch-trigger probes. As a result of the probe orientation test, probe orientation ω was disregarded so that the repeatability of on-machine measurements was evaluated considering the seven parameters, listed in Table 4-1.

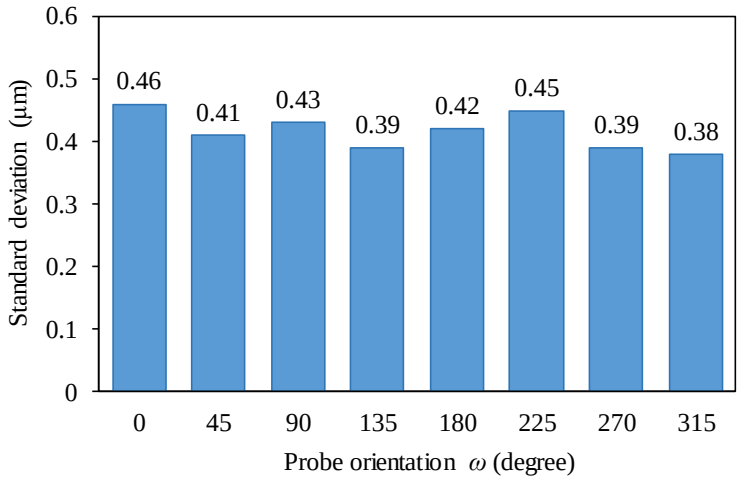

Figure 4-6: The repeatability of on-machine measurements versus the probe orientation ω in the probe orientation tests (Figure 4-2d).

4.7.2 Repeatability models of on-machine measurements

The coordinates recorded by the five-axis ball tests suggest that most of the first recorded values, among the 30 repeated measurements at each position, were singularly deviated from the average (Figure 4-7). This is thought to be due to hysteresis because the first touch has a preceding motion, which is different from subsequent touches. In order to prevent this outlier affecting the standard deviation of each sample, the first probing result was ignored in the standard deviation calculations. Given that this study separately addresses the hysteretic effects (section 4.7.3), disregarding the first deviated indication prevents the model from double counting this effect.

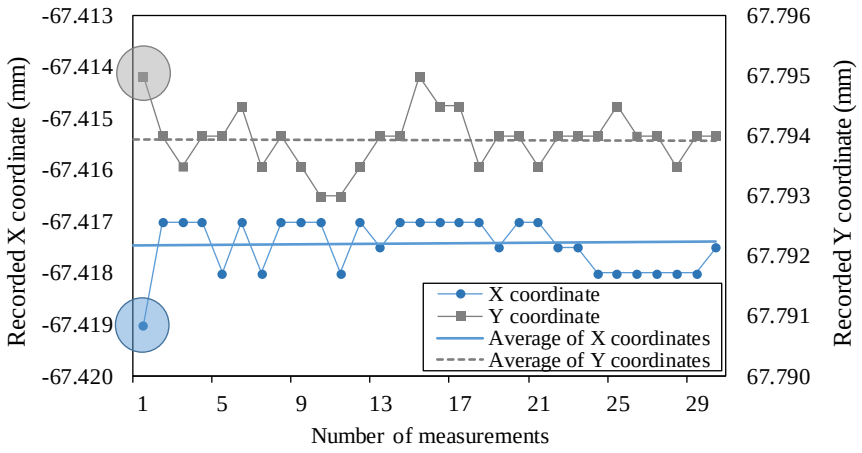

Figure 4-7: Typical X and Y coordinates recorded in the replicate measurements for the five-axis ball tests obtained for nominal target pose $X_T = -68.8$, $Y_T = 69.7$, $Z_T = 110.6$, $B_T = -54°$, $C_T = -180°$, $\varphi = 90°$ and $\theta = 144°$. The polar angle of the approach direction is $\varphi = 90°$, thus the probe moves in the XY plane resulting in no variation in Z coordinate.

4.7.2.1 Standard deviation models

On-machine measurement repeatability models of the machine give the machine repeatability for any point and measurement direction. The seven inputs (X_T, Y_T, Z_T, B_T, C_T, φ and θ) of the repeatability models are obtainable from the measurement G code. The R-squared values (coefficients of determination) of the fitted standard deviation models are 92%, 81%, and 90 %, respectively for the X, Y, and Z coordinates (Figure 4-8a-c). The models are then used to predict the standard deviations at the eight validation points, randomly chosen within the working volume of the machine, with maximum errors 36%, 34%, and 33% for the X, Y, and Z coordinates, respectively (Table 4-2). The magnitudes of the maximum differences between measured and predicted values are 0.24, 0.09, and 0.12 μm, respectively.

One of the conditions of regression models for a valid least-squares fit is that the fitted residuals are normally distributed [88]. To verify this condition, the histograms of residuals of the repeatability models were visually inspected (Figure 4-8d-f). Considering the fact that the theoretical percentiles of the normal distribution versus the observed sample percentiles should be approximately linear [88], normal probability plots can give a more reliable picture of the quality of the fitted functions. The normal probability plots of the residuals pass approximately through

zero and are nearly linear (Figure 4-8g-i), suggesting the condition that the residuals are normally distributed is met. No extreme outlier is present and the residuals are reasonably bounded resulting in non-heavy tailed distributions. Therefore, the residuals of the fitted models can be considered as "well-behaved". Higher-order polynomial functions, i.e. quartic, was also examined, which were fitted with higher R-squared values though inaccurately estimated the validation data, probably due to over-fitting.

In the uncertainty analysis of single point measurement, the repeatability of the three recorded Cartesian coordinates contributes to the uncertainty associated with the position reported for a target point. In general, this is important for the evaluation of certain tolerances of freeform surfaces, for example in airfoil blade inspection where airfoil profile should be reconstructed under the uncertainty of inspection data points [89, 90]. However, in many metrological applications, the final measurand, such as a surface flatness, or a hole roundness, is mostly insensitive to any variation parallel to the target surface. In this regard, having the machine repeatability along the measurement direction and in a local coordinate frame positioned at the target point with normal and tangential axes with respect to the target surface will be more practical. Accordingly, repeatability models that receive the target pose and the measurement direction and return the repeatability along the nominal measurement direction, as well as tangent to the target surface, are fitted to the measured points. The R-squared values of the standard deviation models are 84% and 82% (Figure 4-9a and b) respectively for the normal and tangential projections. The models predict the standard deviation of on-machine measurement for the eight verification points with maximum errors of 38% and 27% (Table 4-2), denoting maximum difference magnitudes 0.34 and 0.05 μm for the normal and tangential directions, respectively. The normality of the residuals (Figure 4-9c and d) were examined through the normal probability plots (Figure 4-9e and f).

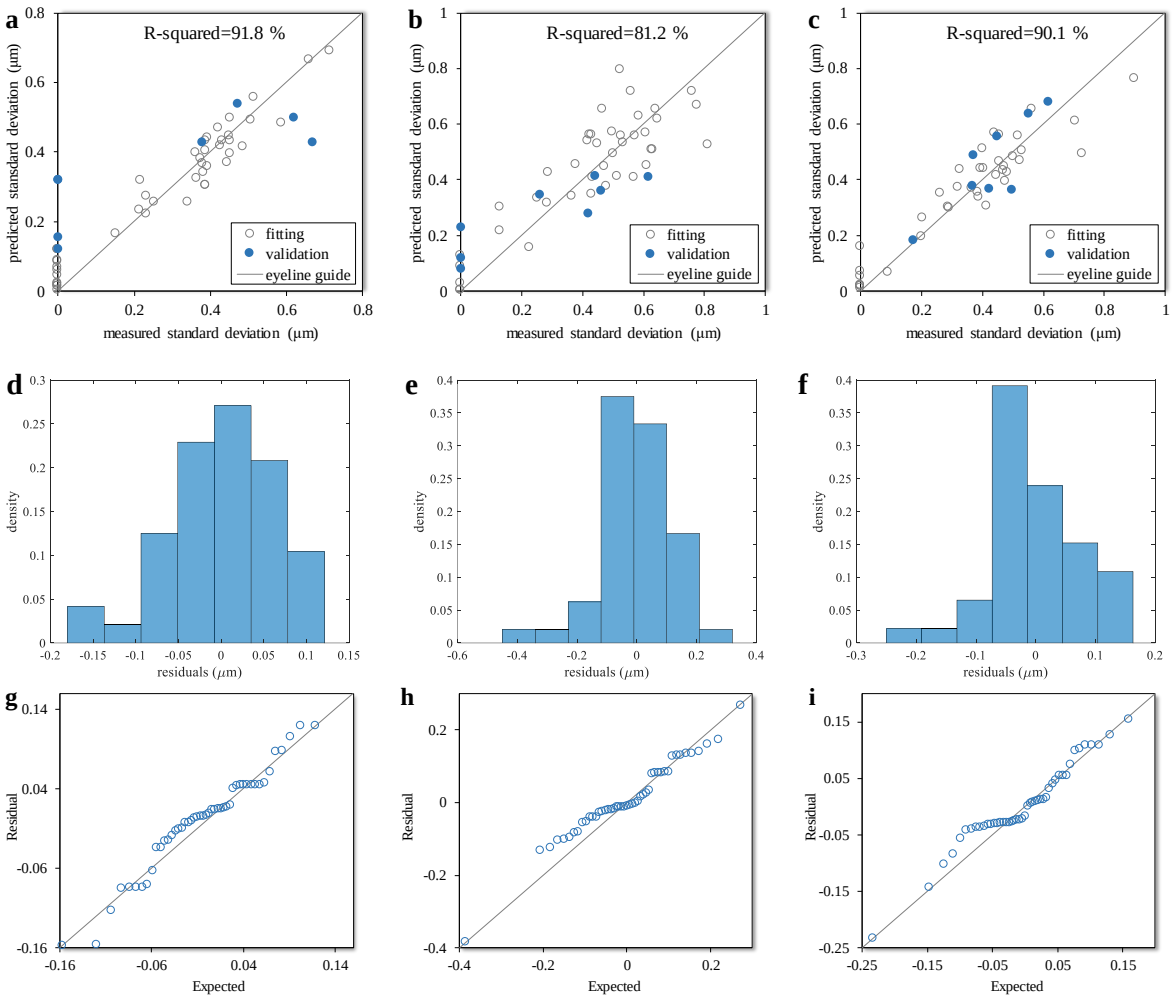

Figure 4-8: Regression plots of the values measured versus the values predicted by the probing standard deviation models for: a) the X coordinate, b) the Y coordinate, and c) the Z coordinate. The non-filled and filled markers represent the measurement results used to fit and to validate the probing repeatability models, respectively. The residual histograms obtained by fitting the standard deviation models to the: d) X coordinate, e) Y coordinate, and f) Z coordinate. Normal probability plots obtained for the recorded g) X coordinate, h) Y coordinate, and i) Z coordinate.

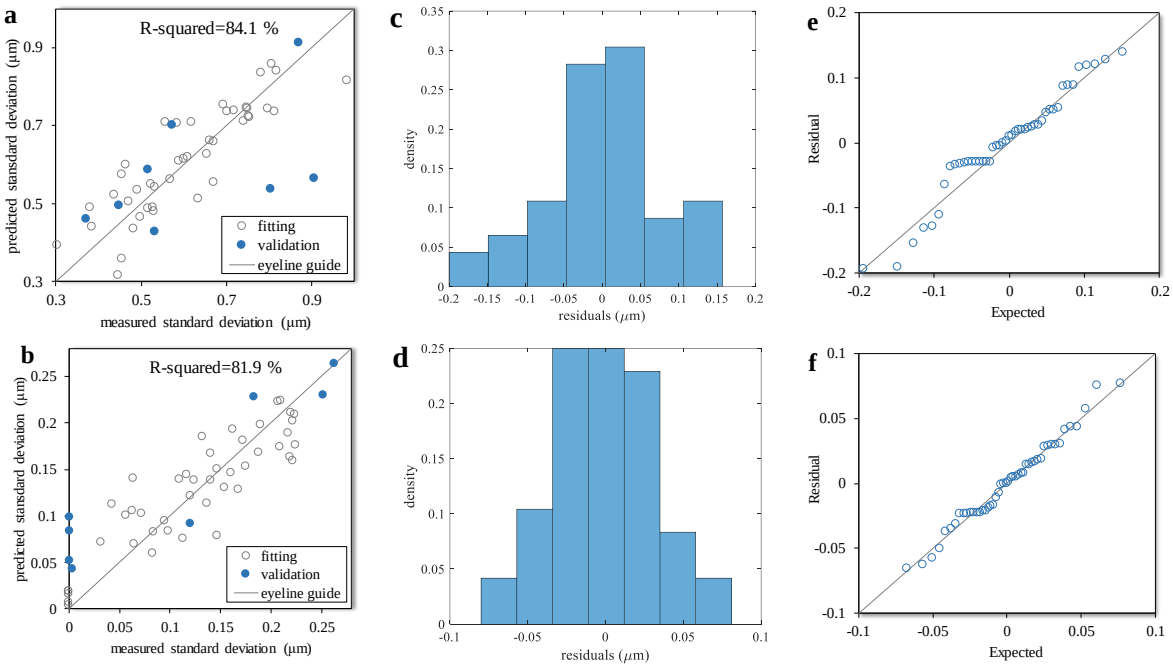

Figure 4-9: Regression plot of the values measured versus the values predicted by the probing standard deviation model a) perpendicular to the target surface and b) tangent to the target surface. The non-filled and filled markers represent the measurement results used to fit and to validate the probing repeatability models, respectively. The residual histograms obtained by fitting the standard deviation model c) perpendicular to the target surface and d) tangent to the target surface. Normal probability plot e) perpendicular to the target surface and f) tangent to the target surface

Table 4-2: Validation of the standard deviation models of on-machine measurements.

	Experimental factors							Error (%)				
	φ (degree)	θ (degree)	B_T (degree)	C_T (degree)	X_T (mm)	Y_T (mm)	Z_T (mm)	X	Y	Z	N	T
1	45	180	-90	120	-153.5	-158.3	-89.6	32.1	33.3	10.6	5.1	22.7
2	60	240	-60	-180	-36.5	74.5	114.3	35.8	21.6	26.3	37.6	11.5
3	60	240	-60	-180	-102.4	-165.5	152.4	13.0	6.4	3.6	22.8	7.6
4	0	240	0	0	-80.0	-80.0	90.0	15.6	7.9	32.5	24.6	4.5
5	0	240	0	0	-80.0	160.0	166.2	12.0	12.0	24.1	10.7	9.9
6	15	240	30	-60	-58.8	27.6	133.8	31.9	22.8	15.8	19.7	14.4
7	60	240	60	-120	212.7	-16.2	-71.6	19.9	33.0	12.7	33.2	1.7
8	45	180	-90	120	-153.5	-158.3	-89.6	14.1	33.9	6.8	14.2	27.0

In order to provide a picture of the effects of each factor on the repeatability and its variations, Table 4-3 quantitatively summarizes the standard deviation model. The columns include the mean of the indicated output as well as its average gradient with respect to each of the seven experimental factors. In each row of this table, the indicated factor is incrementally varied over its range, specified in Table 4-1, and the average values as well as the absolute gradients of the model are calculated. In this table, the factors other than the considered variable are fixed in a way that the machine axes are set at their central values (Table 4-1) and the approach direction is $[\varphi, \theta]=[45°, 45°]$.

Figure 4-10 shows the variations of the standard deviation functions with respect to the frame of the last axis (the C-axis) of the workpiece branch of the machine tool, which includes the X, B, and C-axis. The five-axis ball tests are conducted in a way that after completing each probing task and before starting the next repetition, all the five axes of the machine retract to their zero positions. As a result, although rotary axes B and C are fixed while the touch-trigger probe picks the coordinates, these axes contribute to the repeatability of probing results due to their unrepeatable positioning through the replicate measurements. In Figure 4-10, the axis positions other than the independent factors of each graph are fixed at their central values (Table 4-1) and the approach direction is $[\varphi, \theta]=[45°, 45°]$. The positions of axes B and C have little effect on the repeatability of the recorded Z coordinates (Figure 4-10c), whereas they are more likely to affect the X (Figure 4-10a) and Y (Figure 4-10b) coordinates, where larger gradients are observable for the standard deviation functions (Table 4-3). The maximum standard deviation of the recorded X coordinate exceeds 0.40 μm (Figure 4-10a) at the extremes of the B and C-axis.

Figure 4-10d-f illustrate the variations of on-machine measurement standard deviation with respect to the B and X-axis of the machine. The repeatability of the Y coordinate (Figure 4-10e) varies more with respect to the X-axis than what is shown in Figure 4-10b for the B and C-axis (Table 4-3). As Figure 4-10e illustrates, for all values of the B-axis the repeatability of the Y coordinates improves at the negative extreme of the X-axis. The standard deviations of the recorded Y (Figure 4-10e) and Z (Figure 4-10f) coordinate reach 0.55 and 0.70 μm, respectively. Figure 4-10g-i show the recorded standard deviations of the coordinates versus the positions of the C and X axes of the machine. The maximum standard deviation of the recorded Y coordinate (Figure 4-10h) is 0.62 μm at the zero positions of the C-axis, and that of the recorded Z coordinate (Figure 4-10i) exceeds 0.7

μm. The effect of the prismatic X-axis on the repeatability of on-machine measurement is more significant in the recorded Y coordinates (Figure 4-10h), where a larger gradient is observable along the machine X-axis (Table 4-3).

Figure 4-11 shows the repeatability variations with respect to the axes of the tool branch, Z and Y axes. The standard deviation of measured X coordinates is smaller than 0.30 μm (Figure 4-11a) and its variations with respect to the Z-axis are small in all the positions of Y-axis (Table 4-3 and Figure 4-11a). The maximum standard deviation of the Y (Figure 4-11b) and Z (Figure 4-11c) coordinates reaches 0.80 and 0.58 μm, respectively. According to Table 4-3, the average gradient of standard deviation model with respect to the Y-axis is among the largest. This implies a more significant role of this axis in the repeatability variations of on-machine probing. Particularly, the Y-axis position dramatically varies the recorded Y coordinate with an average gradient of 0.0089 μm/mm.

Table 4-3: The average of standard deviation and the average of absolute gradient of the standard deviation model with respect to the experimental factors. For each row, the variable other than the indicated factor is fixed so that the machine axes are fixed at their central values (Table 4-1) and the approach direction is $[\varphi,\theta]=[45°,45°]$.

	Average of standard deviation (μm)					Average of absolute gradient (μm/unit)				
	X	Y	Z	N	T	X	Y	Z	N	T
φ (degree)	0.18	0.57	0.36	0.78	0.10	0.0033	0.0052	0.0068	0.0044	0.0027
θ (degree)	0.30	0.50	0.48	0.74	0.20	0.0044	0.0039	0.0054	0.0062	0.0012
B_T (degree)	0.19	0.57	0.46	0.61	0.16	0.0034	0.0033	0.0009	0.0111	0.0009
C_T (degree)	0.21	0.56	0.44	0.85	0.15	0.0017	0.0015	0.0004	0.0041	0.0001
X_T (mm)	0.20	0.51	0.44	0.65	0.13	0.0024	0.0057	0.0007	0.0082	0.0024
Y_T (mm)	0.19	0.60	0.44	0.84	0.16	0.0022	0.0089	0.0060	0.0149	0.0009
Z_T (mm)	0.21	0.58	0.45	0.71	0.16	0.0007	0.0029	0.0023	0.0073	0.0009

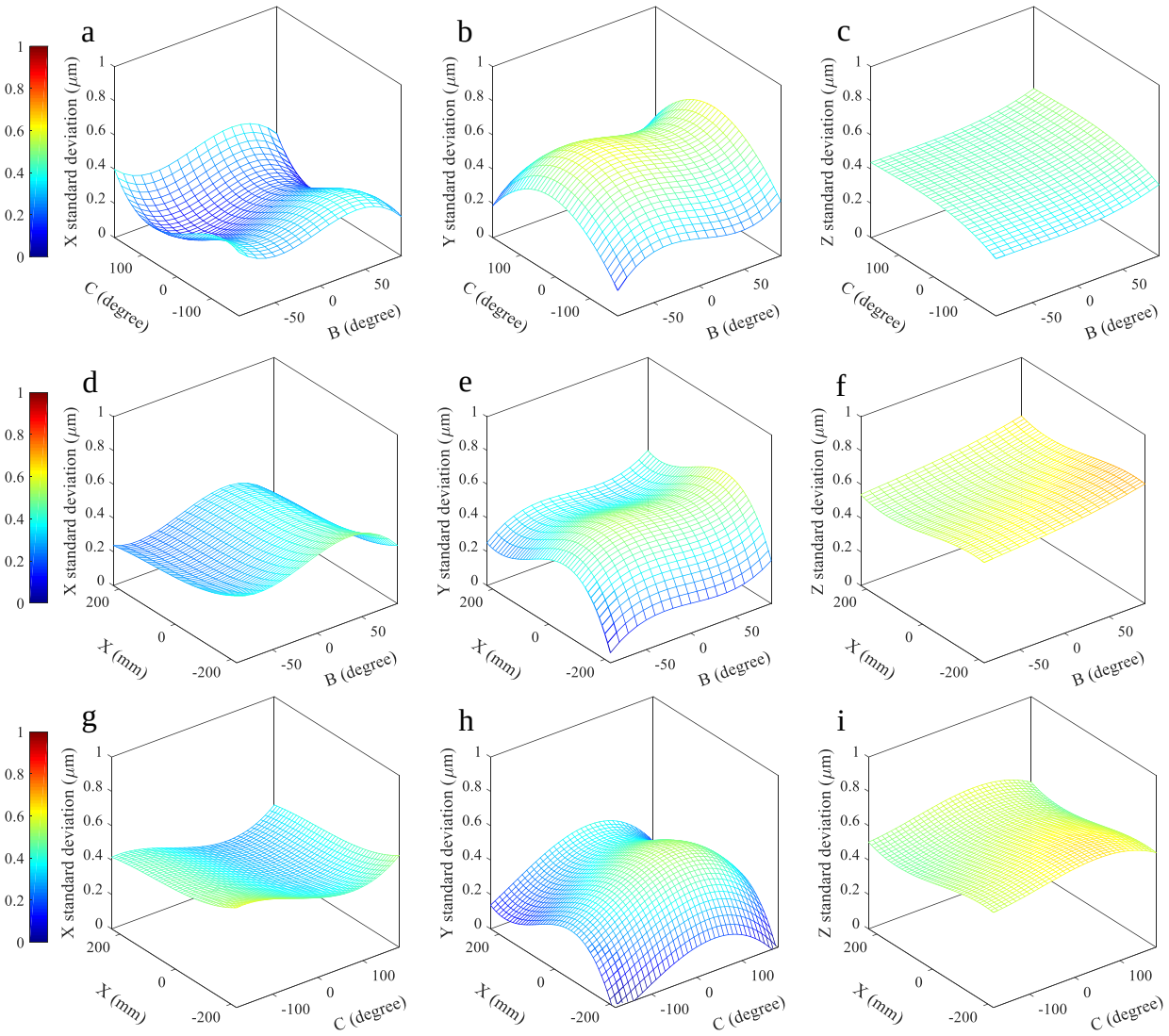

Figure 4-10: The standard deviation of on-machine measurements versus the positions of the workpiece branch axes: a-c) B and C; d-f) B and X; and g-i) X and C. The other independent parameters are fixed at their central values (Table 4-1) and the approach direction is $[\varphi,\theta]=[45°,45°]$.

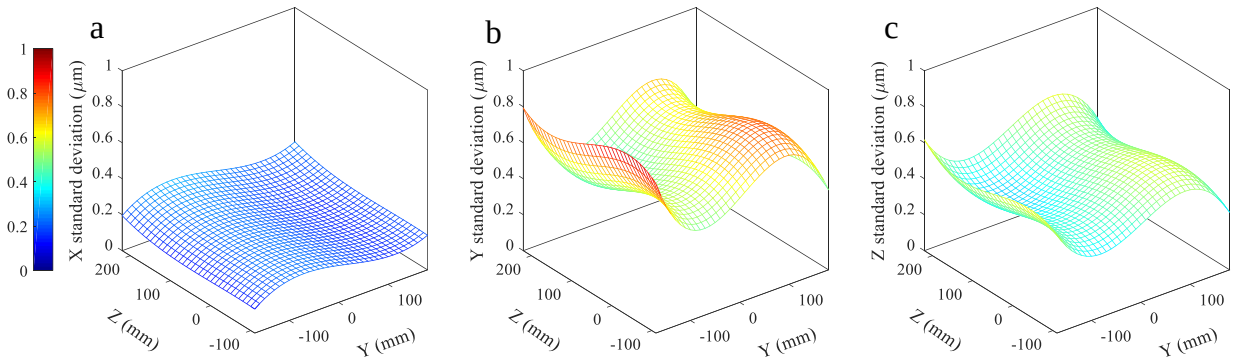

Figure 4-11: The standard deviation of on-machine measurements versus the positions of the tool branch axes Z and Y. The other independent parameters are fixed at their central values (Table 4-1) and the approach direction is [φ,θ]=[45°,45°].

Figure 4-12 depicts the polar plots of the standard deviation models with respect to the polar φ and azimuthal θ angles of the approach direction. The repeatability plots of the recorded X and Y coordinates (Figure 4-12a and b) are more stretched along the machine X (θ=90°) and Y (θ=0°), respectively. The repeatability of these coordinates improves by decreasing the azimuthal angle of the approach direction. Smaller plots of the recorded X coordinates implies more repeatability of the machine X-axis. The plots of the recorded Z coordinates (Figure 4-12c) are more circular compared with the other two prismatic axes of the machine that might be caused by the symmetry of the Z-axis movement with respect to the polar angle φ of the approach direction. Because of fitting residuals, the model fitted to the recorded Z coordinates does not pass through zero at φ =90°. As expected, the standard deviation of the recorded coordinates projected on the normal (radial) direction (Figure 4-12d) is considerably larger than those projected on the tangential direction (Figure 4-12e).

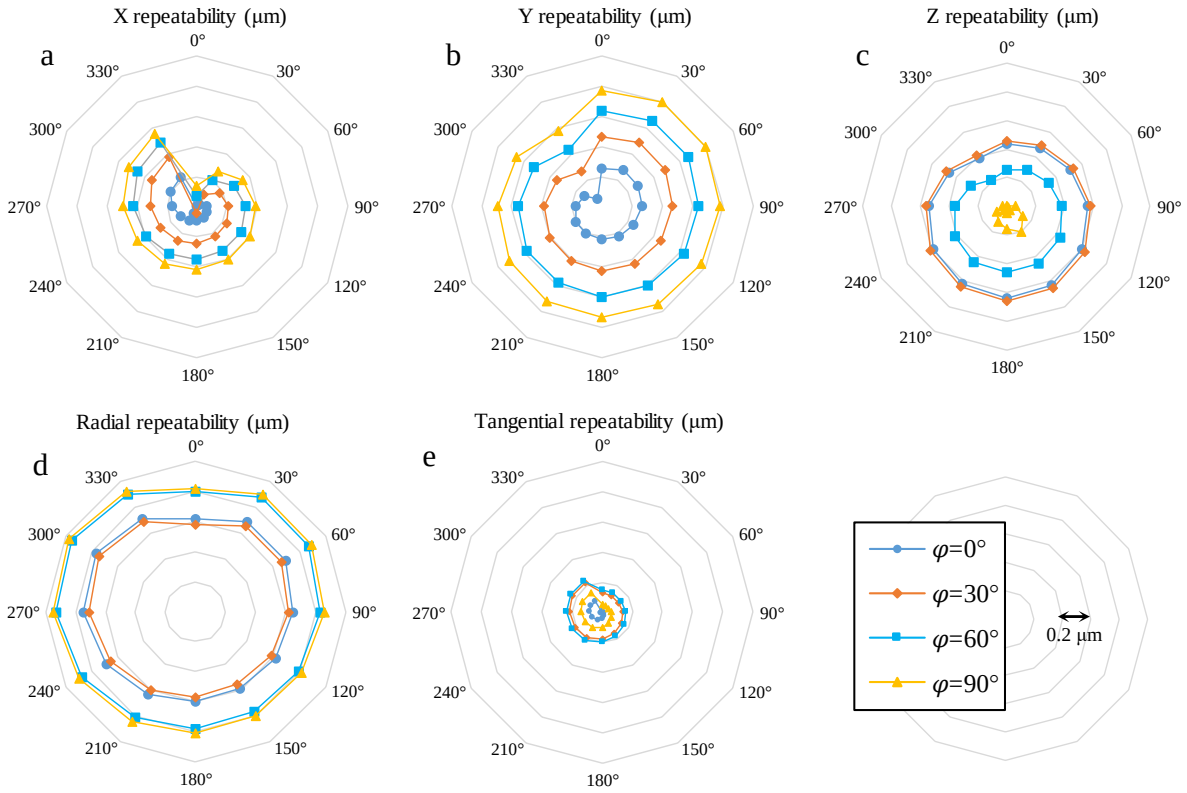

Figure 4-12: The polar plots of the standard deviation predictions from the model versus the polar φ and azimuthal θ angle of the approach direction for the a) X coordinate, b) Y coordinate, c) Z coordinate, d) normal (radial) projection, and e) tangential projection of the Cartesian readings. The other independent parameters are fixed at their central values (Table 4-1).

4.7.2.2 Covariance models

Studying the correlation coefficients and the p-values obtained through hypothesis testing revealed some strong correlations between the recorded coordinates under specific measurement conditions. The repeatability analysis of a machine tool for uncertainty evaluation purposes will be incomplete without determining the off-diagonal elements of the covariance matrix. The output of the covariance model is needed to propagate the uncertainty of on-machine measurement through to their post-processing to evaluate part deviations against their required tolerances. Particularly, the covariance analysis is inevitable in uncertainty evaluation of a multi-input measurement function, which is usually the case in on-machine measurement. However, the proposed model also can serve as a stand-alone scheme, providing insights into machine performance.

Therefore, four covariance models were fitted to estimate the covariance between the recorded X and Y coordinates cov(X,Y), between the recorded X and Z coordinates cov(X,Z), between the recorded Y and Z coordinates cov(Y,Z) and between the normal and tangential projections cov(N,T).

When the probe travels in a way that a component of the reported coordinates (for example X coordinate) remains unchanged during the movement, the covariance values between that component and the other two are zero (cov(X,Y)=0 and cov(X,Z)=0). Because the covariance between a constant and a changing variable is zero. Also, by varying the azimuthal angle θ of the probing direction from 0° to 360°, the recorded X coordinates at θ=0° and 180° as well as the recorded Y coordinates at θ=90° and 270° remain constant. That is, at these five angles θ, the covariance between the recorded X and Y coordinates cov(X,Y) is zero. This implies that any polynomial function used to estimate cov(X,Y) should have at least a degree of five.

The R-squared values of the fitted covariance models are 95%, 89%, and 76 %, respectively for cov(X,Y), cov(X,Z) and cov(Y,Z) (Figure 4-13a-c). The models predicted these covariance quantities at the eight validation points with maximum errors 31%, 35%, and 45% (Table 4-4), denoting maximum differences between measured and predicted values of 0.12, 0.07, and 0.07 μm^2, respectively. The quality of fittings is examined with fitting residual histograms and normal probability plots (Figure 4-13d-i). The R-squared values of the models fitted to estimate the covariance between the normal and the tangential projections cov(N,T) is 77% (Figure 4-14a). This model predicts cov(N,T) for the eight validation points with a maximum error of 37% (Table 4-4), denoting a maximum difference magnitude of 0.04 μm^2. Similarly, the normal probability plot (Figure 4-14c) was used to inspect the normality of the residuals (Figure 4-14b).

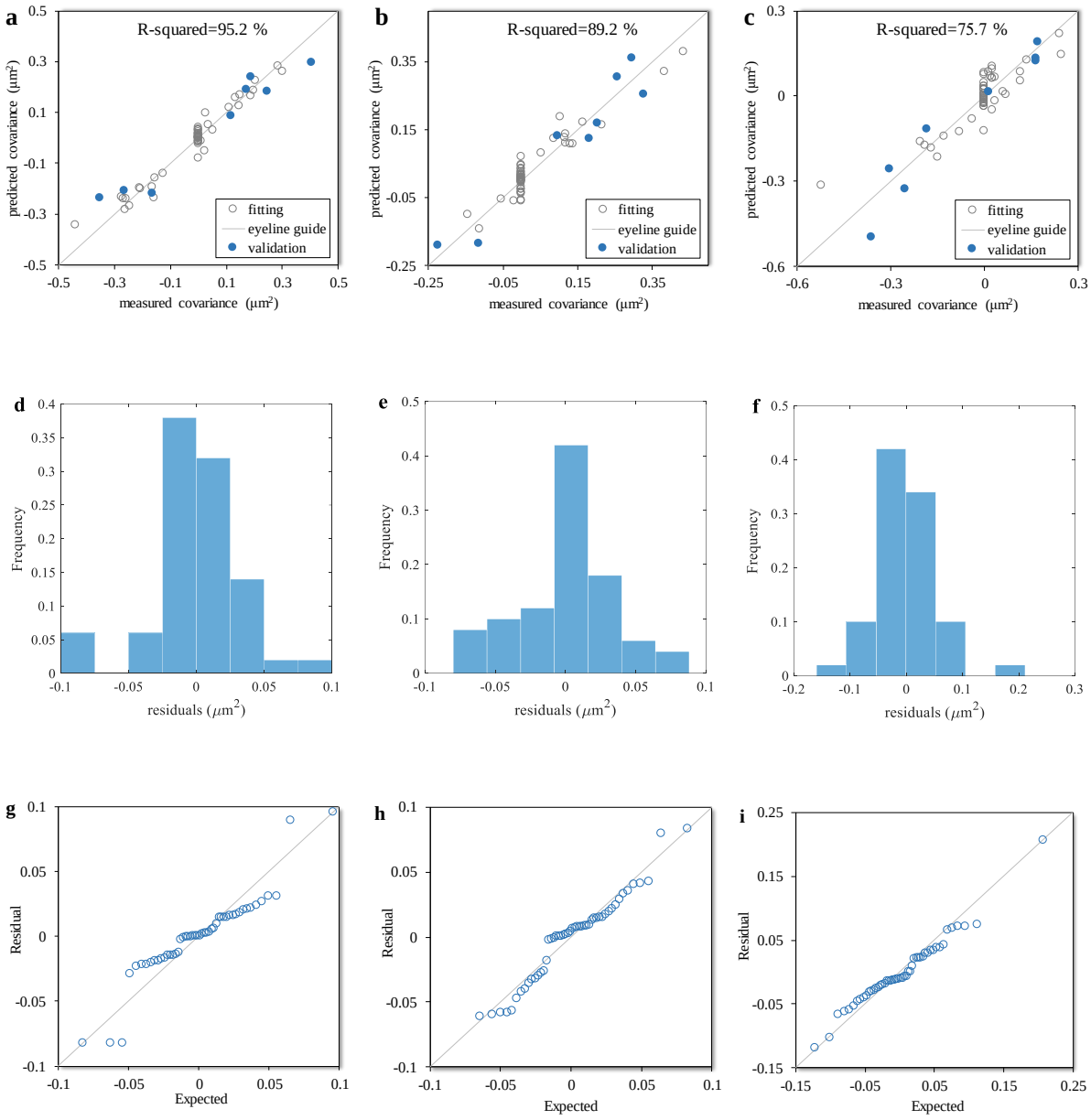

Figure 4-13: Regression plots of the values measured versus the values predicted by the covariance models between: a) the X and Y coordinates cov(X,Y), b) the X and Z coordinates cov(X,Z), and c) the Y and Z coordinates cov(Y,Z). The non-filled and filled markers represent the measurement results used to fit and to validate the covariance models, respectively. The residual histograms obtained by fitting the models to the: d) cov(X,Y), e) cov(X,Z), and f) cov(Y,Z). Normal probability plots obtained for the measured g) cov(X,Y), h) cov(X,Z), and i) cov(Y,Z).

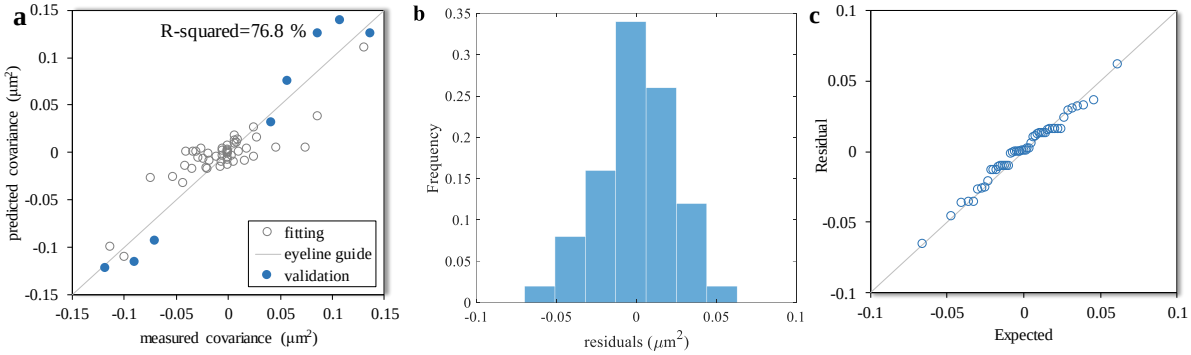

Figure 4-14: a) Regression plot of the values measured versus the values predicted by the covariance model between the values projected perpendicular to the target surface and tangent to the target surface cov(N,T). The non-filled and filled markers represent the measurement results used to fit and to validate the covariance models, respectively. b) The residual histograms obtained by fitting the model and c) corresponding normal probability plot.

Table 4-4: Validation of the covariance models of on-machine measurements.

	Experimental factors							Error (%)			
	φ (degree)	θ (degree)	B_T (degree)	C_T (degree)	X_T (mm)	Y_T (mm)	Z_T (mm)	cov(X,Y)	cov(X,Z)	cov(Y,Z)	cov(N,T)
1	45	180	-90	120	-153.5	-158.3	-89.6	0.3	23.9	14.2	27.4
2	60	240	-60	-180	-36.5	74.5	114.3	25.9	12.6	8.8	17.1
3	60	240	-60	-180	-102.4	-165.5	152.4	20.8	14.1	2.7	12.1
4	0	240	0	0	-80.0	-80.0	90.0	20.6	20.3	10.5	11.8
5	0	240	0	0	-80.0	160.0	166.2	17.7	17.4	18.3	11.4
6	15	240	30	-60	-58.8	27.6	133.8	14.0	16.8	2.3	18.6
7	60	240	60	-120	212.7	-16.2	-71.6	28.9	13.3	3.2	1.2
8	60	-120	75	240	211.6	-16.9	-74.6	8.7	10.6	17.8	17.4

Table 4-5 summarizes the mean and the absolute gradient of the covariance model with respect to the experimental factors (Table 4-1). In this table, similar to Table 4-4, the machine axes are fixed at their central values (Table 4-1) and the approach direction is [φ, θ]=[45°, 45°]. Figure 4-15 depicts the polar plots of the absolute values of the covariance models with respect to the approach vector components, the polar φ and the azimuthal θ angles. As this figure demonstrates, the strongest correlation is observable between the X and Y coordinates for the positive and negative

movements of X and Y-axis, respectively, ($270° < \theta < 360°$) where the covariance reaches 0.9 μm^2. The Y and Z coordinates are the least correlated variables. As expected, the estimator model for cov(X, Y) forms a rose curve due to the zeros of the function at azimuthal angles 0°, 90°, 180°, 270° and 360° (Figure 4-15a). Asymmetric petals suggest that the covariance between the recorded X and Y coordinates is larger for angles θ between 270° and 360°. When the polar angle of the approach vector φ is zero, standing for the probe movement along the Z-axis, cov(X, Y) is zero due to the constant values recorded for X and Y coordinates. However, because of fitting errors the covariance model returns nonzero values for cov(X, Y) at φ=0°. The maximum covariance between the X and Y coordinates belongs to the probe movement with φ=90°, where the recorded Z coordinate is constant. As a result of the unchanged X coordinates recorded at θ=0° and θ=180°, the zeros of the covariance function cov(X, Z) occur at these angles (Figure 4-15b). The covariance values cov(X, Z) are almost symmetric with respect to the machine Y-axis and do not exceed 0.4 μm^2. By moving along the Z-axis, i.e. φ=0°, the constant recorded X coordinates result in the zero of the covariance function cov(X, Z). Having its zero values at θ=90° and θ=270°, the covariance between the Y and the Z recorded coordinates is smaller than 0.2 μm^2.

The behaviour of the model estimating cov(N, T) is mostly steady, except for φ=90° where the model has five zeros by varying azimuthal angle from θ=0° to θ=360°, resembling the behaviour of cov(X, Y). When the approach vector is along any axis of the machine the tangential component of the recorded position is zero, resulting in zero covariance between the normal and the tangential projections. This happens when φ=0°, i.e. approaching along the Z-axis, or when φ=90° and θ takes on one of the values 0°, 90°, 180°, 270° or 360°, denoting the approach vectors along the X or Y-axis. For polar φ angles other than φ=0° and φ=90°, the covariance variations with azimuthal angle θ barely exceed 0.06 μm^2, implying an axisymmetric correlation between normal and tangential projections with respect to the azimuthal angle θ, except for φ=0° and 90°.

Dividing the machine errors into systematic and random components, the later can account for the random positioning of the tool (probe) with respect to the workpiece. Although random, it is suspected that this portion of the machine errors may result from variability sources within the machine structure. These effects propagate through the kinematic chain of the machine and can systematically deviate the end position of the machine branches, resulting in some significant correlations between the coordinates recorded in on-machine probing.

Table 4-5: The average of standard deviation and the average of absolute gradients of the covariance with respect to the experimental factors. For each row the variable other than the indicated factor is fixed so that the machine axes are fixed at their central values (Table 4-1) and the approach direction is [φ, θ]=[45°, 45°].

	Average of absolute covariance (μm^2)				Average of absolute gradient (μm^2/unit)			
	X-Y	X-Z	Y-Z	N-T	X-Y	X-Z	Y-Z	N-T
φ (degree)	0.14	0.18	0.10	0.12	0.0087	0.0095	0.0099	0.0068
θ (degree)	0.21	0.23	0.08	0.19	0.0251	0.0063	0.0019	0.0018
B_T (degree)	0.21	0.31	0.15	0.21	0.0057	0.0054	0.0105	0.0033
C_T (degree)	0.13	0.27	0.04	0.18	0.0026	0.0015	0.0013	0.0014
X_T (mm)	0.17	0.22	0.04	0.13	0.0029	0.0030	0.0026	0.0025
Y_T (mm)	0.11	0.21	0.04	0.16	0.0035	0.0088	0.0051	0.0076
Z_T (mm)	0.08	0.19	0.03	0.15	0.0042	0.0028	0.0047	0.0027

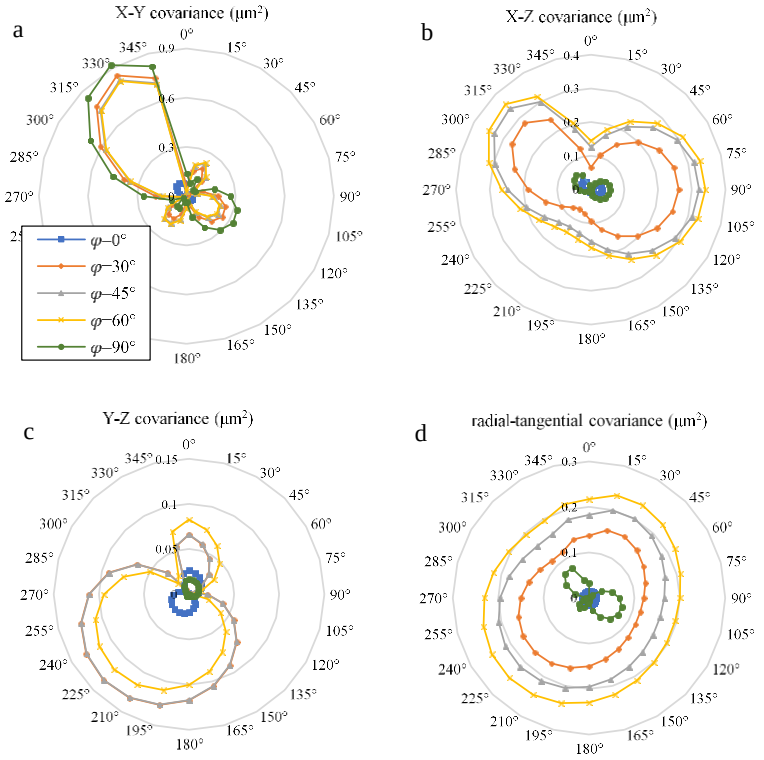

Figure 4-15: The polar plots of the absolute values of covariance predictions from the model versus the polar φ and azimuthal θ angle of the approach direction for the a) cov(X, Y), b) cov(X, Z), c) cov(Y, Z) and, d) cov(N, T). The other independent parameters are fixed at their central values (Table 4-1).

4.7.3 Probing hysteresis test and axis hysteresis test

Figure 4-16a shows the difference between the average of radial projections recorded in the probing hysteresis test (Figure 4-5a). In general, the ring gauge radius measures smaller in the presence of hysteresis. The average of radial projections recorded with hysteresis minus those recorded without hysteresis are plotted in Figure 4-16b. On average, the radius measures 0.11 μm smaller when hysteresis is involved. Figure 4-16c shows the standard deviation obtained in the probing hysteresis test with and without hysteresis effects as well as for the combined data. As this figure shows, hysteresis has no significant effect on the repeatability of probing results. Hysteresis changes the average of probing repeatability by 0.01 μm. To evaluate the uncertainty associated with the systematic hysteresis errors (Figure 4-16b), the law of propagation of uncertainties [42] can be applied. At each indexation, the hysteresis error is calculated by [84]

$$H_\psi = \overline{r_{H,\psi}} - \overline{r_\psi} \tag{4-3}$$

where, $\overline{r_{H,\psi}}$ and $\overline{r_\psi}$ are the average of radial projections measured respectively with and without hysteresis being involved, for indexations $\psi = 0°, 30°, \dots, 330°$. Then, the standard uncertainty of hysteresis error $u(H_\psi)$ can be estimated as

$$u(H_\psi) = \sqrt{u^2\left(\overline{r_{H,\psi}}\right) + u^2\left(\overline{r_\psi}\right)} \tag{4-4}$$

where, $u\left(\overline{r_{H,\psi}}\right)$ and $u(\overline{r_\psi})$ are the standard uncertainties (standard deviations of the mean) of radial projections obtained for each indexation ψ. Evaluating these parameters results in $u(H_\psi)$ values between 0.13 μm and 0.25 μm (Figure 4-16b). By averaging over the 12 values shown in Figure 4-16b, the average hysteresis error is 0.11 μm with a standard uncertainty of 0.19 μm.

Figure 4-17 shows the hysteresis errors, for the axis hysteresis test (Figure 4-5b), calculated as the average of radial projections recorded with the premovements along the positive direction of the cross axis minus those recorded with the negative direction of the cross axis. Comparing the hysteresis errors of axes X and Y (Figure 4-17a) with the probing hysteresis errors obtained for the corresponding indexations $\psi = 0°, 90°, 180°$ and $270°$ (Figure 4-16b) reveals that the hysteresis error of the machine axes is on average 0.22 μm larger than probing hysteresis. Similar to the

probing hysteresis test, on average, the axis hysteresis has negligible effects on the probing repeatability (Figure 4-17b).

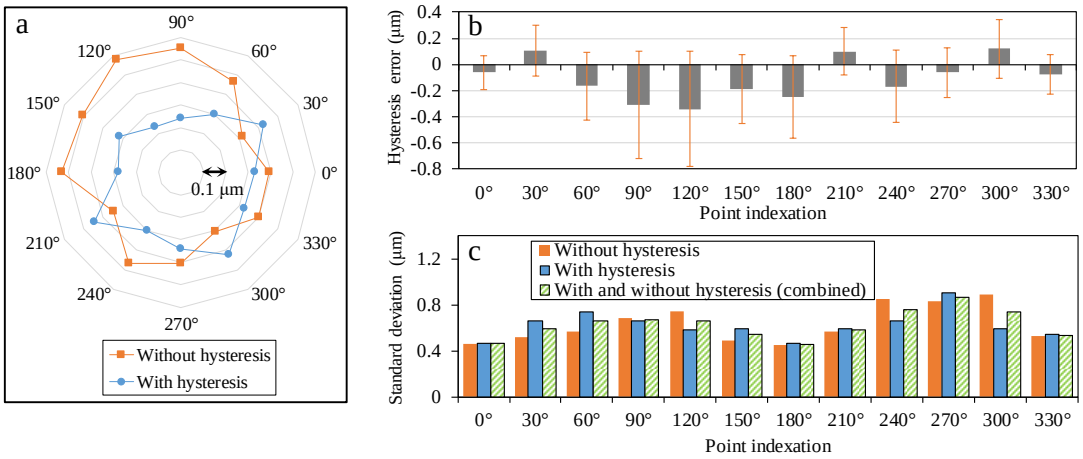

Figure 4-16: a) Polar presentation of the differences between the radii measured for indexations $\psi = 0°, 30°, \ldots, 330°$ (Figure 4-4a), with and without hysteresis being involved; b) hysteresis errors identified for each indexation together with the associated standard uncertainty, and c) the standard deviations of the radial projections recorded for each indexation.

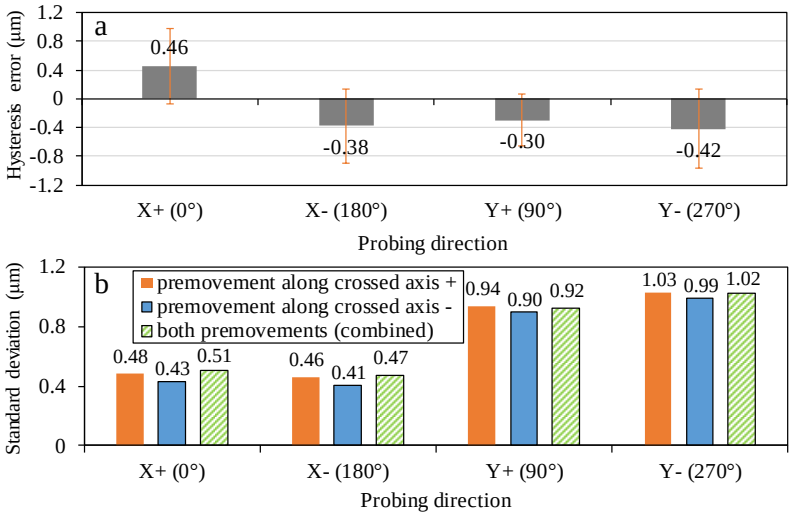

Figure 4-17: a) Hysteresis errors of machine axes X and Y with premovements along the positive and negative directions of the cross axis together with the associated standard uncertainty and b) the standard deviations of probing results with the premovements.

4.7.4 Probing strategy and time span

Figure 4-18 shows the trend of recorded 50 measurements in each of the three ring gauge tests: simple, ordered and shuffled. This figure also includes the temperature variations of the machine work envelop measured during the shuffled and ordered ring gauge tests. In the simple ring gauge test, replicate measurements of each point took about 12 min to complete, suggesting a period short enough to result in stable outputs, from a thermal effects point of view. Therefore, as can be seen in this figure, no systematic behaviour is distinguishable in the recorded values. On the other hand, systematic drifts are observable in the coordinates recorded with the ordered and shuffled strategies. As Figure 4-18 shows, the temperature variations are consistent with the drifts in the recorded coordinates and projections, suggesting that the drifts are most likely to be caused by thermal effects. Each of these tests takes five hours to run, 25 times longer than the simple ring gauge test.

Considering that only the random errors of the measurement system should account for the repeatability of on-machine measurement, random variations should be isolated from the recorded data before any repeatability evaluation. To do so, cubic polynomials are first fitted to the recorded coordinates and the radial projections obtained through the shuffled and ordered tests in order to remove drift, which is associated with thermal effects. Then, fitting residuals are considered to represent the random variations of the recorded data, whose standard deviation specifies probing repeatability. The repeatability values obtained after removing the systematic drifts are shown in Figure 4-19. The average repeatability over the 24 points, obtained by the three tests, is almost 0.65 μm for radial projections. The average repeatability values recorded for the X and Y coordinates with the three ring gauge tests vary by a maximum of 10%, which suggests that the measurement strategy has a negligible effect on probing repeatability.

Because of the long time spans of the shuffled and ordered ring gauge tests, the machine status in terms of thermal variations and performance of inner components, such as bearings, gears and slideway systems, is expected to gradually change during these tests. Besides the observed drifts, these changes might affect the random behaviour of the machine. To study this effect, the steady state of raw data, typically shown in Figure 4-18, is analyzed. As Figure 4-18 shows, after the 25th iteration, the drift is negligible. The probing repeatability along the X ($\psi = 0°, 180°$) and Y ($\psi =$

90°, 270°) axes is calculated within a 10-iteration wide frame. By sliding this frame between the 26th and the 50th iterations, the standard deviations of the data within the frames are shown in Figure 4-20. In this figure, the time span for data acquisition within each frame of the simple test is 2.5 min, where the machine axes and the probe do not perform any other task between two consecutive measurements. This period for the ordered and shuffled tests is almost 24 times larger, i.e. one hour, where the X and Y axes, and the probe conduct different tasks between two consecutive measurements. Then, compared with the simple test, machine conditions are expected to vary more within each frame of the ordered and shuffled tests. As this figure shows, the repeatability obtained by the ordered and shuffled tests is mostly more stable than the simple test, especially for both positive and negative directions of the Y-axis. Moreover, the differences between the probing repeatability along the X and Y axes are smaller in the shuffled and ordered tests compared with the simple test. Conducting this analysis with wider frames verifies these results. These observations imply that warming up the machine and carrying out different/random tasks before conducting an on-machine measurement, as in the shuffled and ordered ring gauge tests, stabilizes the repeatability of axis X and Y.

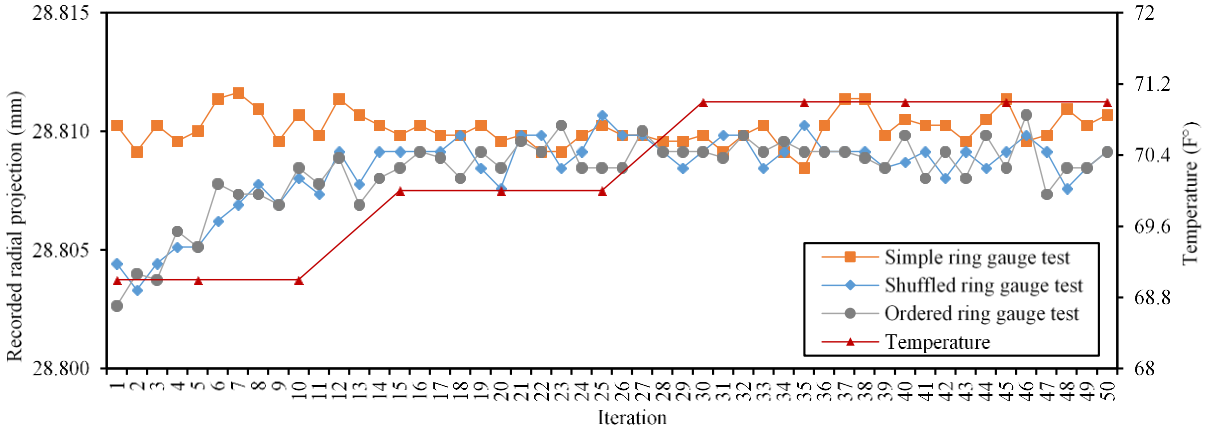

Figure 4-18: Typical trends of replicate measurements done in different ring gauge tests along with temperature variations measured during the shuffled and ordered tests. The presented data is the normal (radial) projections recorded at 90° ($\psi_0 =$ 7.5° in Figure 4-4b).

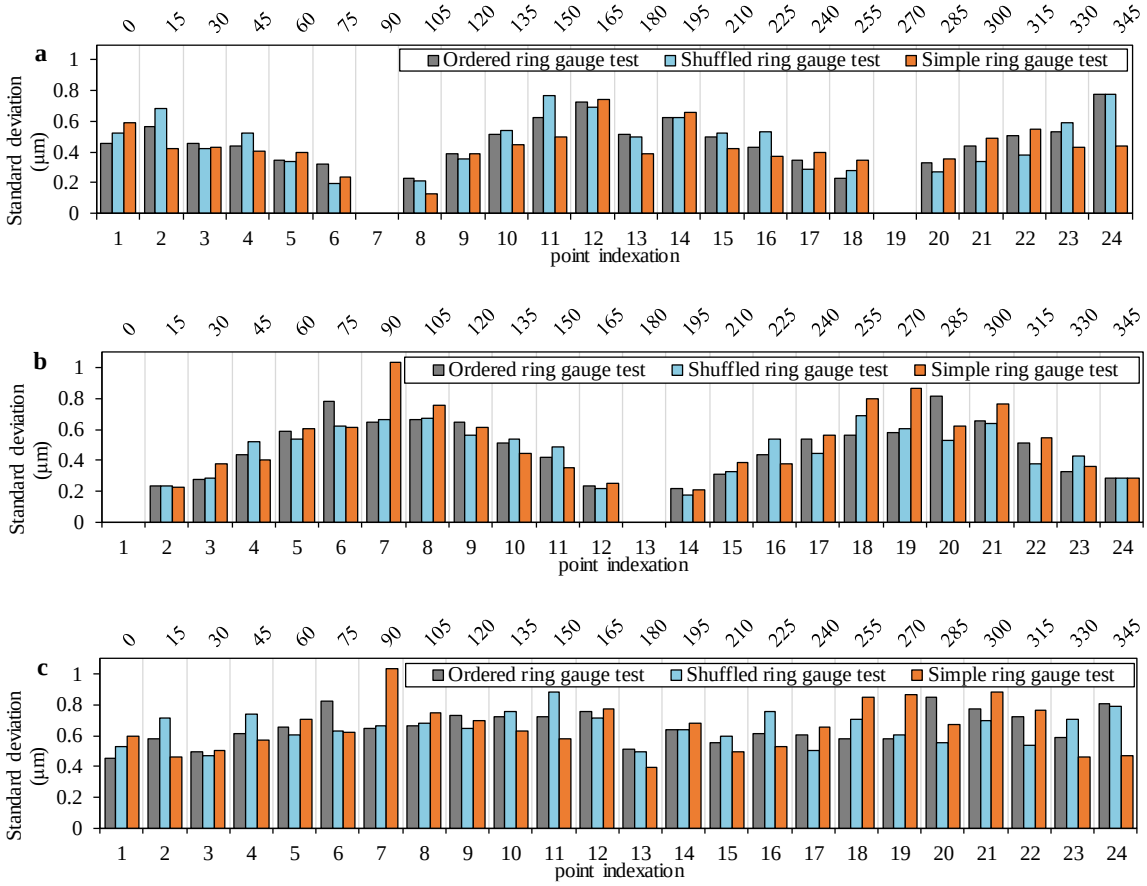

Figure 4-19: The repeatability of on-machine measurements obtained based on the fitting residuals in the ordered and shuffled ring gauge tests for a) the X coordinate, b) the Y coordinate, and c) the normal projection of the Cartesian readings at the 24 points (with $\psi_0 = 7.5°$ in Figure 4-4b). The angle ψ (Figure 4-4b) corresponding to each indexation in Figure 4-4b is shown on top of each graph.

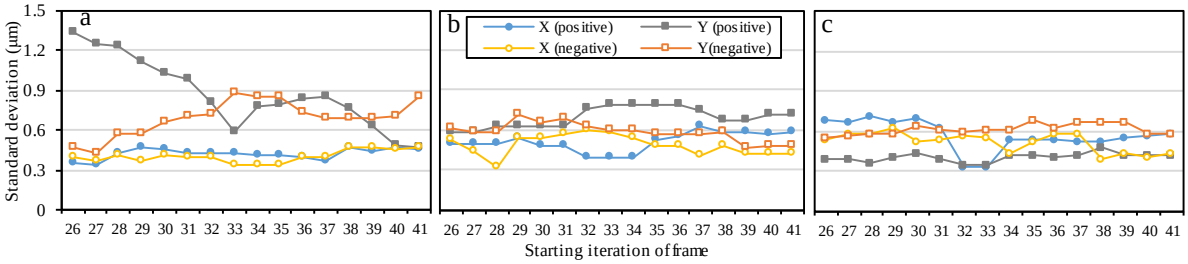

Figure 4-20: The probing repeatability along the X and Y axes by sliding a 10-iteration wide frame between the 26th and the 50th iterations shown in Figure 4-18. Results obtained through the a) simple, b) ordered, and c) shuffled ring gauge tests.

The results of the simple ring gauge test with $\psi_0 = 7.5°$ (Figure 4-4b) reveal the effect of machine resolution in the repeatability of recorded coordinates. According to VIM [3], the resolution is the "smallest change in a quantity being measured that causes a perceptible change in the corresponding indication". Machine resolution transfers continuous measurement results into discrete counterparts. Because of machine resolution, output fluctuations can be either damped or amplified as the measurement outcomes are mapped to different indications. This transformation might affect any estimate of the repeatability of measurement results. The effect of the resolution is visible in Figure 4-21a , which shows the 50 X and Y coordinates recorded for point 67.5° (Figure 4-4b) through replicate measurements in the simple ring gauge test. In the on-machine probing, when a touch occurs, the position of each axis is translated to the closest indication on the axis encoder. As a result, the recorded touch positions in replicate measurements are less likely to lie on the nominal approach path, but on the grids formed by the indications of the machine axes (Figure 4-21a). As can be seen in Figure 4-21a, since the Y-axis motion is dominant the recorded point set is oriented approximately along the nominal measurement direction in a way that the variation range of the Y coordinates is proportionally larger than that of the X coordinates. This

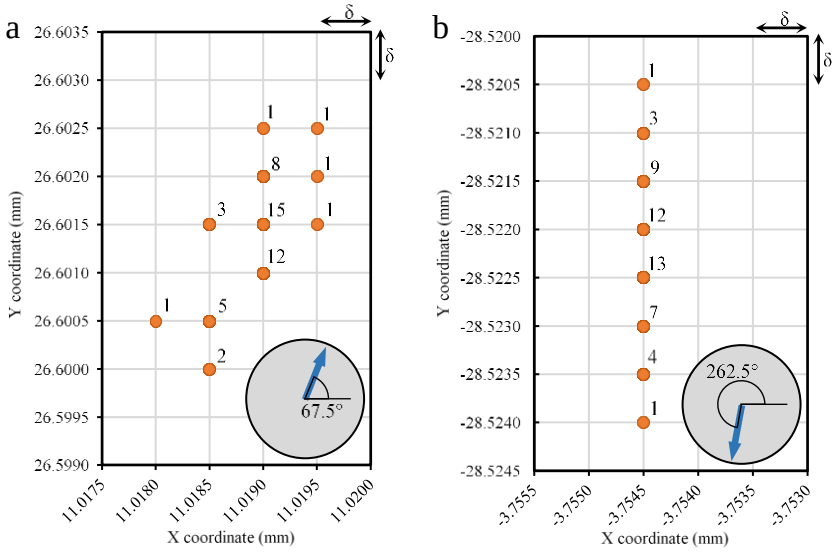

Figure 4-21: 50 replicate measurements recorded in simple ring gauge test with an approach direction lying in the XY plane of the machine frame and making an angle of a) 67.5° and b) 262.5° with the positive direction of the X-axis of the machine (δ=0.5 μm is the machine resolution and the labels indicate the number of duplicate results).

diagram also illustrates how a certain amount of covariance between X and Y occurs when both axes are involved in a probing operation. The effect of machine resolution is even more obvious at target point 262.5°, where all the 50 recorded X coordinates were mapped to the same indication, resulting in perfectly repeatable outcomes with a standard deviation of zero (Figure 4-21b).

4.8 Conclusions

In this study, we quantified the repeatability of a specific instance of a five-axis machine tool in the probing mode by measuring two precision spheres as artifacts and a ring gauge. In order to evaluate measurement repeatability, firstly machine parameters including five quantities of machine pose at the target point X_T, Y_T, and Z_T, B_T and C_T, two direction parameters θ and φ, indicating the approach direction with respect to the target surface, and the probe orientation ω were considered. Preliminary analysis on the effect of probe orientation ω revealed its negligible effect on the measurement repeatability ($\approx$ 0.1 μm). Ignoring this parameter in the design of experiments, 1500 on-machine probing tasks were carried out, including 30 repeated measurements on target points on the spheres at various poses within the workspace of the machine and with different measurement directions. Polynomial models were then fitted to the standard deviations of the recorded X, Y, and Z coordinates as well as to those of the projections of recorded coordinates perpendicular and tangent to the target surface. The covariance quantities were then estimated by fitting quintic polynomials to the measured covariance between the recorded coordinates. The potential effect of measurement system hysteresis on the repeatability of recorded coordinates was also investigated by probing 12 points equally distributed around the inner wall of the ring gauge. The findings are summarized below.

1. Validation of the models suggests that the repeatability of on-machine measurements, quantified by its standard deviation and covariance, can be predicted for any position of the machine and approach direction. The presented method can provide the repeatability models that reliably portray the random behaviour of a machine tool, which is one of the major challenges in conducting traceable on-machine tool measurements. Results show that the standard deviation in on-machine measurement barely exceeds one μm. The recorded X and Y coordinates showed a strong correlation, up to 0.90 μm^2, especially for the positive and negative movements of the X and the Y-axis, respectively. The recorded Y and Z

coordinates were found to be mostly independent with covariance values smaller than 0.15 μm^2. Covariance information is necessary to estimate the uncertainty of geometric and dimensional deviations calculated using the collected coordinates.

2. Hysteresis has a negligible effect on the repeatability of on-machine probing. However, some systematic effects (i.e., biases) were observed. The systematic hysteresis errors caused by the whole probing system, including the machine and the probe, were found to be smaller than those caused by the machine axes. This implies that the measuring system should be entirely considered in hysteresis evaluation because separate hysteresis evaluations of the system components can provide inaccurate error values.
3. The simple ring gauge test shows that the machine resolution plays a significant role in altering the fluctuations of the measurement results so that perfectly repeatable coordinates (zero standard deviation) are recorded for some approach directions with a small angle with the X- or Y-axis. For other directions, a correlation occurs between the coordinates, with the main variability along the probing direction.

4.9 Acknowledgements

This research was supported in part by Natural Sciences and Engineering Research Council of Canada (NSERC) under the CANRIMT Strategic Research Network Grant NETGP 479639-15, and in part by the startup grant of Polytechnique Montreal. The authors gratefully acknowledge Guy Gironne and Vincent Mayer, the technicians of Virtual Machining Research Laboratory (VMRL) at the mechanical engineering department of Polytechnique Montreal.

4.10 Appendix A. Examples of data analysis

4.10.1 Standard deviation and covariance evaluation in the five-axis ball test

Figure A. 1 schematically shows a single probing on the precision sphere in the five-axis ball test. The machine records coordinates X, Y and Z of the probe tip position (vector $\overrightarrow{OP}$ in the machine

frame) over 30 repeated measurements. In order to calculate normal projections N of the recorded coordinates, first, vector $\overrightarrow{\mathrm{CP}}$ can be obtained as

$$\overrightarrow{\mathrm{CP}} = \overrightarrow{\mathrm{OP}} - \overrightarrow{\mathrm{OC}} \qquad \text{A. 4-1}$$

Then, normal projection N is

$$\mathrm{N} = \overrightarrow{\mathrm{CP}} \,.\, \hat{n}\,, \quad \hat{n} = \begin{pmatrix} \sin\varphi \sin\theta \\ \sin\varphi \cos\theta \\ \cos\varphi \end{pmatrix} \qquad \text{A. 4-2}$$

where $\hat{n}$ is the nominal unit vector normal to the ball surface at the target point. For target point$[\varphi, \theta, B_{\mathrm{T}}, C_{\mathrm{T}}, X_{\mathrm{T}}, Y_{\mathrm{T}}, Z_{\mathrm{T}}] = [18°, 144°, 90°, -180°, 78.1\ \mathrm{mm}, 76.8\ \mathrm{mm}, -66.8\ \mathrm{mm}]$ we have $\overrightarrow{\mathrm{OC}} = [76.2000, 80.0000, -78.9190]$ mm. In this example, considering probing results $\overrightarrow{\mathrm{OP}} = [78.9655, 76.1950, -64.4430]$ mm, equation A. 4-2 gives N= 15.2211 mm. Then, tangential projection T of the recorded coordinates is

$$\mathrm{T} = \sqrt{\left\|\overrightarrow{\mathrm{CP}}\right\|^2 - \mathrm{N}^2} \qquad \text{A. 4-3}$$

which yields T =0.0009 mm. These calculations are conducted on the 30 measurements repeated

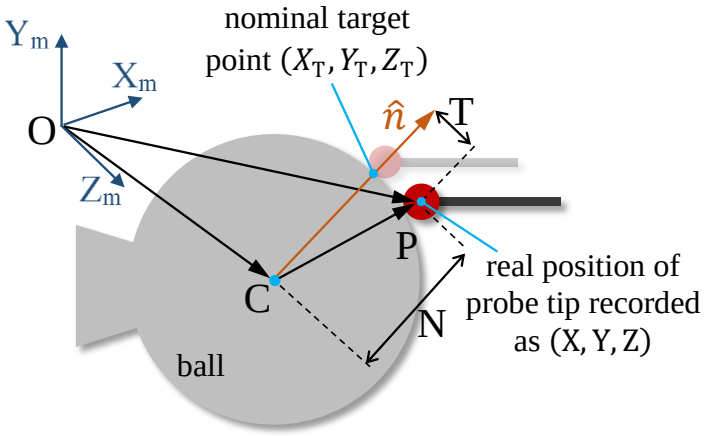

Figure A. 1: Schematic of a single probing on the precision sphere in the five-axis ball test.

for each of the 50 target points. The 50 standard deviations obtained for each of the coordinates and projections form a data set are used to fit the standard deviation model given by Eq. 4-1. The covariance values are also calculated between the recorded coordinates and the projections in order to fit the covariance model given by Eq. 4-2.

4.10.2 Hysteresis evaluation

In the probing hysteresis test conducted for $\psi = 60°$ (Figure 4-4a), coordinates X and Y are directly recorded by the machine. Radial projections R are obtained by

$$\mathrm{R} = \begin{pmatrix} \mathrm{X} \\ \mathrm{Y} \end{pmatrix} . \hat{N} , \quad \hat{N} = \begin{pmatrix} \cos\psi \\ \sin\psi \end{pmatrix} \qquad \text{A. 4-4}$$

where $\hat{N}$ is the nominal unit vector along the approach direction. Averaging over the 24 radial projections calculated for $\psi = 60°$ gives $\overline{r_{H,\psi}}$ =28.7821 mm and $\overline{r_{\psi}}$=28.7819 mm, respectively with and without hysteresis being involved. Then, Eq. 4-3 gives a hysteresis error of $H_{60°} = -0.17$ µm.

In the axis hysteresis test concerning the positive direction of the X-axis, the X-axis hysteresis error is 0.46 µm, which is calculated as the average of readings recorded with the premovements along the positive direction of the Y-axis (28.7623 mm) minus those recorded with the negative direction of the Y-axis (28.7618 mm).

4.10.3 Evaluation of probing strategy and time span effects

Using Eq. A. 4-4), the radial projections measured by means of the three ring gauge tests (i.e., simple, ordered and shuffled tests), conducted for $\psi = 30°$ (Figure 4-4b with $\psi_0 = 0°$), are shown in Figure A. 2a. This figure also includes the cubic polynomials along with their equations, fitted to the readings of the ordered and the shuffled ring gauge tests. By removing the drift in this example, the standard deviations recorded in the ordered test decreased from 2.07, 1.12 and 2.34 µm to 0.45, 0.28 and 0.49 µm, respectively for the coordinates X and Y, and the radial projections.

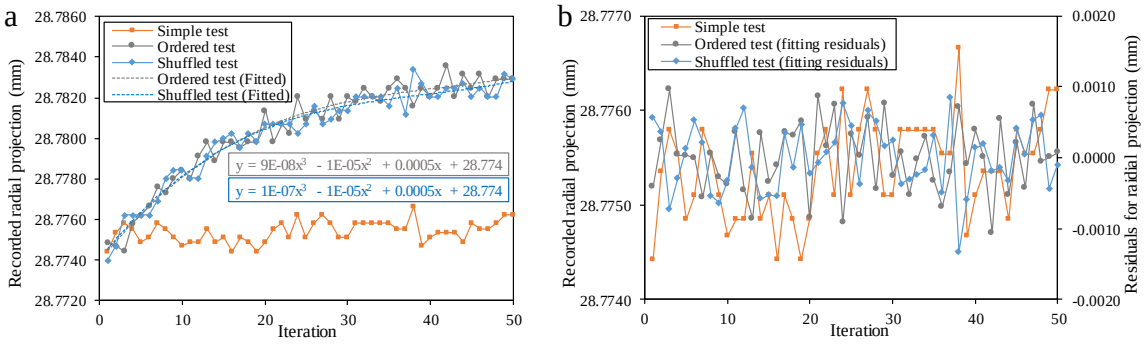

Figure A. 2: a) The radial projections measured by the simple, ordered and shuffled ring gauge tests, conducted for $\psi = 30°$ (Figure 4-4b with $\psi_0 = 0°$), and b) the corresponding fitting residuals obtained for the ordered and shuffled tests together with the raw data recorded by the simple test.

CHAPTER 5 : ARTICLE 2: EFFICIENT UNCERTAINTY ESTIMATION OF INDIRECTLY MEASURED GEOMETRIC ERRORS OF FIVE-AXIS MACHINE TOOLS VIA MONTE-CARLO VALIDATED GUM FRAMEWORK

Published in: Precision Engineering, October 2020

Authors: Saeid Sepahi-Boroujeni[*a]; J.R.R. Mayer[a]; Farbod Khameneifar[a]

5.1 Abstract

Whether using a machine tool as a machining or a measuring system, its accuracy has a key role in ensuring product quality. As a result, conducting periodic geometric calibration of a machine tool to quantify and to compensate for the machine's geometric errors is highly desirable. The measured geometric errors must be accompanied by uncertainty estimates, reflecting the lack of exact knowledge of the value of measurands. Indirect calibration approaches, as opposed to direct ones, have gained considerable attention recently because they can be automated and take considerably less time to conduct. However, the uncertainty of the indirectly measured error parameters is more challenging to estimate because of the complexity of the used mathematical models and the large number of machine error parameters identified simultaneously. The use of uncalibrated artifacts also adds to the wariness towards such approaches. In this paper, two different approaches are used to evaluate the uncertainty of machine geometric errors identified by the scale and master ball artifact (SAMBA), an indirect approach relying on the on-machine probing of uncalibrated and calibrated artifacts. First, a simulator of an adaptive Monte Carlo method (MCM) determines the uncertainty of machine tool geometric errors. A multivariate sample generator draws at random the input vectors from a joint probability density function (PDF) obtained through experimental replications over 15 days. Supplement 2 to the Guide to the expression of uncertainty in measurement (GUM) specifies the conditions where an adaptive MCM validates the GUM uncertainty framework (GUF). Adhering to the instructions given by this standard, the validity of

---

[*] Corresponding author
[a] Department of Mechanical Engineering, Polytechnique Montreal, Montreal, QC H3T 1J4, Canada

GUF, a much faster uncertainty evaluation method, is examined. Results show that the adaptive MCM procedure, which takes 24 h to run, validates the alternative GUF approach, which takes a computation time of only 10 min. A maximum disagreement of 1% between the geometric errors from experimental replications and their estimates identified by the adaptive MCM implies that the marginal means of the estimated output joint PDF in the adaptive MCM well represent the average of the output quantities. High dependencies of the linear terms (slopes) of the linear positioning errors of prismatic axes X, Y, and Z on the SAMBA scale bar length cause high correlations between these errors with correlation coefficients up to 0.965. The largest standard uncertainty estimated for the angular geometric errors is 1.26 μrad (associated with the out-of-squareness error of axis Z relative to axis X, E_{B0Z}) and that for the translational geometric errors is 1.03 μm (associated with the distance between the spindle axis and axis B along axis X, E_{X0S}). Axis X is estimated to have the largest standard uncertainty (6.1 μm/m) of the linear terms (slopes) of the linear positioning errors among the machine's prismatic joints.

Keywords: Uncertainty; Monte Carlo; GUM framework; Machine tool; Calibration; SAMBA

5.2 Introduction

Machining accurate parts requires machine tools characterized by high repeatability and accuracy [91]. In closed-loop manufacturing, part metrology (through in-process inspection or off-line measurements) can provide feedback to apply adjustments to the process parameters to attain the required accuracy [15]. Geometric accuracy of the part can also be achieved through machine calibration, including error compensation or mechanical adjustments, before machinery may come into operation [92]. Calibration becomes more important when production conditions such as manufacturing time and volume prevent any closed-loop optimization of process parameters [91].

Machine tools have structural loops built of linear and rotary axes, having a tool at one end and a workpiece at the other end of their kinematic chain. Due to geometric errors of the machine tools, the actual end position and orientation of the tool with respect to the workpiece differ from their nominal values. Geometric errors describe the imperfect position and orientation of a mechanical axis relative to other mechanical axes of the machine as well as the imperfect motions of each machine axis [91].

Measurement methodologies of geometric errors comprise direct and indirect measurement methods. In case of direct method, the measurand is a single geometric error, such as linear or angular error motions of a single axis [91]. Measuring the angular error motion of a rotary axis or linear positioning error of a linear axis are examples of direct methods [93]. When conducting direct measurements, it is necessary to install the setup in a way that only the targeted error affects the measurement results [22]. On the other hand, indirect measurements focus on the superposition of geometric errors, i.e. volumetric error, the relative deviations between actual and nominal position and orientation of the tool frame with respect to the workpiece frame. The ball bar is one of the most established instruments for indirect measurement of machine geometric errors, described in ISO 230-4:2005 [94]. In a circular trajectory, geometric errors of at least two axes of the machine tool result in variations of the ball bar length from its nominal value. Then, best fitting the machine kinematic error model to the ball bar readings can identify many geometric errors. Indirect measurement methods mostly benefit from simpler setups and faster measurement processes compared to direct methods [22].

Regardless of choosing a direct or an indirect method to quantify the geometric errors of a machine tool, measurement results are subject to measurement uncertainty. The Guide to the Expression of Uncertainty in Measurement (GUM) [42] defines an internationally accepted procedure for measurement uncertainty evaluation. GUM mainly focuses on the law of propagation of uncertainties as a tool to propagate the uncertainties of the input variables of a measurement function to evaluate the uncertainty of measurement results. This law, however, is limited to multi-input single-output measurement models and does not provide any probability density function (PDF) for the measurement output quantity. Supplement 1 to the GUM [79] provides details of the implementation of a Monte Carlo method (MCM), by which the PDF and many other statistical measures of the output quantity become achievable for multi-input multi-output measurement functions. Supplement 2 to the GUM [50] presents a modification of the GUM uncertainty framework (GUF) that gives the estimates of the output quantities and their covariance matrix of a multi-input multi-output function when the input quantities are summarized (as in GUM) in terms of estimates and their covariance matrix. In addition, Supplement 2 to the GUM specifies the validation steps of GUF using an MCM.

In general, indirect methods employed for a multi-axis machine tool calibration identify the geometric errors through a multi-output measurement function. As a result, the law of propagation of uncertainties specified by GUM is unable to evaluate the uncertainty of estimated geometric errors. Besides, in case of compensation for the effects of the geometric errors of a machine tool used as a measuring device, the uncertainties of the geometric errors must be further propagated through the employed compensation model to evaluate the uncertainty of the corrected probing results. This requires, besides the uncertainties of the estimated geometric errors, the correlation between these estimates, which is not attainable via the methodology specified in GUM [42]. Consequently, one has to evaluate the uncertainty of geometric errors by means of an appropriate method such as MCM or the validated GUF, respectively elaborated in Supplements 1 [79] and 2 [50] to the GUM.

In machine tool metrology, MCM can address the uncertainty associated with geometric errors obtained in the calibration process of machine tools. Bringmann and Knapp [60] estimate the uncertainty associated with the calibration technique “chase-the-ball” using an MCM, where machine errors are drawn at random from uniform distributions. They define the ranges of these errors according to comparative measurements, manufacturer specifications or the values stated in standards. In another study [61], they adopt the same approach to estimate the uncertainty of machine parameters obtained by another calibration procedure, “3-D ball plate”. They model machine parameters as a superposition of a linear term (e.g., the thermal expansion of a ball screw), of a cyclic term with a wavelength representing either the grating of the linear scale or the pitch of the ball screw, plus a certain number of Fourier harmonics. The parameters of such a series are random draws from uniform PDFs. Andolfatto et al. [62] use the non-contact measuring instrument “CapBall” to identify machine axis position and orientation errors and then implement an MCM to estimate the uncertainty associated with the estimated errors. They evaluate the uncertainties of eight axis position and orientation errors and six setup errors by considering the effects of CapBall sensors, transformation matrices, and the drift of the kinematic chain. They show that involving the drift effects in uncertainty evaluations results in less normality in the measurand distribution because the MCM trials do not occur under identical conditions. Los and Mayer [63] implement an adaptive MCM to evaluate the uncertainty associated with eight axis position and orientation errors and three error motions of a machine tool, identified by using the scale and master ball

artifact (SAMBA) technique. The inputs of their measurement model are the coordinates probed on SAMBA using a touch-trigger probe. Replicate measurements over a period of 24 h determine the joint PDF of input values, while the machine is cold or is cooling down from 27°C to 23°C. They report smaller rectangular coverage intervals without the warm-up cycle, though these intervals do not well represent real conditions of the machine performance. They also observe a large growth in the output correlation matrix due to the drifts in ball coordinates probably caused by thermal variations in the machine tool. Zimmermann and Ibaraki [95] adopt a new calibration procedure based on on-machine measurement of an uncalibrated artifact to identify the position errors and the error motion of a rotary axis of a machine tool. They use an MCM simulator to estimate the standard uncertainty propagated through the multi-input multi-output calibration model. Measuring the repeatability of the probing system smaller than the machine resolution, they assign a density function with a standard deviation equal to the machine resolution to the input quantities, i.e. the on-machine probing results. MCM is also an effective tool in the uncertainty evaluation of coordinate measuring machines (CMMs) [58, 96-99]. Balsamo et al. [53] introduce "expert CMM" aiming to evaluate the uncertainty associated with CMM probing, where an error simulator adds imperfections to random samples and repeatedly generates distorted shapes of a part. Then, statistical analysis of the population obtained for these shapes gives the uncertainty associated with the measurement results. They validate the evaluated uncertainty by measuring repeatedly a calibrated hole plate at 100 different positions of the CMM working volume. The uncertainty associated with 93 measurements out of 100 lies within the expanded uncertainty interval for a coverage probability of 95%. Sladek and Gaska [56] use a LaserTracer™, a commercial product, to indicate volumetric errors and the repeatability of a CMM. Defining a 3D Cartesian grid in the working volume of the machine, they assign a PDF to each point through replicate measurements. They separately investigate the contribution of the employed probe head to CMM probing accuracy by measuring a precision sphere under different probing strategies. They conclude that, in case of systematic error compensation, studying the effects of random errors can address the accuracy of the CMM i.e. the closeness between a measured value and true value of the measurand.

In this study, we investigate the uncertainty associated with the machine geometric errors quantified by the multi-input multi-output calibration model of SAMBA. In order to involve only

the random effects, the measurement process excludes any warm-up cycle or noticeable thermal variation of the machine tool. Then, an adaptive MCM simulator receives the summary of the initial measurements (indications of the center positions of the balls of the artifact), in terms of estimates and an associated covariance matrix, and returns the estimates of the machine errors and the associated uncertainties. Then, through a linear approximation of the SAMBA calibration function, GUF evaluates the estimates and the uncertainties of the machine errors. Comparing the outcomes of the two approaches, we examine the feasibility of replacing the elaborate MCM with the efficient but approximate GUF.

5.3 Geometric error evaluation

The SAMBA artifact consists of any number of precision balls fixed on rods with different lengths along with a calibrated scale bar made of a fixed length magnetic double ball bar (Figure a). In this study, four balls are used. The position of the balls amongst themselves and relative to the machine table are uncalibrated and the scale bar is the only calibrated part of the artifact. The bar sits directly on the machine pallet and it is assumed that the relative positions of the four balls with respect to the last kinematic axis of the workpiece branch remain unchanged during the calibration process (Figure b). The experimental stage of the calibration process consists of probing each precision ball, in order to determine its centre coordinates, in different angular positions of the machine rotary axes and measuring the length of the scale bar at least once.

As an indirect method, the SAMBA technique identifies geometric errors based on the evaluation of volumetric error vectors or residuals $\boldsymbol{r}$ at the ball centres [25, 26]. This requires an error-enriched kinematic model of the machine, which allows calculating the predicted tool position $\boldsymbol{P}_{\text{tool}}$ relative to the probed ball centre $\boldsymbol{P}_{\text{ball}}$. The kinematic model of the machine gives this predicted relative position based on the axis positions and through a chain of transformation matrices corresponding to the machine topology and its geometric errors (Figure b). Then, residuals $\boldsymbol{r}$ are

$$\boldsymbol{r} = (\boldsymbol{P}_{\text{tool}} - \boldsymbol{P}_{\text{ball}})_{\text{predicted}} - (\boldsymbol{P}_{\text{tool}} - \boldsymbol{P}_{\text{ball}})_{\text{actual}} \qquad 5\text{-}1$$

where, $\boldsymbol{P}_{\text{tool}}$ and $\boldsymbol{P}_{\text{ball}}$ are column vectors including the coordinates of the tool and the ball positions, respectively, and $\boldsymbol{r}$ is a column vector of the corresponding residuals. The actual relative

position equals the zero vector when the tool (stylus tip centre) coincides with the centre of the probed ball. This being physically impossible, the tool coordinates are approximated by probing five points on the ball surface. In other words, when probing a ball, it is assumed that the recorded machine axis positions, as estimated from the five points probed on the ball surface, would be those positioning the tool (stylus tip center) at the ball centre, so that

$$(\boldsymbol{P}_{\text{tool}} - \boldsymbol{P}_{\text{ball}})_{\text{actual}} = \vec{\boldsymbol{0}} \qquad 5\text{-}2$$

Substituting Eq. 5-2 into Eq. 5-1 yields

$$\boldsymbol{r} = (\boldsymbol{P}_{\text{tool}} - \boldsymbol{P}_{\text{ball}})_{\text{predicted}} \qquad 5\text{-}3$$

Figure 5-1a illustrates the flowchart of the SAMBA geometric error estimation process. For each ball centre, mapping the probe tip centre from the tool frame to the ball frame by means of homogeneous transformation matrix ${}^{\text{ball}}\boldsymbol{T}_{\text{tool}}$ gives the corresponding residual [63]. This matrix is obtained by multiplying homogenous transformation matrices between successive error-enriched link and axis frames from each ball to the stylus tip [100]. Eq. 5-3 implies that the smaller the residuals, the more accurate is the machine kinematic model (${}^{\text{ball}}\boldsymbol{T}_{\text{tool}}$). In other words, the more accurate are the geometric errors in the kinematic model of a machine tool, the more accurate is the predicted relative position of the tool with respect to the workpiece. Then, a calibration model can identify the geometric errors by developing the machine kinematic model in such a way that minimizes the sum of the squares of residuals $\boldsymbol{r}$. SAMBA incorporates the Gauss-Newton method [101] to estimate the required changes (adjustments) $\boldsymbol{\delta y}$ in $\boldsymbol{y}$, a column matrix of machine geometric errors and artifact dimensions. By defining $\boldsymbol{J}$ the sensitivity Jacobian matrix of residuals $\boldsymbol{r}$ with respect to $\boldsymbol{\delta y}$, the residuals are

$$\boldsymbol{r} = \boldsymbol{J}\,\boldsymbol{\delta y} \qquad 5\text{-}4$$

Solving this equation for $\boldsymbol{\delta y}$ gives

$$\boldsymbol{\delta y} = \boldsymbol{J}^{+}\boldsymbol{r} \qquad 5\text{-}5$$

where $\boldsymbol{J}^{+}$ is the pseudoinverse matrix of $\boldsymbol{J}$, defined by

$$\boldsymbol{J}^{+} = (\boldsymbol{J}^{\mathrm{T}}\boldsymbol{J})^{-\mathbf{1}}\,\boldsymbol{J}^{\mathrm{T}} \qquad 5\text{-}6$$

The minimization of the sum of the squares of residuals $\boldsymbol{r}$ starts with an initial guess for $\boldsymbol{y}$. The initial guess for the machine geometric errors is $\mathbf{0}$ (the perfect or nominal machine) and the initial guess for the uncalibrated dimensions $\boldsymbol{d}$ (the balls' centre coordinates in the last axis frame of the workpiece branch) is the mean predicted tool position for each ball calculated using a nominal machine model, i.e. $\boldsymbol{y}^{0} = [\mathbf{0}, \boldsymbol{d}]^{\mathrm{T}}$. Although the ball positions are uncalibrated and dimensions $\boldsymbol{d}$ are only roughly known at first, including them together with the machine geometric errors as unknown variables in $\boldsymbol{y}$ allows for explaining as much as possible of the residuals by also changing the estimated coordinates of the balls in the last workpiece branch frame. In the n^{th} iteration ($n > 0$), after extracting the corresponding residual vector $\boldsymbol{r}^{n}$ from homogeneous transformation matrix ${}^{\mathrm{ball}}\boldsymbol{T}_{\mathrm{tool}}$, adjustments $\boldsymbol{\delta y}^{n}$ (Eq. 5-5) update $\boldsymbol{y}^{n-1}$ as $\boldsymbol{y}^{n} = \boldsymbol{y}^{n-1} + \boldsymbol{\delta y}^{n}$. The process stops when $|\boldsymbol{\delta y}^{n}|$ becomes smaller than stipulated threshold $\boldsymbol{\tau}$.

In this study, SAMBA evaluates the geometric errors of a five-axis horizontal machining centre model HU40-T from Mitsui Seiki equipped with a Renishaw® MP 700 touch-trigger probe (Figure 5-1). The employed SAMBA consists of four precision balls of diameter 12.7 mm and a scale bar with a calibrated length of 305.2105 mm. The geometric error measurement procedure is replicated over 15 days, once a day at a specific hour and without any preceding warm-up cycle. Each test of these experimental replications of the SAMBA procedure completes over a time span of almost 3 h, including the probing of 109 ball centres. Table 5-1 lists the machine geometric errors identified by SAMBA as measurand. In this table, the error symbols are according to the nomenclature specified in [102].

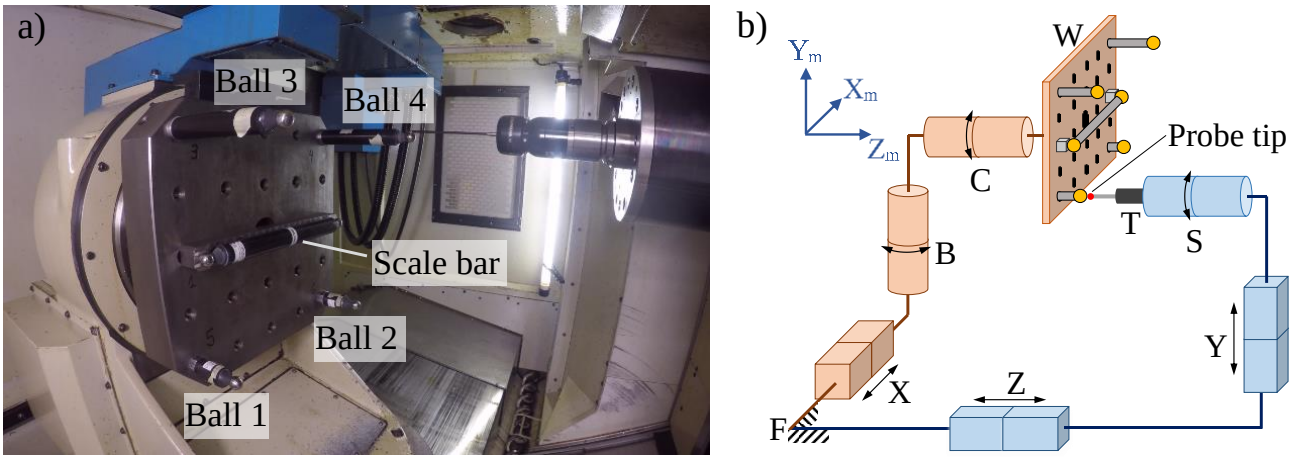

Figure 5-1: a) Experimental setup of SAMBA on a Mitsui Seiki HU40-T machine tool equipped with a Renishaw® MP 700 touch-trigger probe. b) Schematic of the five-axis machine tool with topology WCBXFZYST (W: workpiece; C and B: rotary axes around axes Z and Y, respectively; X, Y, and Z: machine linear axes; F: foundation; S: spindle, and T: tool).

Table 5-1: Geometric errors of the machine tool according to the nomenclature specified in [102]. The first subscript is the nature of the error, the numeral 0 (zero) as the middle subscript indicates that it is an axis position or an orientation error (not an error motion) and the third subscript is the axis of motion with this error.

Symbol	**Description**	**Number of significant figures as per validated uncertainty**
E_{A0B} (μrad)	out-of-squareness error of axis B relative to axis Z	2
E_{C0B} (μrad)	out-of-squareness error of axis B relative to axis X	2
E_{X0C} (μm)	distance between axes B and C	4
E_{A0C} (μrad)	out-of-squareness error of axis C relative to axis B	3
E_{B0C} (μrad)	out-of-squareness error of axis C relative to axis X	2
E_{B0Z} (μrad)	out-of-squareness error of axis Z relative to axis X	3
E_{A0Y} (μrad)	out-of-squareness error of axis Y relative to axis Z	3
E_{C0Y} (μrad)	out-of-squareness error of axis Y relative to axis X	3
E_{XX1} (μm/m)	linear term (slope) of the linear positioning error of axis X	2
E_{YY1} (μm/m)	linear term (slope) of the linear positioning error of axis Y	3
E_{ZZ1} (μm/m)	linear term (slope) of the linear positioning error of axis Z	3
E_{Y0S} (μm)	distance between the spindle axis and axis C along axis Y	3
E_{X0S} (μm)	distance between the spindle axis and axis B along axis X	4

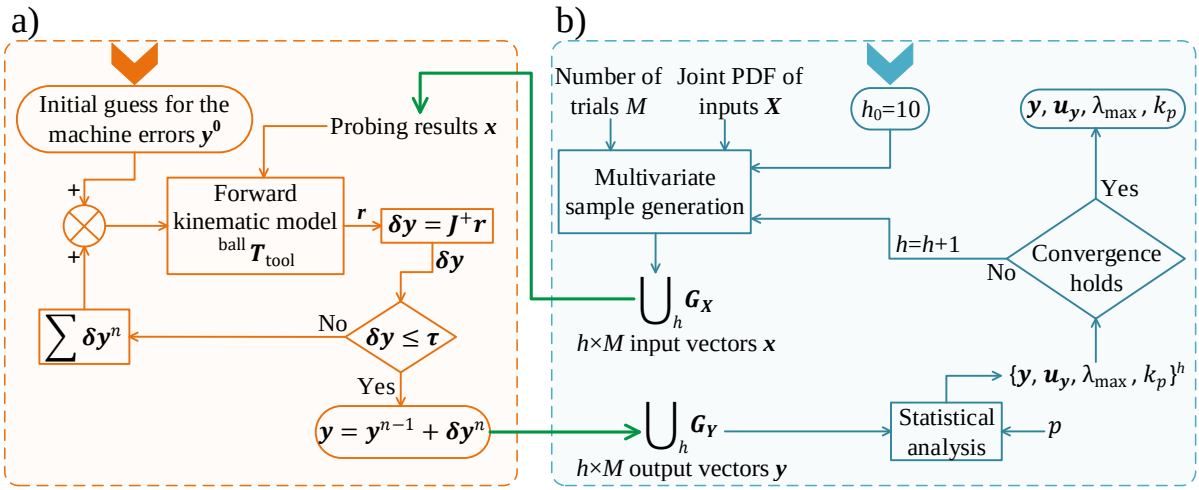

Figure 5-2: Flowcharts of a) SAMBA calibration process and b) uncertainty evaluation by means of the adaptive Monte Carlo.

5.4 Uncertainty estimation

Any statement of the results of a measurement process is complete only when accompanied by the measurement uncertainty. The GUM uncertainty framework (GUF) [50] mainly includes a linearized model that efficiently estimates an expanded uncertainty by assuming a normal PDF for the output quantities. Based on the central limit theorem, however, assuming a normal PDF for the output quantities can be imprecise when a *t*-distribution describes an input quantity with a type A evaluation with a small number of replicate indications [48]. This might happen in industrial metrology, for example, by assigning a uniform (rectangular) PDF to a calibrated length. Therefore, employing the linear uncertainty evaluation using GUF [50] requires a careful inspection of input variables. Although costly in terms of computing time, MCM is a reliable mathematical algorithm for determining the joint PDF of the output values, by which one can validate the legitimacy of GUF.

5.5 Adaptive Monte Carlo method

In an MCM, the evaluation of an input population with measurement model $f(\boldsymbol{X})$ generates a population of output quantities (Figure b). A multivariate sample generator serves as an engine in any MCM simulator, which uses the joint PDF assigned to input quantities $\boldsymbol{X}$ to create input

estimate $\boldsymbol{x}$. Each draw of input quantities corresponds to one and only one set of measurand values, $\boldsymbol{y}$, through the measurement model. Then, repeating this process, say M times (trials), results in the same number of output quantity sets. For a univariate random variable, mapping a random number within interval $[0,1]$ through the inverse of the cumulative distribution function (CDF) of the input random variable can generate a random sample. However, drawing a multivariate random sample from a joint PDF is more complicated. Supplement 1 to the GUM [79] proposes the following equation to draw M random vectors from an N −dimensional multivariate normal distribution:

$$\boldsymbol{G_X} = \boldsymbol{x}\,\boldsymbol{1_{M\times 1}}^{\mathrm{T}} + \boldsymbol{L}^{\mathrm{T}}\,\boldsymbol{Z} \tag{5-7}$$

where, $\boldsymbol{G_X}$ is an $N \times M$ matrix, of which the j^{th} column is a random draw from the multivariate normal distribution, and $\boldsymbol{x}$, of dimension $N \times 1$, is the vector of input quantity estimates. $\boldsymbol{1}_{M\times 1}$ is a column vector of ones of length M and $\boldsymbol{Z}$, of dimension $N \times M$, is a set of draws from a standard normal distribution. In this equation, $\boldsymbol{L}$ of dimension $N \times N$ is the Cholesky factor (a lower triangular matrix) of covariance matrix $\boldsymbol{U_x}$ that satisfies

$$\boldsymbol{U_x} = \boldsymbol{L}\,\boldsymbol{L}^{\mathrm{T}} \tag{5-8}$$

Then, the M vectors included in $\boldsymbol{G_X}$ correlate as per the covariance matrix $\boldsymbol{U_x}$ of the input data. In the evaluation of random input vectors $\boldsymbol{x}$ over M trials of MCM, matrix $\boldsymbol{G_Y}$ of dimension $m \times M$ stores the output vectors, where m is the number of output quantities. Matrices $\boldsymbol{G_X}$ and $\boldsymbol{G_Y}$ are the discrete presentations of input and output parameters so that the i^{th} row of $\boldsymbol{G_X}$ and the j^{th} row of $\boldsymbol{G_Y}$ provide the discrete representations of marginal distributions for random variables X_i and Y_j, respectively [52, 79]. Taking the average of each row of $\boldsymbol{G_Y}$ provides $\boldsymbol{y}$, a best estimate of $\boldsymbol{Y}$:

$$\boldsymbol{y} = \frac{1}{M}\boldsymbol{G_Y}\,\boldsymbol{1}_{M\times 1} \tag{5-9}$$

The covariance matrix associated with the best estimate $\boldsymbol{y}$ is

$$\boldsymbol{U_y} = \frac{1}{M-1}\boldsymbol{G'_Y}\,(\boldsymbol{G'_Y})^{\mathrm{T}}, \qquad \boldsymbol{G'_Y} = \boldsymbol{G_Y} - \boldsymbol{y}(\boldsymbol{1}_{M\times 1})^{\mathrm{T}} \tag{5-10}$$

The square root of the i^{th} diagonal element of $\boldsymbol{U_y}$ is the standard uncertainty associated with the estimate of the i^{th} output quantity y_i. The off-diagonal value located on the i^{th} row and the j^{th} column of $\boldsymbol{U_y}$ represents the covariance between the corresponding output estimates.

For a given coverage probability p, a coverage interval $[y_{\text{low}}, y_{\text{high}}]$ of single output variable Y_i is an interval comprising pM estimates y_i of the output population. This interval is obtainable by sorting the values in the i^{th} row of $\boldsymbol{G_Y}$ into non-decreasing order, and identifying y_{low} and y_{high} with indices differing by pM [52]. Generally, there is more than one coverage interval for a specific coverage probability because any interval, within which Y_i lies with probability p, can be taken as a coverage interval [79]. For output vector $\boldsymbol{Y}$, however, determination of coverage interval is less straightforward, since it requires sorting multivariate data. Considering that the coverage interval represents the expanded uncertainty associated with the output estimate $\boldsymbol{y}$ [42], mostly the smallest coverage interval is of interest. In multivariate distributions, the smallest coverage region does not have a particular geometric definition and a hyper-volume integration can merely approximate its shape [50]. Nevertheless, in uncertainty evaluation, one can replace the smallest coverage region either with a hyper-ellipsoidal coverage region, which is close to the smallest region, or with a hyper-rectangular coverage region, which might be conservatively large. Supplement 2 to the GUM formulates a hyper-ellipsoidal coverage region as [50]

$$(\boldsymbol{\eta} - \boldsymbol{y})^{\mathrm{T}}\, \boldsymbol{U_y}^{-1} (\boldsymbol{\eta} - \boldsymbol{y}) = k_p^2 \qquad 5\text{-}11$$

where $\boldsymbol{y}$ (best estimate of output $\boldsymbol{Y}$) specifies its location, $\boldsymbol{U_y}$ (the covariance matrix associated with estimate $\boldsymbol{y}$) defines its shape, and k_p specifies its size while $\boldsymbol{\eta}$ is an independent parameter. Supplement 2 to the GUM also provides detailed instructions on how to determine k_p [50].

In the MCM, the numerical precision of the average (estimate) $\boldsymbol{y}$ of the measurand $\boldsymbol{Y}$ is expected to improve by one digit when the number of MCM trials increases by a factor of $M^{-0.5}$ [51]. For example, the numerical accuracy of $\boldsymbol{y}$ obtained by M trials of an MCM is likely to improve by one decimal digit after $100\times M$ trials. As a result, the convergence properties of the MCM is irrespective to the number of input quantities N [52]. Supplement 2 to the GUM establishes convergence criteria for an MCM, namely adaptive MCM [50]. After each sequence (consisting of

M=10^4 trials), the standard deviations obtained for estimates $\boldsymbol{y}$, standard uncertainties $\boldsymbol{u_y}$, maximum eigenvalue $\lambda_{\max}$ of the associated correlation coefficient matrix, and coverage factor k_p are calculated. In an adaptive MCM, the convergence criterion includes (after h =10 sequences) comparing these standard deviations with corresponding stipulated numerical tolerances. The numerical tolerance δ associated with output quantity Y_i is defined as [50]

$$\delta = \frac{1}{2}10^{l} \qquad 5\text{-}12$$

where l is the number of decimal digits of the significant figures considered for output quantity Y_i (Table 5-1). The simulator executes one more sequence if the convergence does not hold (Figure b).

In this study, the employed MCM simulator comprises the SAMBA numerical calibration procedure (Figure 5-2), described in section 2, as measurement model $f(\boldsymbol{X})$. The inputs of this function consist of 327 centre ball coordinates indications (including three Cartesian coordinates for each of the 109 ball measurements done during the calibration) plus the length of the SAMBA calibrated scale bar, therefore $N =$ 328. The experimental population, consisting of the experimental replications, yields the joint PDF of input quantities $\boldsymbol{X}$. For each of the 10^4 trials, the multivariate sample generator draws one input vector $\boldsymbol{x}$ at random (Eq. 5-7) and stores it in matrix $\boldsymbol{G_X}$ of dimension 328×10^4 (Figure b). Then, measurement function $f(\boldsymbol{X})$ processes each column of matrix $\boldsymbol{G_X}$ and returns m =13 scalar geometric errors listed in Table 5-1, stored in matrix $\boldsymbol{G_Y}$ of dimension 13×10^4. After each sequence of MCM, best estimate $\boldsymbol{y}$ (Eq. 5-9), the associated standard uncertainty $\boldsymbol{u_y}$, coverage factor k_p, and the maximum eigenvalue $\lambda_{\max}$ of the correlation matrix of the output quantities are calculated from the concatenation of all matrices $\boldsymbol{G_Y}$ from the executed sequences. Although only m =13 output quantities (the geometric errors listed in Table 5-1) are of interest, the SAMBA calibration function also returns the ball centre coordinates and the coordinates of the scale bar's ends, a total of 6×3 more output quantities. This reduction in the number of outputs from 31 to 13 does not affect the statistical properties of the generated population stored in matrix $\boldsymbol{G_Y}$ as well as on estimated covariance matrix, standard uncertainties, and the coverage factor of any single output quantity.

5.6 GUM uncertainty framework

In GUF, the propagation of uncertainties proceeds without propagating PDFs. In this method, the linear term of the Taylor series of measurement model $f(\boldsymbol{X})$ approximates the variations of measurand about its expected value due to small changes of the input quantities about their expected values [42]. Accordingly, covariance matrix $\boldsymbol{U_y}$ associated with output estimates $\boldsymbol{y}$ is [50]

$$\boldsymbol{U_y} = \boldsymbol{C_x}\, \boldsymbol{U_x}\, \boldsymbol{C_x}^{\mathrm{T}} \tag{5-13}$$

where $\boldsymbol{C_x}$ is the sensitivity matrix of dimension $m \times N$ given by evaluating

$$\boldsymbol{C_x} = \begin{bmatrix} \dfrac{\partial Y_1}{\partial X_1} & \cdots & \dfrac{\partial Y_1}{\partial X_N} \\ \vdots & \ddots & \vdots \\ \dfrac{\partial Y_m}{\partial X_1} & \cdots & \dfrac{\partial Y_m}{\partial X_N} \end{bmatrix} \tag{5-14}$$

at $\boldsymbol{X} = \boldsymbol{x}$, where $\boldsymbol{x}$ is an estimate of input quantity $\boldsymbol{X}$. Because of the numerical approach (Figure 5-2a) used in the SAMBA calibration function, no explicit mathematical form of this function is available. Nevertheless, numerical differentiation can approximate the partial derivatives of Eq. 5-14. Figure 5-3 shows the calculation procedure of the jth column of the sensitivity matrix (Eq. 5-14), i.e. the partial derivatives of the SAMBA calibration function with respect to $X_{\boldsymbol{j}}$, the j^{th} input quantity at $\boldsymbol{X} = \boldsymbol{x}$. The step size in the numerical differentiation (Figure 5-3) is $u(x_j)$, the standard uncertainty associated with estimate x_j of input quantity X_j [42].

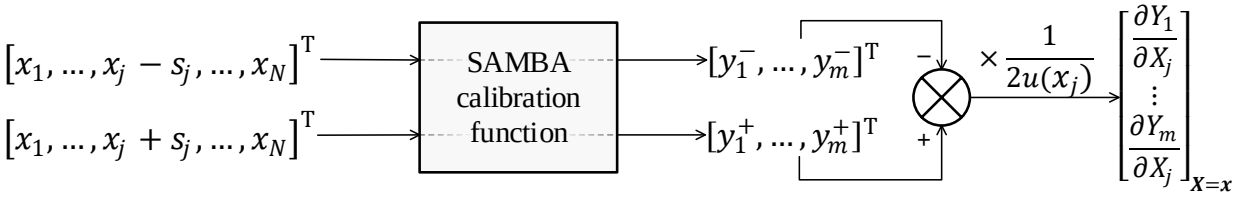

Figure 5-3: Numerical differentiation of the SAMBA calibration function at $\boldsymbol{X} = \boldsymbol{x}$ with respect to X_j, the jth input quantity.

The evaluation of measurement function $f(\boldsymbol{X})$ at $\boldsymbol{X} = \boldsymbol{x}$ gives estimate $\boldsymbol{y}$ of output quantities $\boldsymbol{Y}$. Assuming a normal joint PDF for the m =13 outputs, GUF specifies hyper-ellipsoidal coverage factor k_p =4.73 for coverage probability $p = 0.95$ [50].

5.7 Results and discussion

Any systematic variation in the initial measurements, i.e. the coordinates recorded on the experimental replications of SAMBA, can considerably enlarge the variance of the assigned distributions and can falsify the correlation between the input quantities. Such large standard deviations can affect the validity of the GUF results, which approximates the output uncertainty of a function in terms of small deviations of input values [42]. Inspecting the trend of the recorded raw data for any probable drift or systematic behaviour and taking actions to reduce it can help the agreement between the adaptive MCM and the GUF evaluations. Figure 5-4 illustrates the typical variations of a ball centre coordinates measured in the experimental replications of SAMBA. Systematic trends are hardly distinguishable in the measured coordinates which are fairly equally spread around the mean value through the sequence. The acquisition of data under almost the same thermal conditions of the machine tool and with the same experimental factors, including measurement strategy and speed, can cause the random behaviour of the recorded data (Figure 5-4). However, the laboratory uses an environment control similar to the university classrooms. Therefore, some levels of temperature variation are expected, which could contribute to the randomness of the records. Other machine variation sources as well as some lack of repeatability of the touch probe, could also contribute [103].

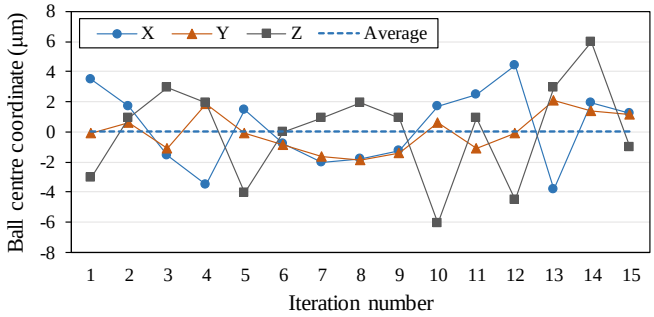

Figure 5-4: Variations of the centre coordinates of ball 3 around their average (the zero line) measured in the experimental replications of SAMBA.

Table 5-2 presents the estimates of machine errors and the associated standard uncertainties obtained by the adaptive MCM and the GUF procedures. The machine reference frame (X_m, Y_m, Z_m) determines the sign of the estimated geometric errors while the direction of the angular errors follows the right-hand rule (Figure b). The adaptive MCM results are also shown in Figure 5-5, grouped into three categories; the angular errors, the translational errors, and the linear terms (slopes) of the linear positioning errors. Table 5-2 also includes the experimental results, in which only the experimental replications shape the population of input vectors (rather than thousands of random input vectors drawn at random from the assigned joint PDF). Table 5-3 includes $\lambda_{\max}$, the maximum eigenvalue of the correlation matrix of machine errors, and k_p, the coverage factor according to the hyper-ellipsoidal coverage region, specified by these three approaches. Adhering to Supplement 2 to the GUM [50], the differences between the MCM and the GUF results remain within the corresponding numerical tolerances (Eq. 5-10) advised by this standard, which suffices to validate GUF. As a result, GUF is not only efficient but also adequately accurate to replace MCM for the uncertainty evaluation of a machine tool calibration via SAMBA. Depending on the specified numerical tolerance and the speed of computation, an MCM task might require weeks to complete. The most demanding part of the employed MCM code is calling the SAMBA calibration function, i.e. measurement model $f(\boldsymbol{X})$. All the quantities listed in Table 5-2 and Table 5-3 converge before or by 10 sequences ($h = 10$), for an almost 24 h runtime (on a computer with an Intel i7 processor running at 4.2 GHz using 32 GB of RAM, running Windows version 10). Considering the rate of MCM convergence, increasing the number of significant digits (Table 5-1) by one would considerably increase the runtime required for convergence. On the other hand, GUF efficiently evaluates the uncertainty, in less than 10 min, by the analytic equation given in Eq. 5-13 and through a numerical differentiation according to Eq. 5-14.

Table 5-2 includes the MCM results and the results obtained by the experimental replications. The maximum difference between the values obtained for the geometric error estimates is smaller than 1%, although that for the associated uncertainties is 47% and belongs to E_{YY1} (Table 5-2). The conformity of the MCM estimates with those obtained by experimental replications implies that the marginal means of the joint PDF estimated for the output vector in the adaptive MCM well represent the average of the output quantities. However, for the uncertainty of the linear terms (slopes) of the linear positioning errors, i.e. E_{XX1}, E_{YY1}, and E_{ZZ1}, the standard deviations estimated

by the experimental data and by the adaptive MCM show notable differences, causing the joint PDF to stretch along these directions. This difference is most likely due to introducing the standard uncertainty of the scale bar length to the joint PDF of the input vector. For $\lambda_{\max}$ and k_p (Table 5-3), the differences between the MCM and the experimental results are 10% and 31%, respectively. For a small output population, as in the experiments, coverage factor k_p is highly sensitive to the number and the distribution of output points in $\mathbb{R}^m$ (in this study, the 13-dimensional domain of the output vector). Particularly for the 15 trials of the experimental replications, a hyper-ellipsoidal coverage region for coverage probability of almost $p = 0.95$ has to encompass 14 output points. Then, the position of a single point can notably vary the coverage factor, which specifies the size of the coverage region. Then, the limited number of experimental replications can explain the difference between the coverage factors determined by the experiments and the adaptive MCM.

The geometric error estimates given in Table 5-2 are calculated based on the best estimate of the 328 input quantities, which is obtained by averaging over the probing results of the experimental replications. However, in this table, the standard uncertainties belong to any output vector of only one implementation of the SAMBA method. If one estimates the geometric errors of a machine tool by carrying out k replications of the SAMBA process, any uncertainty evaluation should be done based on the experimental standard deviations associated with the mean of the k input vectors [42]. As a result, the experimental uncertainty associated with the machine parameters obtained through k replications of the SAMBA procedure can be estimated by dividing the standard uncertainties given in Table 5-2 by $\sqrt{k}$. Particularly, in order to estimate the standard uncertainties associated with the geometric error values given in Table 5-2, the standard uncertainties presented in this table have to be divided by $\sqrt{15}$ (≈ 3.9).

Table 5-2: Error estimates y and standard uncertainty u_y evaluated by the adaptive MCM, the experimental replications (Exp.) and GUF (results with one digit more than the number of significant digits presented in Table 5-1).

Error	Best estimate y			Standard uncertainty u_y			Is GUF validated?
	Exp.	MCM	GUF	Exp.	MCM	GUF	
E_{A0B} (μrad)	-8.73	-8.73	-8.77	0.86	0.86	0.87	Yes
E_{C0B} (μrad)	-2.80	-2.80	-2.83	0.80	0.80	0.79	Yes
E_{X0C} (μm)	-104.59	-104.59	-104.59	0.48	0.48	0.48	Yes
E_{A0C} (μrad)	-18.75	-18.75	-18.73	0.86	0.86	0.87	Yes
E_{B0C} (μrad)	-4.40	-4.41	-4.41	0.96	0.96	0.97	Yes
E_{B0Z} (μrad)	-12.23	-12.24	-12.28	1.26	1.26	1.26	Yes
E_{A0Y} (μrad)	-13.87	-13.86	-13.89	1.12	1.12	1.12	Yes
E_{C0Y} (μrad)	25.81	25.81	25.76	0.89	0.89	0.89	Yes
E_{XX1} (μm/m)	75.6	75.6	75.4	4.6	6.1	6.1	Yes
E_{YY1} (μm/m)	102.0	102.0	101.8	3.7	5.4	5.4	Yes
E_{ZZ1} (μm/m)	113.4	113.3	113.2	3.8	5.5	5.5	Yes
E_{Y0S} (μm)	18.72	18.72	18.73	0.88	0.88	0.89	Yes
E_{X0S} (μm)	-107.15	-107.15	-107.15	1.04	1.03	1.03	Yes

Table 5-3: The maximum eigenvalue $\lambda_{\max}$ of the correlation matrix and coverage factor k_p of hyper-ellipsoidal coverage region for coverage probability 0.95 obtained by the adaptive MCM, the experimental replications (Exp.), and GUF.

Validation parameter	Exp.	MCM	GUF	Is GUF validated?
Maximum eigenvalue $\lambda_{\max}$ of correlation matrix	4.99	4.47	4.46	Yes
Coverage factor k_p	3.61	4.73	4.73	Yes

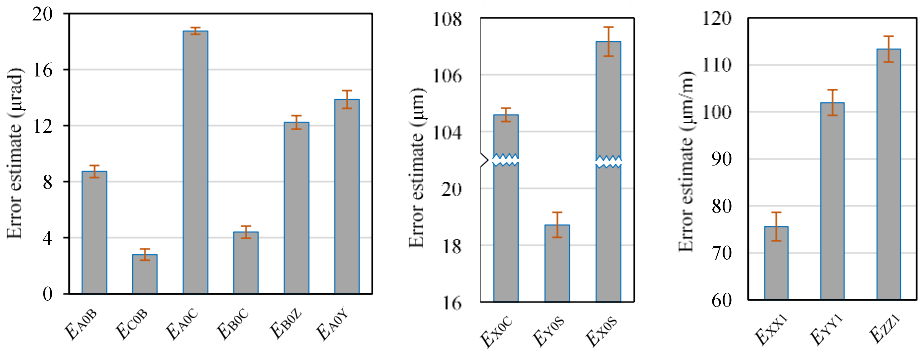

Figure 5-5: Error estimates (absolute values) and the associated standard uncertainty evaluated through the adaptive MCM. Errors are grouped into three categories; the angular errors, the translational errors, and the linear terms (slopes) of the linear positioning errors.

The following are three examples from the most to the least correlated geometric error estimates including the comparisons between the GUF and the MCM results. Table 5-4 includes the superposition of the correlation and the covariance matrices obtained by the adaptive MCM. According to this table, the linear terms (slopes) of the linear positioning errors of the prismatic joints E_{XX1}, E_{YY1}, and E_{ZZ1} are the most correlated machine errors. Sensitivity analysis of these three outputs by studying the corresponding rows of the sensitivity matrix $\boldsymbol{C_x}$ (Eq. 5-14), which represent the gradient of each output, demonstrates their significant dependency on the standard uncertainty of the SAMBA scale bar length. Figure 5-6 shows the gradient magnitudes of the machine geometric errors and their partial derivatives with respect to the SAMBA scale bar length. The largest partial derivative magnitudes of these errors are the ones with respect to the length of the scale bar and almost equal to 3.34×10^{-3} μm/m^2, denoting 88%, 87%, and 84% of the magnitudes of the gradients of E_{XX1}, E_{YY1}, and E_{ZZ1}, respectively (Figure 5-6). Therefore, these three functions are likely to show the same variation trends in most directions, which can cause high correlation coefficients. SAMBA calibrates the prismatic joints in a way that it identifies the relative positioning errors using the isolated balls, and determines their magnitudes by measuring, at least once, the length of the scale bar. As a result, one can expect that the three linear terms vary with full correlation (Table 5-4) by changing the measured length of the scale bar because of, for example, thermal variations or simply via some machine or probe related non-repeatable factors.

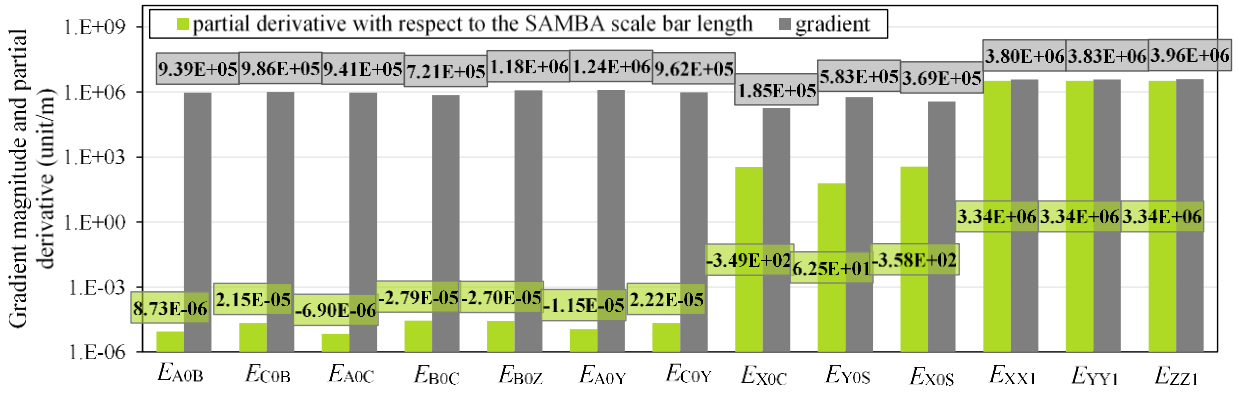

Figure 5-6: The gradient magnitudes of the geometric errors and their partial derivatives with respect to the SAMBA scale bar length. The green columns represent the absolute values of the partial derivatives whose numerical values are shown as data labels.

Table 5-4: Superposition of the correlation and the covariance matrices obtained by the adaptive MCM. The upper triangular part of the matrix includes the correlation coefficients and the lower triangular part together with the diagonal elements include the covariance values. The color spectrum denotes the absolute values of the correlation coefficients.

	E_{A0B}	E_{C0B}	E_{X0C}	E_{A0C}	E_{B0C}	E_{B0Z}	E_{A0Y}	E_{C0Y}	E_{XX1}	E_{YY1}	E_{ZZ1}	E_{Y0S}	E_{X0S}
E_{A0B}	7.4e-01	0.189	-0.035	0.058	-0.089	0.365	0.509	0.415	0.037	0.008	0.255	-0.641	-0.297
E_{C0B}	1.3e-01	6.3e-01	-0.486	0.163	0.254	0.204	0.534	0.828	0.276	0.199	0.274	0.100	-0.491
E_{X0C}	-1.5e-02	-1.9e-01	2.3e-01	-0.163	0.080	0.136	-0.438	-0.275	-0.103	-0.049	0.025	0.019	0.540
E_{A0C}	4.3e-02	1.1e-01	-6.8e-02	7.5e-01	-0.328	0.005	0.517	0.012	-0.209	-0.143	-0.135	-0.497	0.060
E_{B0C}	-7.4e-02	2.0e-01	3.7e-02	-2.7e-01	9.3e-01	0.577	0.061	0.174	0.430	0.377	0.340	0.385	-0.207
E_{B0Z}	4.0e-01	2.0e-01	8.2e-02	5.3e-03	7.0e-01	1.6e+00	0.096	0.283	0.113	0.124	0.301	-0.315	-0.141
E_{A0Y}	4.9e-01	4.8e-01	-2.4e-01	5.0e-01	6.6e-02	1.4e-01	1.3e+00	0.489	0.183	0.174	0.222	-0.300	-0.398
E_{C0Y}	3.2e-01	5.9e-01	-1.2e-01	9.2e-03	1.5e-01	3.2e-01	4.9e-01	7.9e-01	0.380	0.328	0.444	0.002	-0.672
E_{XX1}	1.9e-01	1.3e+00	-3.0e-01	-1.1e+00	2.5e+00	8.6e-01	1.2e+00	2.1e+00	3.7e+01	0.965	0.906	0.273	-0.580
E_{YY1}	3.9e-02	8.6e-01	-1.3e-01	-6.7e-01	2.0e+00	8.4e-01	1.1e+00	1.6e+00	3.2e+01	2.9e+01	0.929	0.259	-0.472
E_{ZZ1}	1.2e+00	1.2e+00	6.6e-02	-6.4e-01	1.8e+00	2.1e+00	1.4e+00	2.2e+00	3.0e+01	2.8e+01	3.0e+01	0.003	-0.444
E_{Y0S}	-4.9e-01	7.0e-02	8.2e-03	-3.8e-01	3.3e-01	-3.5e-01	-3.0e-01	1.4e-03	1.5e+00	1.2e+00	1.3e-02	7.8e-01	0.001
E_{X0S}	-2.6e-01	-4.0e-01	2.7e-01	5.4e-02	-2.1e-01	-1.8e-01	-4.6e-01	-6.2e-01	-3.6e+00	-2.6e+00	-2.5e+00	7.3e-04	1.1e+00

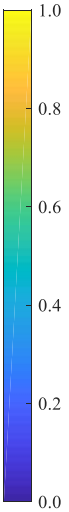

Figure 5-7a illustrates the ellipsoidal and the rectangular coverage regions, for coverage probability p =0.95, specific to E_{XX1} and E_{YY1} by means of the adaptive MCM and the GUF evaluations, along with 2,000 random output points. In this figure, also shown are the outputs of experimental replications together with the coverage regions obtained in the experiments. The areas of the ellipsoidal coverage regions specified by GUF and the adaptive MCM (161.8 and 160.5 $\mu m^2/m^2$, respectively) are comparable, although GUF overestimates the area of the rectangular region (657.3 $\mu m^2/m^2$) compared to that obtained by the adaptive MCM (548.9 $\mu m^2/m^2$). Although not required by supplement 2 to the GUM [50], the size of the hyper-ellipsoidal coverage region obtained by GUF is also compared with an approximated size of the smallest coverage region. The latter is estimated by creating hyper-rectangular regions (meshes) region in the space of the MCM output quantities [50]. The area of the smallest coverage region is almost 158.9 $\mu m^2/m^2$ that is 2% smaller than the areas of the GUF ellipsoidal regions. The areas of the ellipsoidal and the rectangular coverage regions specified by the experiments are 96.1 and 269.0 $\mu m^2/m^2$, respectively, 40% and 51% times smaller than the areas obtained by the adaptive MCM (Figure 5-7a). Excluding the

uncertainty of the scale bar from the MCM analysis suggests that such a difference is mostly because of the length uncertainty of the SAMBA scale bar that is not involved in the experiment results. However, even without the length uncertainty being involved, the experiment results are less likely to provide a coverage region close enough to the ones obtainable with the adaptive MCM

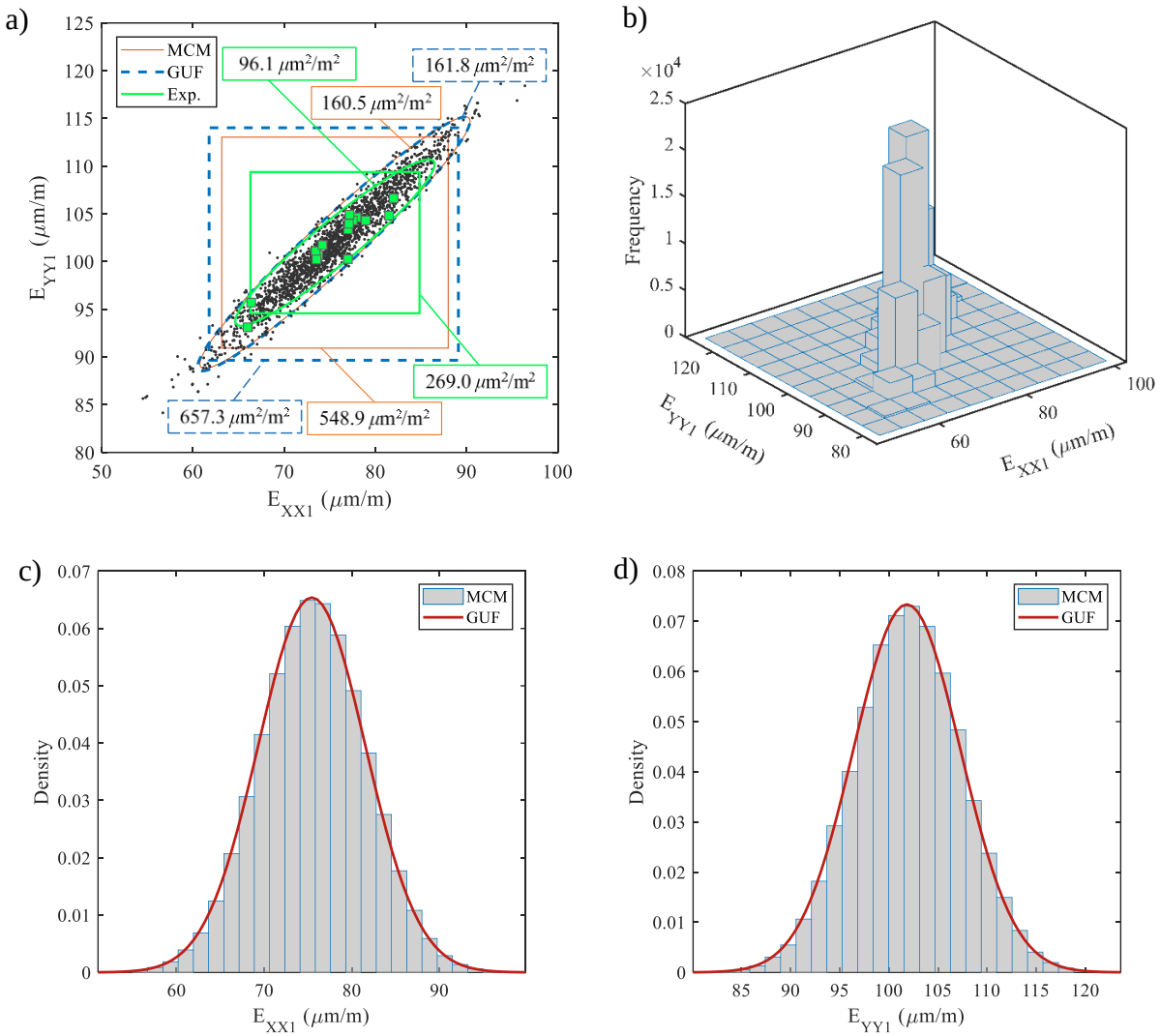

Figure 5-7: a) Ellipsoidal and rectangular coverage regions obtained by the experiments (Exp.), the adaptive MCM, and the GUF analyses for E_{XX1} and E_{YY1} (for coverage probability p =0.95) together with 2,000 points drawn at random from the joint PDF of the outputs and the 15 outputs obtained experimentally. b) 3D histogram of the outputs based on the adaptive MCM, and comparison between the adaptive MCM and the GUF histograms for c) E_{XX1} and d) E_{YY1}.

and the GUF procedures. Because, as mentioned before, the size and the area of a coverage region strongly depends on the position of a single output quantity. A single row of the histogram bins in the joint PDF of these errors (Figure 5-7b) also suggests a high correlation between them. Figure 5-7c and d compare the PDFs of E_{XX1} and E_{YY1} determined by the adaptive MCM and the GUF approaches.

After the positioning errors of the prismatic joints, the out-of-squareness of axes B (E_{C0B}) and Y (E_{C0Y}) relative to axis X are the most correlated machine errors (Table 5-4). Figure 5-8a depicts 2,000 random points of these errors along with the ellipsoidal and rectangular coverage regions for coverage probability $p = 0.95$. The ellipsoidal coverage regions are less stretched compared with the regions obtained for the positioning errors (Figure 5-8a), showing a smaller correlation between the two out-of-squareness errors. The areas of the ellipsoidal regions specified by the adaptive MCM and GUF are comparable (7.5 μrad^2). The area of the smallest coverage region is almost 7.4 μrad^2, which is 1% smaller than the ellipsoidal area specified by the adaptive MCM. The experimental results determine the areas of the ellipsoidal (4.7 μrad^2) and rectangular (10.0 μrad^2) coverage regions smaller than those specified by the adaptive MCM. Figure 5-8b illustrates the joint PDF of the same errors and Figure 5-8c and d compare the PDFs of the same errors obtained using the adaptive MCM and the GUF evaluations. Considering the topology of the machine (Figure b), E_{C0B} and E_{C0Y} model the out-of-squareness errors to the same primary axis X and are occurring in parallel planes in the machine frame, i.e. the XY plane. This makes both errors have related, but not identical, effects on the vector of volumetric error. Any indirect calibration process should be able to separate these effects to identify these geometric errors. Despite probing SAMBA at various axis positions and rotary axes angular position, a portion of the effects of these errors still seems to remain coupled, which can account for the considerable correlation (0.828 μrad^2) between E_{C0B} and E_{C0Y} (Table 5-4). Optimization of the SAMBA measurement strategy might address this issue and decrease the correlation between such coupled output variables. However, there is also the possibility that a physical correlation exists whereby some common factors affect both errors simultaneously.

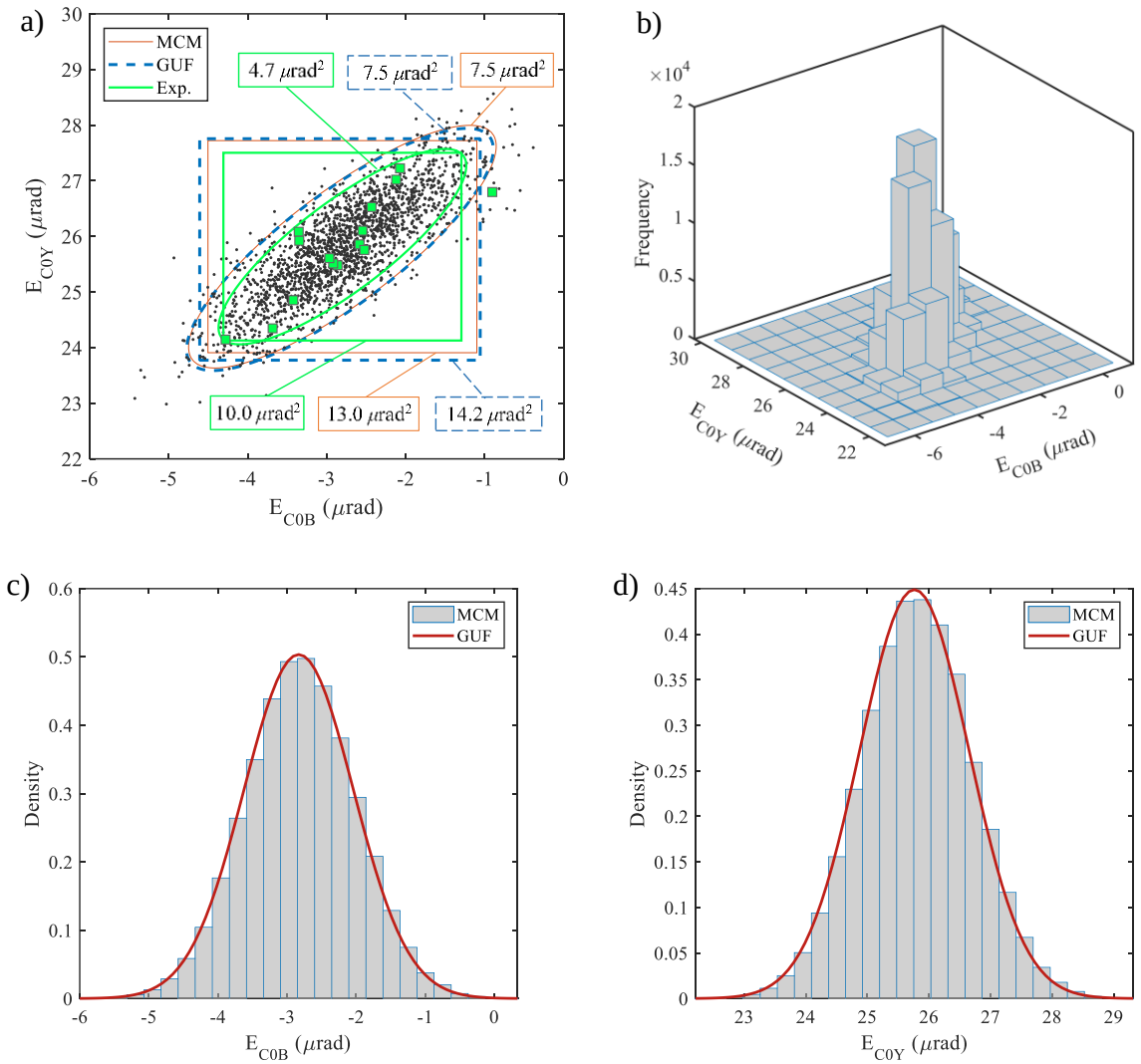

Figure 5-8: a) Ellipsoidal and rectangular coverage regions obtained by the experiments (Exp.), the adaptive MCM, and the GUF analyses for E_{C0B} and E_{C0Y} (for coverage probability p =0.95) together with 2,000 points drawn at random from the joint PDF of the outputs and the 15 outputs obtained experimentally. b) 3D histogram of the outputs based on the adaptive MCM, and comparison between the adaptive MCM and the GUF histograms for c) E_{C0B} and d) E_{C0Y}.

The least correlated machine errors are E_{Y0S} and E_{X0S} with a correlation coefficient of 0.001 (Table 5-4). The ellipsoidal coverage region for coverage probability p =0.95 is more circular (Figure 5-9a) and the sizes of these coverage regions are closer to the rectangular regions compared with the more correlated outputs studied before (Figure 5-7a and Figure 5-8a). The areas of the

ellipsoidal regions determined by the adaptive MCM and the GUF analyses are 17.1 and 17.4 μrad^2, respectively. Amongst all the output pairs, the area of the rectangular coverage region obtained for E_{Y0S} and E_{X0S} using GUF (18.3 μrad^2) is the closest to its counterpart obtained by the adaptive MCM (18.2 μrad^2). The area of the smallest coverage region (obtain based on the MCM results) is

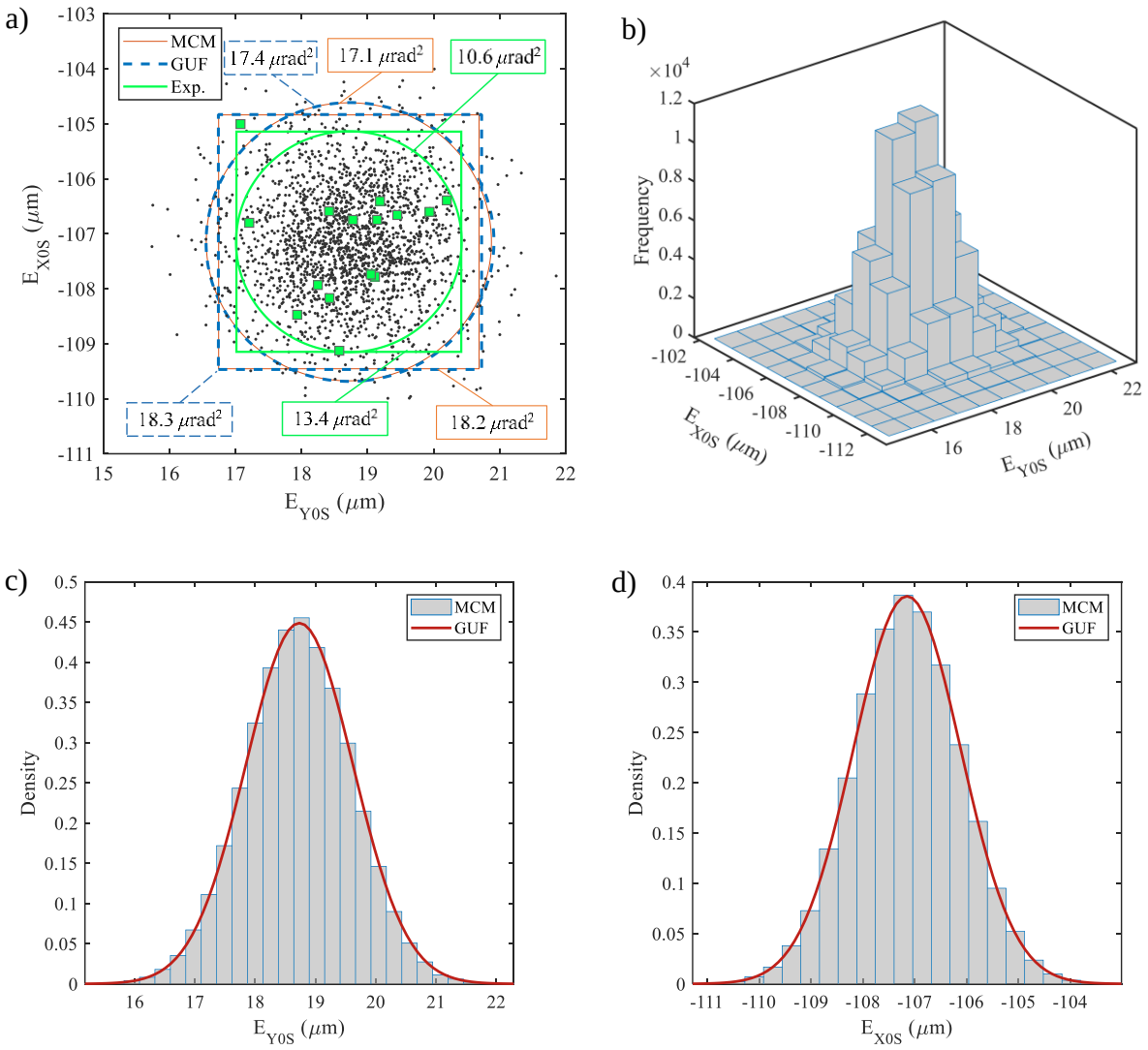

Figure 5-9: a) Ellipsoidal and rectangular coverage regions obtained by the experiments (Exp.), the adaptive MCM, and the GUF analyses for E_{Y0S} and E_{X0S} (for coverage probability p =0.95) together with 2,000 points drawn at random from the joint PDF of the outputs and the 15 outputs obtained experimentally. b) 3D histogram of the outputs based on the adaptive MCM, and comparison between the adaptive MCM and the GUF histograms for c) E_{Y0S} and d) E_{X0S}.

almost 16.73 μrad^2, which is 4% smaller than the ellipsoidal area given by GUF. The experimental areas of the ellipsoidal and the rectangular coverage regions are 10.6 and 13.4 μrad^2, respectively, which notably differ from the values obtained by the adaptive MCM and the GUF approaches. Figure 5-9b depicts the joint PDF of the error, which is mostly symmetric with respect to both variables. Figure 5-9c and d illustrate the comparable PDFs acquired by the adaptive MCM and the GUF evaluations for E_{Y0S} and E_{X0S}.

5.8 Conclusions

In this study, we evaluate the uncertainty associated with the indirectly estimated geometric errors of a machine tool identified by on-machine touch probing of a scale and master ball artifact (SAMBA). First, an adaptive MCM simulator evaluates the estimates of the geometric errors and the associated uncertainties. The input of the adaptive MCM is a vector of length 328, including the length of the SAMBA scale bar as well as the coordinates of 109 SAMBA ball centres as the measured machine coordinates of four balls probed using the linear axes for different angular positions of the rotary axes. The outputs are 13 geometric errors of the machine tool. Repeating the calibration of a Mitsui Seiki® five-axis machine tool model HU40-T equipped with a Renishaw® MP 700 touch-trigger probe over 15 days provides an initial sample of experimental replications to approximate the joint PDF of the input quantities. Then, adhering to Supplement 2 to the GUM, the results of the adaptive MCM examine the feasibility of the SAMBA uncertainty evaluation through GUF. The estimates of the geometric errors, the standard uncertainty associated with the estimates, the coverage factor for coverage probability $p = 0.95$, and the maximum eigenvalue of the output correlation matrix are the validation criteria. In addition, comparing the experimental results to the geometric error estimates obtained by the adaptive MCM simulator examines the reliability of the marginal means of the joint PDF assigned to the output quantities. Below are the most important conclusions:

1. GUF can replace the adaptive MCM for the uncertainty evaluation of machine tool geometric errors identified by SAMBA. Comparing the adaptive MCM and the GUF results demonstrates that the linearization of the SAMBA calibration function via the Taylor series through GUF gives an adequately accurate approximation of the function. Besides the

validation criteria, the areas of the ellipsoidal and the rectangular coverage regions obtained by MCM and GUF are also comparable.

2. Comparing the experimental and the adaptive MCM results signifies the reliability of the means of the joint PDF assigned to the output quantities in the adaptive MCM uncertainty evaluation. The maximum difference between the estimates obtained by the adaptive MCM and the experiments does not exceed 1%. However, for the uncertainties associated with the linear terms (slopes) of the linear positioning errors, this difference is up to 47%, which is most likely because of introducing the standard uncertainty of the scale bar length to the joint PDF of the input vector in the MCM procedure.
3. The linear terms (slopes) of the linear positioning errors of the prismatic joints E_{XX1}, $E_{YY1,}$ and E_{ZZ1}, are the most correlated machine errors. A sensitivity analysis reveals their significant dependency on the length of the SAMBA scale bar so that the partial derivative magnitudes of these errors with respect to the length of the scale bar are 88%, 87%, and 84% of the norms of the gradients of E_{XX1}, $E_{YY1,}$ and E_{ZZ1}, respectively. Then, the dependence of these errors on the measured length of the scale bar, which can vary due to thermal drift of the machine, may also account for the high correlation values.

5.9 Acknowledgments

This research was supported in part by Natural Sciences and Engineering Research Council of Canada (NSERC) under the CANRIMT2 Strategic Research Network Grant NETGP 479639-15, and in part by the NSERC Discovery Grant of the last author. The authors would like to thank Dr. Kanglin Xing for providing the experimental calibration data.

CHAPTER 6 : ARTICLE 3: A FULL COVARIANCE MATRIX METHOD FOR UNCERTAINTY ASSESSMENT IN ON-MACHINE PROBING

Submitted to: International Journal of Machine Tools and Manufacture, February 2021

Authors: Saeid Sepahi-Boroujeni[*a]; J.R.R. Mayer[a]; Farbod Khameneifar[a]; Adam Woźniak[b]

6.1 Abstract

Despite the growing use of machine tools for in-process measurement, the uncertainty evaluation of on-machine probing has mostly remained limited to the method specifically developed in ISO 15530-3 for coordinate-measuring machines. These methods reduce the on-machine measurement problem to a single-output system, so that the law of propagation of uncertainty becomes applicable, which excludes any covariance effect between the input quantities. This study proposes a methodology that inclusively estimates the uncertainty associated with any probing within the working space of a five-axis machine tool. Defined by the machine's forward kinematic model, the on-machine measurement function receives the machine's geometric errors and the axis positions for a probed point set, and estimates its compensated position in the workpiece frame. The proposed uncertainty estimator assembles the covariance matrices associated with these input quantities and evaluates the measurement uncertainty through an adaptive Monte Carlo method. Unlike the task-specific method given by ISO 15530-3, this scheme eliminates the need for any part's calibrated counterpart and involves the covariance between the input quantities. The experimental verification of the new method includes the on-machine measurement of a gauge's length and the diameter and sphericity of a precision sphere through highly diverse axis positions of a five-axis machine tool. Over the 225 possible combinations of 15 point sets (each of size 2) probed on the gauge block, the coverage probability of the expanded uncertainty (for a coverage factor of 2) estimated for the gauge's length is 90%. Then, 10 point sets (each of size 25) collected on the sphere create 10 accumulated pools, and from each, 200 randomly drawn samples estimate the sphere's diameter.

---

[*] Corresponding author
[a] Department of Mechanical Engineering, Polytechnique Montreal, Montreal, QC H3T 1J4, Canada
[b] Warsaw University of Technology, Institute of Metrology and Biomedical Engineering, ul. Św. A. Boboli 8, 02-525 Warsaw, Poland

The coverage probabilities of the expanded uncertainty estimated for the pools built of up to 7 point sets remain above 94%. These levels of confidence are comparable to the theoretical level (95%).

Keywords: Uncertainty; On-machine measurement; Covariance; Five-axis machine tool; Monte Carlo

6.2 Introduction

The measurement capability of machine tools, imparted by installing touch probes, has improved both the efficiency and accuracy of manufacture. Measuring a machined part in situ prevents inspection bottlenecks and provides the feedback required for readjusting the process parameters [15]. This advantage, however, introduces a new challenge, being ensuring the traceability of the on-machine measurement results, which calls for a reliable uncertainty assessment.

Besides measurement capacity, any behaviour quantification of machine tools is complete only if it comes with an uncertainty metric. Stability analysis of machining process [104], control of chatter [105, 106], thermal deflections [107], and kinematic error identification [108, 109] are a few among many studies where uncertainty evaluation establishes the tractability of results.

The guide to the Expression of Uncertainty in Measurement (GUM) [42] presents the law of propagation of uncertainty based on a linear Taylor approximation of the measurement function. This method forms the basis of the uncertainty assessment in the identification of many machining systems [110, 111]. Supplement 2 to the GUM [50] includes a modification to this law that allows the uncertainty evaluation of multi-dimensional problems through the GUM uncertainty framework. According to this document, however, a Monte-Carlo-method (MCM) validation, which is already established in Supplement 1 to the GUM [79], is required to certify the uncertainty calculated through the GUM uncertainty framework. For this purpose, Supplement 2 to the GUM [50] specifies an adaptive MCM that ensures the results stabilize in the statistical sense by conducting an adequately large number of MCM trials.

Machine tools share many kinematic features with coordinate measuring machines (CMMs). Following ISO 15530-3 [1], Štrbac et al. [99] study the influence of thermal effect on systematic error and measurement uncertainty in the CMM measurement of the diameter and roundness of a ring gauge. They report significant growth in the standard uncertainty of the diameter by increasing

the system temperature. Mussatayev et al. [112] also detect a significant contribution of thermal effects, raised by long-term measurement tasks, to the uncertainty of the CMM measurement of a hole plate standard. Harmatys et al. [113] study the effect of a warm-up period on the measurement accuracy of an optical CMM. Studying the measurement results obtained during and after warm-up periods, they report a considerable increase in measurement uncertainty by rising the part temperature, which they attribute to the thermal deflection of the part rather than that of the machine.

Resorting to the methods established specifically for the uncertainty evaluation of CMM measurement, such as those proposed in ISO 15530 [1, 2], is the approach most adopted to address the traceability of on-machine measurements [36, 44-47]. However, this practice brings about new challenges. First, the differences between CMMs and machine tools in terms of working conditions, maintenance routines, and environment require specific studies on dominant uncertainty contributors to on-machine measurement. Second, fabricating and calibrating a counterpart for any new workpiece would be costly, especially when it comes to large part machining.

The instruction specified in ISO 15530-3 [1] evaluates the standard uncertainty of task-specific measurements. That is, the evaluated uncertainty resulting from this standard only suits the intended measurement task. Such a simplification saves much time and computation cost only if the probing process, as well as the factors contributing to the measurement uncertainty, remain unchanged during the measurement tasks conducted on the products selected for quality control. However, machine tools are known for their unsteady conditions caused by the uncontrolled environment of the shop floor. In different terms, the varying state of a machine tool, in both the short and long term, can affect the credibility of the measurement uncertainty evaluated by the replacement method documented in ISO 15530-3. More specifically, the repeatability of a machine tool could vary from time to time, although studying this effect on a certain machine tool demonstrates the stability of the short-term repeatability of on-machine measurements [103]. Moreover, the geometric errors of the machine tool and in turn, the measurement bias are likely to change in the long term with the thermal conditions of the machine and the environment [41].

Besides these challenges, the main disadvantage of the present guidelines on the uncertainty evaluation for CMMs is the absence of any covariance analysis between the input quantities. The formula given by ISO 15530-3, which stems from the law of propagation of uncertainty, neglects

the covariance term in the expectation of a squared first-order Taylor expansion of the measurement function about the expectations of the input variables. This can be understood by considering an underlying causal relationship between certain probed coordinates and the bias of on-machine measurement results. For instance, the changes in a machine tool's geometric errors can simultaneously affect certain probed coordinates and the measurement bias, implying a correlation between them.

Through a task-specific scheme for uncertainty evaluation, Mutilba et al. [45] investigate the major uncertainty contributors in on-machine measurement under the shop-floor conditions. They machine a workpiece including several geometric features and then calibrate each feature on a CMM. Conducting on-machine measurements on the machined part and through an uncertainty evaluation according to ISO 15530-3, they quantify the contribution of each uncertainty term specified by this standard. They report that the repeatability of on-machine measurement is the main uncertainty contributor. They find this factor even more dominant for the on-machine measurement following the machining process, which they attribute to the changes in thermal conditions. They also detect a strong correlation between the geometric errors of the machine tool and the systematic errors of the on-machine measurement results and conclude that the machine's geometric errors are the major contributors to the uncertainty associated with the bias of measurement results.

Following the ISO 15530-3 instruction, the user's knowledge about the machine's systematic error contribution to the measurement uncertainty is only obtainable through a calibrated workpiece installed at a certain position on the machine tool. To overcome this limitation and the need for a calibrated workpiece, Mutilba et al. [44] quantify the uncertainty associated with the systematic errors with a laser tracer right before conducting the on-machine measurement. This allows them to obtain the volumetric error of each probed point, and accordingly, calculate the measurement bias of a calculated feature, i.e. the difference between the feature calculated directly from the probed point set and that obtained after correcting each point by subtracting the corresponding volumetric error. Skipping the evaluation of the uncertainty associated with this measurement bias, they directly introduce this error (as an uncertainty source) into the equation given by ISO 15530-3. They also follow the instruction specified in this standard to calculate the probing repeatability through replicated measurements of the workpiece. Then, they validate the standard uncertainty

associated with each estimated feature through the results [45] obtained using the ISO 15530-3 method and show the feasibility of eliminating the calibrated workpiece from the uncertainty evaluation process suggested by this standard.

In another implementation of the existing methods for the uncertainty evaluation of CMMs, Gąska et al. [114] developed a virtual CMM-based model into an uncertainty estimator for five-axis measuring systems by drawing an analogy between the rotary axes of an articulated probe head installed on a CMM and those of a five-axis machine tool. Including in their model the systematic errors of both the CMM kinematic structure and the probe, they evaluate the uncertainty associated with a calculated feature through an MCM simulation. For this purpose, they deviate the probed coordinates of each point based on the distribution of volumetric errors obtained with a laser tracer. By comparing the model outcomes with the calibrated values, they verify their model for the Geometric Dimensioning and Tolerancing (GD&T) applications via on-machine measurement. Despite promising results, this methodology lacks the covariance analysis for the input quantities including the five axis positions, the three coordinates defining the probing direction, and the systematic errors.

Unlike any other existing approach to uncertainty evaluation of on-machine measurement, the methodology proposed in this paper concerns the covariance between the input quantities of the measurement function. Moreover, benefiting from an indirect machine error identifier, i.e. the scale and master ball artifact (SAMBA) [26], the proposed method obviates the need for a calibrated workpiece resembling the concerned workpiece (as specified in ISO 15530-3) and provides an inclusive uncertainty evaluator that ensures the metrological traceability irrespective of the workpiece's position on the machine. Experimental on-machine probing of a gauge block and a precision sphere verify that the uncertainty estimate provides coverage probability comparable to the expected value (95% for a coverage factor of 2).

6.3 Uncertainty estimation with an adaptive Monte Carlo method

In the context of this project, the on-machine assessment of a geometric feature includes three main steps (Figure 6-1). The first step is to identify the geometric errors of the machine (machine parameters). As an indirect error identifier, the SAMBA's algorithm estimates the machine parameters based on the raw measurements of the centre of the balls obtained through a series of

on-machine measurements of its artifact. Then, in the second step, an error compensator, which operates as the on-machine measurement function, receives these machine's imperfections and builds the machine's forward kinematic model that uses the workpiece probing results recorded as axis positions to calculate the compensated position of the probed point set in the workpiece frame. Finally, a GD&T function calculates the deviation of the geometric feature of interest. The uncertainty evaluation of on-machine measurement includes the propagation of the uncertainty associated with the input quantities through these steps with a tailored adaptive MCM. To do so, the covariance matrices associated with the machine parameters (the orange matrix in Figure 6-1) and the probing results (the blue matrices in Figure 6-1) assemble (the multicoloured matrix in Figure 6-1) and provide the on-machine measurement function with the covariance matrix associated with its inputs. This matrix includes the covariance of the probed axis positions among themselves (the purple matrix in Figure 6-1) and the machine parameters (the yellow matrix in Figure 6-1).

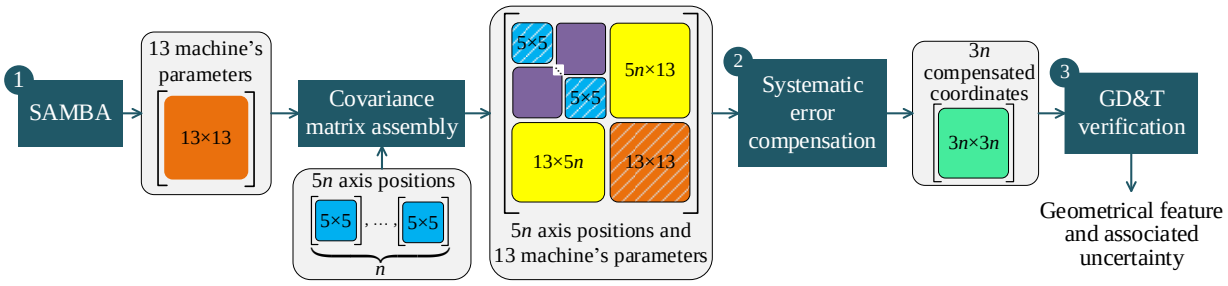

Figure 6-1: Data flow for the on-machine assessment of a geometric feature from a point set consisting of n probed points. The matrices in colour schematically represent the covariance matrices associated with the input and output quantities of the different steps.

6.3.1 Adaptive Monte Carlo method

The main idea of an MCM is to evaluate measurement function $\boldsymbol{Y} = f(\boldsymbol{X})$, where $f: \mathbb{R}^N \to \mathbb{R}^m$, for a population of estimates $\boldsymbol{x} = [x_1, \ldots, x_N]^{\mathrm{T}}$ of the vector of input quantities $\boldsymbol{X} = [X_1, \ldots, X_N]^{\mathrm{T}}$ and to build a population of estimates $\boldsymbol{y} = [y_1, \ldots, y_m]^{\mathrm{T}}$ of the vector of output quantities $\boldsymbol{Y} = [Y_1, \ldots, Y_m]^{\mathrm{T}}$. A covariance simulator (Figure 6-1) provides the adaptive MCM with the information needed to generate the population of input quantities. In the current application of MCM, the on-

machine measurement function receives the axis positions recorded for a probed point set along with 13 machine parameters (Figure 6-5a and), builds the machine's kinematic model through a chain of homogenous transformation matrices, and then returns the compensated position of the probed point set in the workpiece Cartesian frame (Figure 6-2c). Assuming an on-machine measurement of a point set of size n with a five-axis machine tool, the number of inputs and outputs of the measurement function are N=5n+13 and m=3n, respectively. Should the geometric feature outlined by the point set be the output of interest, the measurement function also calls the GD&T verifier (step 3 in Figure 6-1), which reduces the number of outputs from m=3n to one (a scalar quantity of the concerned geometric feature such as length, diameter, sphericity, etc.).

Table 6-1: Geometric errors of the machine tool according to the nomenclature specified in [102]. The first subscript is the nature of the error, the numeral 0 (zero) as the middle subscript indicates that it is an axis position or orientation error (not an error motion) and the third subscript is the axis of motion with this error.

	Symbol	Description
1	E_{A0B}	out-of-squareness error of axis B relative to axis Z
2	E_{C0B}	out-of-squareness error of axis B relative to axis X
3	E_{X0C}	distance between axes B and C
4	E_{A0C}	out-of-squareness error of axis C relative to axis B
5	E_{B0C}	out-of-squareness error of axis C relative to axis X
6	E_{B0Z}	out-of-squareness error of axis Z relative to axis X
7	E_{A0Y}	out-of-squareness error of axis Y relative to axis Z
8	E_{C0Y}	out-of-squareness error of axis Y relative to axis X
9	E_{XX1}	linear term (slope) of the linear positioning error of axis X
10	E_{YY1}	linear term (slope) of the linear positioning error of axis Y
11	E_{ZZ1}	linear term (slope) of the linear positioning error of axis Z
12	E_{Y0S}	distance between the spindle axis and axis C along axis Y
13	E_{X0S}	distance between the spindle axis and axis B along axis X

The MCM simulator (Figure 6-2b) draws at random M input vectors from a normal joint probability distribution function (joint PDF) described by the mean and the covariance matrix of $\boldsymbol{X}$ (the multicoloured matrix in Figure 6-1) and stores them in matrix $\boldsymbol{G_X}$ of dimension $N \times M$ [50]. The

output samples, stored in matrix $\boldsymbol{G_Y}$ of dimension $m \times M$, encode the knowledge of possible values of output vector $\boldsymbol{Y}$ that, among other statistical measures, releases the standard uncertainty $\boldsymbol{u_y}$ associated with $\boldsymbol{y}$, a best estimate for $\boldsymbol{Y}$. This best estimate is obtainable by averaging over the M estimates of output quantities. Standard uncertainty $\boldsymbol{u_y}$ is the square root of the diagonal elements of covariance matrix $\boldsymbol{U_y}$ (the green matrix in Figure 6-1) associated with estimate $\boldsymbol{y}$, given by [50]:

$$\boldsymbol{U_y} = \frac{1}{M-1}\boldsymbol{G'_Y}\,(\boldsymbol{G'_Y})^{\mathrm{T}}, \qquad \boldsymbol{G'_Y} = \boldsymbol{G_Y} - \boldsymbol{y}(\mathbf{1}_{M\times 1})^{\mathrm{T}} \tag{6-1}$$

where $\mathbf{1}_{M\times 1}$ is a column vector of ones of length M.

Concerning the convergence of MCM, Supplement 2 to the GUM [50] specifies the details of an adaptive MCM, where after each sequence h (including M=10^4 trials), the simulator records estimates $\boldsymbol{y}$, standard uncertainties $\boldsymbol{u_y}$, maximum eigenvalue $\lambda_{\max}$ of the associated correlation coefficient matrix, and coverage factor k_p (corresponding to coverage probability p). After the tenth sequence (h=10), the adaptive MCM calculates the standard deviations of these metrics out of the h=10 accumulated values and compares them with stipulated numerical tolerances. If these standard deviations are larger than the numerical tolerances, the adaptive MCM executes one more sequence and this procedure continues until the convergence holds. More details about the used adaptive MCM can be found in [115].

6.3.2 Covariance of input quantities

The multivariate sample generator of an MCM process builds a population of possible values of input vector $\boldsymbol{X}$. Although random, the input quantities drawn at each trial satisfy certain constraints in terms of magnitude and correlation according to a joint PDF (usually normal) described by a mean and a covariance matrix that should reliably define the random behaviour of the probed positions and the machine parameters as well as their correlation. However, quantification of such a covariance matrix poses a significant challenge because the on-machine probing and the identification of the machine parameters are usually obtained at different times and the machine parameters are presumed to remain valid for compensation purposes during a certain period.

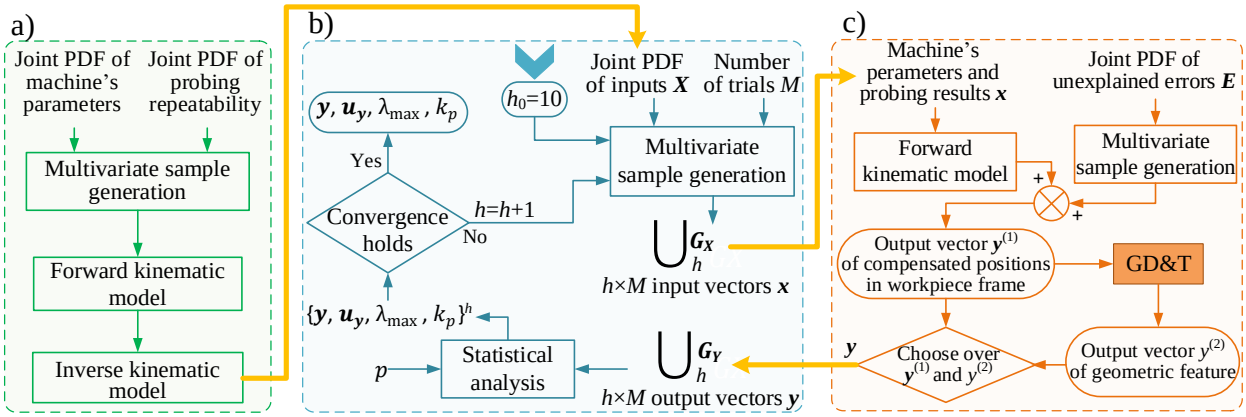

Figure 6-2: Data flow of a) the covariance simulator for input quantities, which provides a full covariance matrix for b) the adaptive Monte Carlo method that evaluates a large sample of input quantities through c) the on-machine measurement function.

The short-term repeatability analysis of the machine tool used in this project reveals an insignificant standard deviation (< 1 µm) for the single-point on-machine measurements [103]. This short-term repeatability (the blue matrices in Figure 6-1) is obtained through replicated on-machine measurements over a time span of 10 min, while the machine's state remains almost unchanged. Therefore, it excludes the day-to-day (long-term) probing repeatability caused by the machine's variation, mostly due to thermal drift and changes in its working conditions. To estimate the long-term variations of the probed coordinates and simultaneously, to quantify their correlations among themselves and with the machine parameters, the variations in the latter effect can be thought of as the cause for the long-term variations of the probed coordinates. In other words, having a quantified picture of the machine's day-to-day fluctuations allows estimating the long-term variations of the on-machine probed points as well as the corresponding correlations.

Figure 6-3 shows the procedure of the covariance simulation for the input quantities. We assume that random variable $\boldsymbol{\Gamma}$ (5×1) describes the axis positions recorded in the long-term replications (long-term repeatability) of the on-machine measurement of a certain target point by a five-axis machine tool. The probe tip touches the target point and the machine reports axis positions $\boldsymbol{\varphi}$ (5×1). A repeatability model [103] gives repeatability covariance matrix $\boldsymbol{v}$ associated with probing results

$\boldsymbol{\varphi}$. Let us assume random variable $\boldsymbol{\Phi}$ (5×1) describes the short-term variations of the probed axis positions and is distributed as:

$$\boldsymbol{\Phi} \sim \mathcal{N}(\boldsymbol{\varphi}, \boldsymbol{v}) \qquad 6\text{-}2$$

where $\mathcal{N}(\boldsymbol{\varphi}, \boldsymbol{v})$ is a multivariate normal distribution with mean and covariance of $\boldsymbol{\varphi}$ and $\boldsymbol{v}$, respectively. The SAMBA method identifies the current machine parameters $\boldsymbol{\delta}$ (13×1). Compensating (evaluating) random variable $\boldsymbol{\Phi}$ with the machine's forward kinematic model f for the current machine parameters $\boldsymbol{\delta}$ yields $\boldsymbol{\Psi} = f(\boldsymbol{\Phi}, \boldsymbol{\delta})$, where $\boldsymbol{\Psi}$ (3×1) is the random variable describing the compensated positions in the workpiece frame. Depending on measurement function f, $\boldsymbol{\Psi}$ can have different types of distribution. Here, we assume a normal multivariate distribution with mean and covariance of $\boldsymbol{\psi}$ and $\boldsymbol{w}$, respectively, describes $\boldsymbol{\Psi}$:

$$\boldsymbol{\Psi} \sim \mathcal{N}(\boldsymbol{\psi}, \boldsymbol{w}) \qquad 6\text{-}3$$

Day-to-day monitoring (once a day over a long term, say two weeks) of the machine tool estimates the long-term variations of the machine's status, described by random variable $\boldsymbol{\Delta}$, distributed as:

$$\boldsymbol{\Delta} \sim \mathcal{N}(\boldsymbol{\delta}, \boldsymbol{\sigma}) \qquad 6\text{-}4$$

where $\mathcal{N}(\boldsymbol{\delta}, \boldsymbol{\sigma})$ is a multivariate normal distribution with mean $\boldsymbol{\delta}$ and covariance $\boldsymbol{\sigma}$. The SAMBA method identifies $\boldsymbol{\delta}$ (the 13 machine parameters) through a multiple regression using the least-square approach. In this indirect method, a sample consisting of 327 observations (raw machine measurements of the center of the balls at 109 positions) and the length of a calibrated bar are used to approximate the machine parameters [115]. This sample seems large enough so that the normality assumption (Eq. 6-4) holds as a consequence of the Central Limit Theorem [116]. To achieve maximum compensation for systemic effects, it is essential that the machine parameters incorporated in the measurement function represent the current status of the machine. Therefore, the distribution given by Eq. 6-4 should be valid in terms of both the mean and the covariance. If the day-to-day monitoring results of the machine seem outdated, although its working conditions and environment have not significantly changed, one can presume the covariance $\boldsymbol{\sigma}$ (shape) of this

distribution to be valid and only update its mean $\boldsymbol{\delta}$ (centre) by conducting a new error identification test.

Q random draws $\boldsymbol{\delta}^q$ $(q = 1, \dots, Q)$ from Eq. 6-4 simulates this number of machine tools, each representing the machine's status in the corresponding section of the period of the day-to-day identification of the machine's errors. Now, we assume each simulated machine tool (defined by $\boldsymbol{\delta}^q$) conducts a short-term pseudo-repeatability test on the same target point whose location on the machine's table remains unchanged. This gives Q distributions of the short-term probing repeatability, where random variable $\boldsymbol{\Phi}^q$ denotes the recorded positions for the five axes of the machine over the q^{th} pseudo-repeatability test:

$$\boldsymbol{\Phi}^q \sim \mathcal{N}(\boldsymbol{\varphi}^q, \boldsymbol{v}^q) \tag{6-5}$$

in which $\mathcal{N}(\boldsymbol{\varphi}^q, \boldsymbol{v}^q)$ is a multivariate normal distribution with mean and covariance of $\boldsymbol{\varphi}^q$ and $\boldsymbol{v}^q$, respectively. Because the short-term repeatability test is repeatable [103], $\boldsymbol{v}^q \approx \boldsymbol{v}$. Then,

$$\boldsymbol{\Phi}^q \sim \mathcal{N}(\boldsymbol{\varphi}^q, \boldsymbol{v}) \tag{6-6}$$

These Q distributions of $\boldsymbol{\Phi}^q$ give snapshots of the long-term variations of axis positions (described by $\boldsymbol{\Gamma}$), taken Q times over the considered long time span. As a result, one random draw from each of these distributions gives a sample of size Q, resembling replicated probing results collected over the long-term. In other words, the drawn sample approximates the axis positions obtainable on a day-to-day basis (conforming to the SAMBA routine that identifies the machine's status $\boldsymbol{\Delta}$), as if the target point is probed once a day over the long-term. Therefore, to evaluate $\boldsymbol{\Gamma}$, it suffices to quantify $\boldsymbol{\Phi}^q$ (Eq. 6-6) and do the Q random draws.

Since the target point's location on the machine table remains unchanged, it is expected that the compensation of the acquired data during any of the Q pseudo-experiment results in the same compensated positions, described by $\boldsymbol{\Psi}$ in Eq. 6-3. Then, evaluating $\boldsymbol{\Psi}$ through the inverse kinematic model f^{-1} of each erroneous machine described with $\boldsymbol{\delta}^q$ quantifies random variable $\boldsymbol{\Phi}^q$, the five pseudo-axis positions of the machine:

$$\boldsymbol{\Phi}^q = f^{-1}(\boldsymbol{\Psi}, \boldsymbol{\delta}^q) \tag{6-7}$$

in which $\boldsymbol{\Psi}$ is distributed as Eq. 6-3.

One random draw from each of the Q distributions given by Eq. 6-7 gives a sample of Q probing results recorded in the long-term. Therefore, this approximates to sampling $\boldsymbol{\gamma}^q$ (q=1, … , Q) from the distribution of $\boldsymbol{\Gamma}$. Choosing an adequately large value for Q provides a population of estimates for $\boldsymbol{\Gamma}$. Since according to Eq. 6-7, $\boldsymbol{\Phi}^q$ (and consequently $\boldsymbol{\Gamma}$) varies with the machine's status $\boldsymbol{\delta}^q$, combining the population estimated for $\boldsymbol{\Gamma}$ with that of the machine parameters $\boldsymbol{\Delta}$ (composed of $\boldsymbol{\delta}^q$) estimates the joint distribution of all the input quantities of the on-machine measurement function. The q^{th} member of the assembled population is the concatenation of $\boldsymbol{\gamma}^q$ and $\boldsymbol{\delta}^q$.

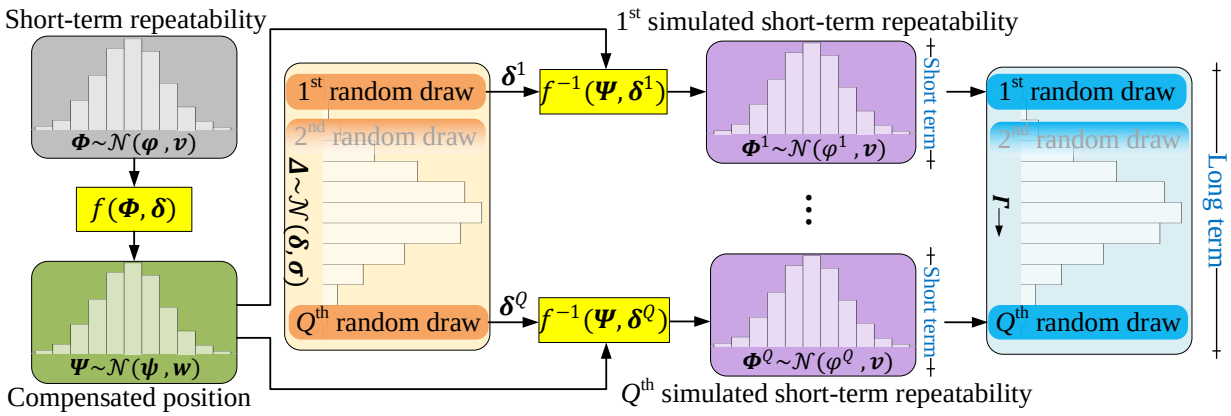

Figure 6-3: Data flow for the simulation of the covariance matrix of the input quantities consisting of probed axis positions $\boldsymbol{\Gamma}$ and machine parameters $\boldsymbol{\Delta}$. The process includes calculating compensated positions $\boldsymbol{\Psi}$ through forward kinematic model f with an estimate of current machine parameters $\boldsymbol{\delta}$, then simulating long-term repeatability of on-machine measurement by evaluating the compensated positions $\boldsymbol{\Psi}$ through the inverse kinematic model f^{-1} with a sample of machine parameters $\boldsymbol{\delta}^q$ $(q = 1, \dots, Q)$. For illustrative purposes, the distributions are univariate.

A covariance simulator conducts these steps and estimates the long-term random behaviour of probing results based on the corresponding variations of the machine tool, as if the probing task has lasted many days. For an on-machine probed point set $\boldsymbol{\varphi}$ of size n, like in measuring the diameter of a hole by probing n points around it, the repeatability model [103] first provides the

short-term covariance matrices $\boldsymbol{v}$ of dimension 5×5 (denoted by the blue matrices in Figure 6-1). Then, according to Eq. 6-2, the covariance simulator generates a population (Population I of size Q) of point sets, i.e. of the vectors ($5n$×1) of the probed axis positions, whose mean equals probing results $\boldsymbol{\varphi}$. Then, the machine's forward kinematic model receives each member (point set) of Population I and calculates the corresponding compensated positions in the workpiece frame through the current estimated machine parameters $\boldsymbol{\delta}$. The resulting population (Population II) consists of the possible actual positions $\boldsymbol{\Psi}$ of the probed point set in the workpiece frame. Monitoring the machine parameters over 15 days (once a day) gives an estimate of their joint PDF [115]. To update this joint distribution, it is centred at the current parameters of the machine $\boldsymbol{\delta}$ without affecting its covariance, given that the machine's functionality and environmental condition have barely changed. The covariance matrix $\boldsymbol{\sigma}$ (the 13×13 orange matrix in Figure 6-1) defines the shape of this distribution [115]. The covariance simulator receives this joint PDF and generates a population (Population III of size Q) of the estimates for the machine parameters $\boldsymbol{\delta}^q$ ($q = 1, \dots, Q$), where each vector (13×1) represents a different simulated machine tool. Then, the inverse kinematic models of the simulated erroneous machines generate the probing data (axis coordinates) that each instance of the machine parameters ,included in Population III, would have produced for each compensated point set stored in Population II. This generates Population IV (of size Q), consisting of the simulated positions of the machine's axes obtainable in a long-term replicated probing task, conforming to the day-to-day variations of the machine's status over 15 days. Combining populations III and IV gives the joint PDF and then the corresponding covariance matrix of dimension ($5n$+13)×($5n$+13) for input vector $\boldsymbol{X}$ of the on-machine measurement function, suitable to initiate the MCM procedure (Figure 6-2b). The multicoloured matrix in Figure 6-1 denotes this covariance matrix. Since the positions of the machine's rotary axes (B and C) remain unchanged during the probing of a single point, they appear as constant values so that the corresponding elements in the covariance matrix are zero.

An example of the single-point probing on a reduced single-axis machine tool can illustrate the covariance simulation. In this example, the only machine parameter is the linear term (slope) of the positioning error, given as δ=-50.0 µm/m with a variance of σ=100 µm^2/m^2 obtained over a day-to-day error identification. Let us assume random variables Φ and Ψ describe the probed axis position and the compensated position, respectively, and Γ denotes the long-term variations of the

recorded axis position. This machine probes one end of a gauge block and reports a hypothetical value of φ=100.000 mm with a repeatability of v=1.0 μm^2 in terms of variance. A multivariate sample generator produces Population I (of size 10^4) of axis position Φ based on normal distribution (Figure 6-4):

$$\Phi \sim \mathcal{N}(\varphi, v) \tag{6-8}$$

Population II includes compensated position Ψ, evaluated through the measurement function (Figure 6-4):

$$\Psi = f(\Phi, \delta) = \Phi(1 + \delta) \tag{6-9}$$

This population shares the variance of Population I but its mean is $\psi = \varphi(1 + \delta)$=99.995 mm. Then, the multivariate sample generator creates Population III (of size 10^4) of the machine error parameters Δ according to normal distribution (Figure 6-4):

$$\Delta \sim \mathcal{N}(\delta, \sigma) \tag{6-10}$$

This population includes 10^4 simulated machine tools, varying in the long-term. Since the gauge block preserves its geometry and location on the machine table, each member of this population suffices to estimate the probing result obtainable in the short-term by the simulated machine it represents. To do so, evaluating the q^{th} ($q = 1, \dots, 10^4$) compensated position (ψ^q) stored in Population II through the inverse kinematic model formed by the q^{th} simulated machine (δ^q) included in Population III estimates the corresponding axis position in a long-term replicated probing task (γ^q). This creates Population IV of Γ (Figure 6-4):

$$\gamma^q = f^{-1}(\psi^q, \delta^q) = \frac{\psi^q}{(1 + \delta^q)} \tag{6-11}$$

Although Eq. 6-7 suggests processing the whole members of Population II through the inverse kinematic model with δ^q, doing so only for one member of this population suffices as long as Q is adequately large.

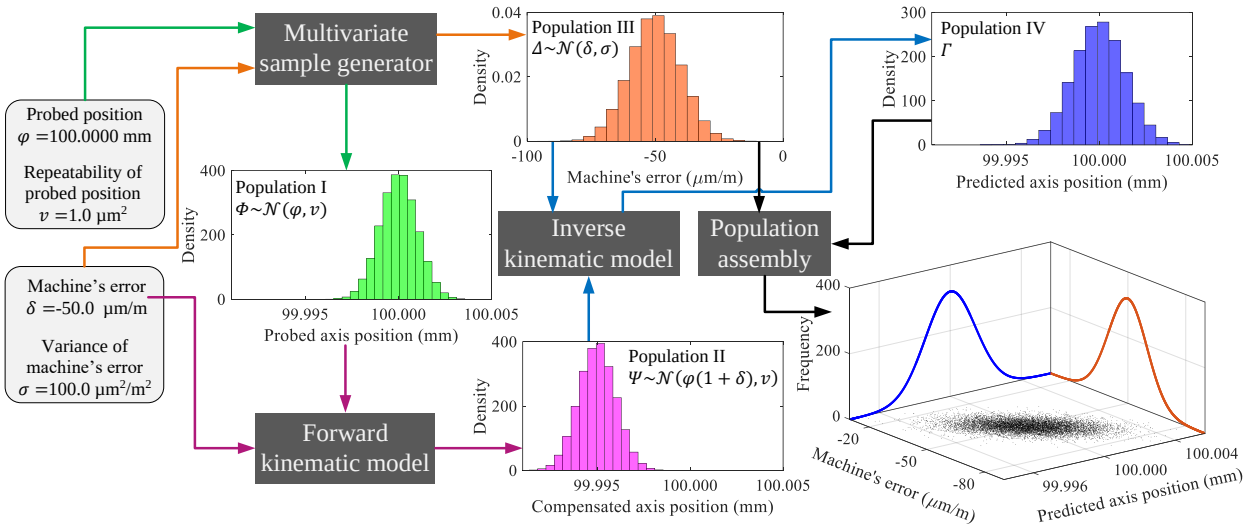

Figure 6-4: The data flow of the covariance simulation for a single-point probing on a single-axis (axis Φ) machine tool with a positioning error of δ. The green distribution describes the population of short-term repeatability of probed positions Φ (Population I). The purple histogram represents the population of corresponding compensated positions Ψ (Population II). The orange distribution describes the population of machine parameter Δ varying in the long-term (Population III). Evaluating Population II through the inverse kinematic model with population III gives the blue histogram representing the population of long-term repeatability of probed positions Γ (Population IV). Combining Populations III and IV provides a joint distribution for input random variables Γ and Δ. Analyzing the combined population reveals a correlation coefficient of -0.7, a high interdependence that is evident in the orientation of 2,000 random points drawn from the joint distribution.

Population IV encodes the long-term variations of the recorded axis position while probing the same target point. Assembling this population (variations of the probed axis positions in the long-term Γ) and Population III (variations of the machine parameter in the long-term Δ) gives the bivariate joint PDF of these variables, where these populations define the marginal distributions for the axis position and the machine's error, respectively. The mean and the covariance matrices of the joint PDF are:

$$\begin{bmatrix}\gamma\\ \delta\end{bmatrix} = \begin{bmatrix}100\ \text{mm}\\ -50.0\ \mu\text{m}/m\end{bmatrix},\quad \begin{bmatrix}\text{cov}(\Gamma,\Gamma) & \text{cov}(\Gamma,\Delta)\\ \text{cov}(\Delta,\Gamma) & \text{cov}(\Delta,\Delta)\end{bmatrix} = \begin{bmatrix}2.0\times10^{-6} & -1.0\times10^{-2}\\ -1.0\times10^{-2} & 1.0\times10^{2}\end{bmatrix} \qquad 6\text{-}12$$

The marginal distribution for the axis position shares the mean of Population I, i.e. γ=φ=100.000 mm, although its variance increases from 1.0 to 2.0 μm^2, through the propagation of uncertainty (Figure 6-4). This joint PDF results in a standard uncertainty of 2.2 μm for the compensated axis position ψ=99.995 mm, whereas relying only on the probing repeatability (the short-term random behaviour of the probed position) and neglecting the inputs' correlation yield 1.4 μm. As Figure 6-4 shows, the input quantities are strongly correlated ($\mathrm{corr}(\Gamma, \Delta)$=-0.7). The negative correlation confirms that a smaller machine's error causes a larger probed axis position since the machine's axis has contracted (the slope of the machine's positioning error is negative). Including such a causal relationship between the two input quantities in the uncertainty estimation becomes possible only through the covariance analysis. Otherwise, as this example demonstrates, the assumption of independence of inputs causes an inaccurate estimate for their random behaviour.

6.3.3 Volumetric errors unexplained by SAMBA

Precise compensation for systematic errors is a prerequisite for uncertainty evaluation. That is, the closer the output estimate to the true value of the measurand, the smaller the uncertainty interval to encompass it. In an ideal case, full compensation for systematic errors places the centre of an uncertainty interval on the true value of the measurand, denoting no residual bias in the measurement result. In practice, however, the estimated uncertainty interval has to be large enough, due to the residual systematic effects, so that it encompasses the true value of the measurand. These residual systematic errors are those unexplained by the estimated machine parameters due to limitations of the error identification model. To consider these effects, the uncertainty estimator includes a vector of unexplained volumetric errors $\boldsymbol{E}$:

$$\boldsymbol{E} = [\boldsymbol{e_1}, \dots, \boldsymbol{e_n}]^{\mathrm{T}} \qquad 6\text{-}13$$

where $\boldsymbol{e_s} = [e_{\mathrm{X}}, e_{\mathrm{Y}}, e_{\mathrm{Z}}]^{\mathrm{T}}$ $(s = 1, \dots, n)$, is the unexplained volumetric error associated with the s^{th} point of a point set of size n. Unexplained volumetric error $\boldsymbol{E}$ is added to the compensated positions (in the workpiece frame) of each probed point set (Figure 6-2c):

$$\boldsymbol{y^{(1)}} = \boldsymbol{y} + \boldsymbol{E} \qquad 6\text{-}14$$

At each trial of the adaptive MCM, the uncertainty estimator creates $\boldsymbol{E}$ through n random draws from the joint PDF of $\boldsymbol{e}$. Calculating the unexplained volumetric errors for 92 positions probed on the machine during the SAMBA procedure gives the mean and the covariance matrix of $\boldsymbol{e}$:

$$\bar{\boldsymbol{e}} \approx \mathbf{0}\,, \quad \mathrm{cov}(\boldsymbol{e}) = \begin{bmatrix} 4.5 & -1.7 & -22.0 \\ -1.7 & 6.6 & 0.7 \\ -22.0 & 0.7 & 5.8 \end{bmatrix} \times 10^{-5}\ \mathrm{mm}^2 \qquad 6\text{-}15$$

These 92 points take no part in the SAMBA probing data used for the error identification with this method.

6.4 Experimental verification

The on-machine measurement of calibrated workpieces allows for the evaluation of the proposed uncertainty estimator. For this purpose, a Mitsui Seiki HU40-T five-axis horizontal machining centre (Figure 6-5a) equipped with a Renishaw® MP 700 touch-trigger probe measures a gauge block's length and a precision ball's diameter and sphericity. The nominal length of the probe's stylus is 150 mm. All probing is conducted using the linear axes whereas different positions of rotary axes B and C re-locate the workpiece in the work envelope. Each measurement task of the gauge block (Figure 6-5b) with a nominal length of 500 mm and an expanded uncertainty of 0.3 µm (indicated at a temperature of 20°C) includes probing one point on each end's centre (denoted by numbers 1 and 2 in Figure 6-5b), providing a set of two points (n=2). First, for the B-axis position of zero and C-axis positions 135°, 165°, …, and 285°, and then for nine random positions of rotary axes B and C, the machine probes Side A of the gauge block, resulting in a group of 15 data (including 30 probed points). The same procedure is repeated (with different nine random positions for the rotary axes) for Side B of the gauge block to acquire another group of 15 data. One single draw from each group provides a point set of size 2 whose distance gives the gauge's length plus the effective diameter of the probe's stylus tip. To compensate for the latter, while the B- and C- axis positions are zero, a five-point probing of a precision sphere of known diameter is conducted. The effective diameter of the probe's stylus tip is 5.925 mm and because of the relatively small size of the used precision sphere and since the rotary axes are not involved in the five-point probing, the uncertainty associated with the stylus tip is assumed negligible. The calibrated diameter and sphericity of the sphere are 19.05 mm and 0.4 µm with associated expanded

uncertainties of 0.5 and 0.1 µm, respectively (indicated at a temperature of 20°C). The whole measurement process of the gauge block lasts about 15 min.

The second experimental validation consists in measuring the diameter and the sphericity of the same precision sphere (Figure 6-5c) by probing 25 points (n=25) on its surface (Figure 6-5d) [117]. Ten point sets are collected at ten random positions of axes B and C. For each point set, the least-square sphere estimates the diameter, and the difference between the maximum and the minimum fitting residuals indicates the sphericity. The sphere measurements take about 74 min. An infrared camera constantly captures the temperature of the calibrated parts and reports a variation between 21.6 and 22.1 °C with an average temperature of 21.7 °C. To have up-to-date knowledge of the machine's state, the SAMBA method identifies the machine parameters twice, once before and once after the two experiments, whose average introduces the vector of the machine parameters (13×1) to the on-machine measurement function.

Let us assume that η denotes the possible values of the measurand (gauge's length, sphere's diameter or its sphericity) and that this variable is normally distributed with mean y_{cal} (the calibrated value of the measurand) and standard deviation u_{cal} (the standard uncertainty associated with the calibrated value). This distribution (Figure 6-5e) includes the available benchmark of the true value of the measurand. The probability that expanded uncertainty interval $y \pm U_y$ associated with a geometric feature estimate (obtained through the proposed methodology for a stipulated coverage factor) encompasses the calibrated value of the measurand y_{cal} is the area bounded within this interval and under the distribution curve of the calibrated value (Figure 6-5e):

$$p = \int_{y-U_y}^{y+U_y} \frac{1}{u_{\text{cal}}\sqrt{2\pi}} e^{-\frac{1}{2}\left(\frac{\eta - y_{\text{cal}}}{u_{\text{cal}}}\right)^2} d\eta \qquad 6\text{-}16$$

Ideally, this integral yields the theoretical coverage probability (for example 95% for a coverage factor of 2). For each calibrated workpiece, the calibrated value $y_{\text{cal,20°C}}$ and its standard uncertainty $u_{\text{cal,20°C}}$ (inspected at 20.0 °C according to the workpieces' specifications), the temperature difference of the workpiece ΔT compared with the calibration process and its uncertainty $u_{\Delta T}$, and the workpiece's thermal expansion α and its uncertainty u_α are the factors

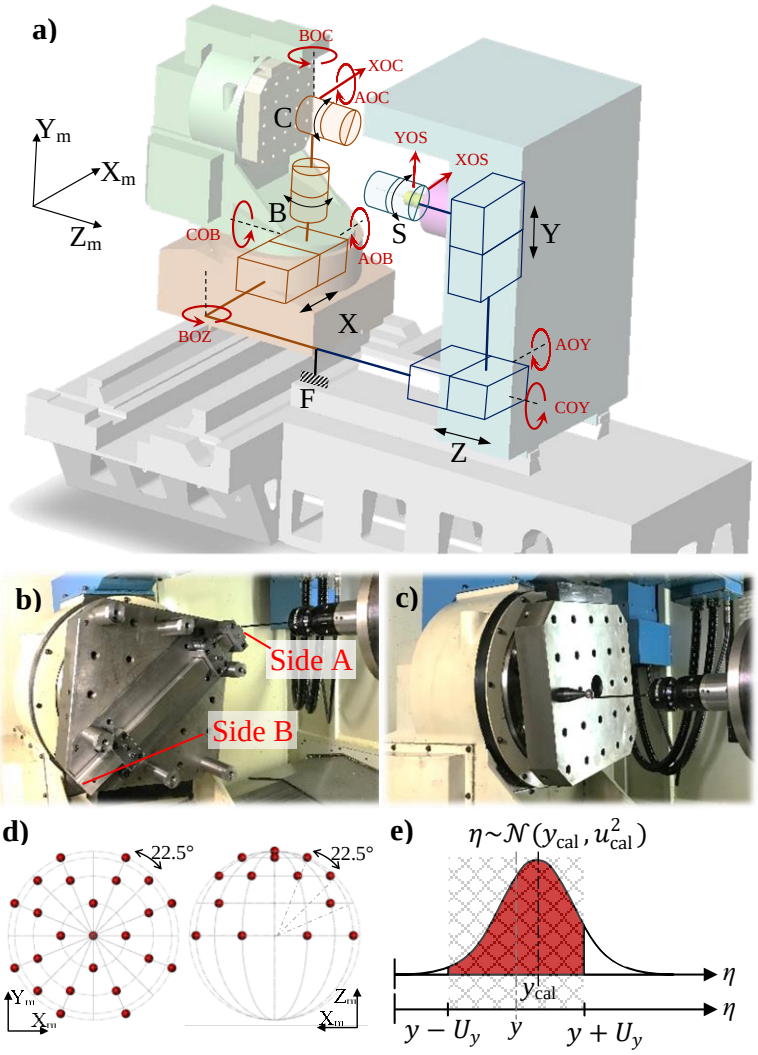

Figure 6-5: The experimental procedure where a) a Mitsui Seiki HU40-T five-axis horizontal machining centre (shown with its axis location errors) measures b) a gauge block and c) a precision sphere. Also shown are d) the target points probed on the precision sphere and e) the calculation of the coverage probability in the experimental verification where the red area is the coverage probability provided by the expanded uncertainty interval $y \pm U_y$ for measurand η.

defining mean y_{cal} and the standard deviation u_{cal} of this distribution. The linear expansion equation gives y_{cal}:

$$y_{\text{cal}} = y_{\text{cal},20^\circ\text{C}}(1 + \alpha\Delta T) \qquad 6\text{-}17$$

and the law of propagation of uncertainty estimates standard uncertainty u_{cal}

$$u_{\text{cal}} = \sqrt{\left(\frac{\partial y_{\text{cal}}}{\partial y_{\text{cal,20°C}}}\right)^2 u_{\text{cal,20°C}}^2 + \left(\frac{\partial y_{\text{cal}}}{\partial \alpha}\right)^2 u_{\alpha}^2 + \left(\frac{\partial y_{\text{cal}}}{\partial \Delta T}\right)^2 u_{\Delta T}^2} \quad \text{6-18}$$

which yields

$$u_{\text{cal}} = \sqrt{(1+\alpha\Delta T)^2\, u_{\text{cal,20°C}}^2 + \left(y_{\text{cal,20°C}}\Delta T\right)^2 u_{\alpha}^2 + \left(y_{\text{cal,20°C}}\,\alpha\right)^2 u_{\Delta T}^2} \quad \text{6-19}$$

According to the calibration specifications, $y_{\text{cal,20°C}}$ and $u_{\text{cal,20°C}}$ (for a coverage factor of 2) are 500.0000 mm and 0.2 µm for the gauge's length, and 19.0500 mm and 0.3 µm for the sphere's diameter, respectively. Thermal expansion coefficient α and its uncertainty u_{α} are 10.80×10^{-6} and 0.15×10^{-6} °C^{-1}, respectively. Based on the average temperature (21.75°C) captured during the on-machine measurements, the temperature difference ΔT is 1.75°C and its uncertainty is derived from the device's resolution (0.01°C) as $0.005/\sqrt{3}$=0.003°C. Substituting these values in Eqs. 6-17 and 6-19 returns y_{cal} and u_{cal} as 500.0095 mm and 0.2 µm for the gauge's length, and 19.0504 mm and 0.3 µm for the diameter of the precision sphere, respectively. The thermal effects on the calibrated sphericity and its uncertainty are assumed negligible.

6.5 Results and discussion

6.5.1 Gauge block

The two data groups (each of size 15), collected during the gauge block test, provide 15^2 different point sets of size 2, denoting 225 bipoint samples of length estimates. Simple probing tasks, such as length measurement, usually complete without moving the rotary axes, i.e. the two points picked at the part's ends share the same rotary-axis positions. In this experiment, however, the position of the workpiece frame, relative to the machine frame, is different for each single-point probing, except for the six lengths measured with the B-axis at its zero position and with C-axis positions of 135°, 165°, …, and 285°. This challenges the compensation capacity of the on-machine

measurement function and well represents the diversity of possible data acquisitions to measure linear feature-of-size on a part.

For each bipoint, the uncertainty estimator (Figure 6-2b) receives the vector of input estimates $\boldsymbol{x}$ of dimension 23×1 (including 2x5=10 axis positions comprising the bipoint and 13 machine parameters) along with its simulated (Figure 6-2a) covariance matrix $\boldsymbol{U_x}$ of dimension 23×23. To obtain this matrix, following the procedure given in section 2-2, a multivariate random generator first creates Population I (10×10^4) based on the short-term repeatability of each point. Evaluating this population with the forward kinematic model generates Population II (6×10^4) of compensated positions for each bipoint. The multivariate random generator creates Population III (13×10^4) based on the joint PDF of the machine parameters. Then, evaluating each member of Populations II through the inverse kinematic model with one and only one member of Population III gives population IV (10×10^4) encoding simulated short-term repeatability. Combining Populations III and IV estimates the population of all input quantities (23×10^4) from which full covariance matrix $\boldsymbol{U_x}$ (23×23) is obtainable. By evaluating M=10^4 generated bipoints through the on-machine measurement function (Figure 6-2c), it then creates a population of size M of vectors $\boldsymbol{y^{(1)}}$ (6×1), whose members are the possible actual positions of the point set in the workpiece frame. Then, the GD&T unit calculates the gauge's length corresponding to each compensated point set, resulting in a population of scalar output $y^{(2)}$ of compensated length l_{c}. A statistical analysis of this population provides best estimate y of the gauge's length and the associated expanded uncertainty U_y (for a coverage factor of 2). Repeating this procedure for the 225 point sets gives this number of expanded uncertainty intervals $y \pm U_y$. The estimated expanded uncertainties vary between 17.5 and 25.5 µm, with an average of 19.2 µm. Then, the integral specified by Eq. 6-16 gives 225 coverage probabilities provided by the estimated intervals, over which averaging yields an average coverage probability of $\bar{p}$ =90%.

Figure 6-6a shows the compensated errors e_{c}versus the measurement errors e_{m}, where

$$e_{\mathrm{c}} = l_{\mathrm{c}} - y_{\mathrm{cal}} \text{ and } e_{\mathrm{m}} = l_{\mathrm{m}} - y_{\mathrm{cal}} \qquad 6\text{-}20$$

in which l_{m} is the gauge's length measured from the probing data before compensation. Also shown is the average expanded uncertainty zone [-19.2 , +19.2] µm. The 203 green points represent the

compensated points whose expanded uncertainty intervals overlaps with that of the calibrated length. Although after compensation for systematic errors the data is less scattered along the vertical axis (compensation error), the residual volumetric errors of an imperfect compensation prevent it from lying on the zero horizontal line. Figure 6-6b shows 20 random (out of 225) samples of the probed (before error compensation) and compensated gauge's lengths compared with the calibrated value. In some cases, such as samples 10 to 13, the compensation deteriorates the length estimate. However, the average length estimate enhances from 500.007 to 500.009 mm, while their standard deviations decrease from 0.031 to 0.011 mm.

Excluding the effect of unexplained volumetric errors (Eq. 6-14) from the uncertainty model can demonstrate the influence of this uncertainty budget. Without this factor, the average coverage probability in the gauge block measurement decreases to 39%, mainly caused by a considerable reduction in the evaluated expanded uncertainty. This reduction in coverage probability implies the unexplained offset between the calibrated length and the compensated measurement results, which could be reduced by adopting a more exhaustive error system in the forward kinematic model of the machine tool.

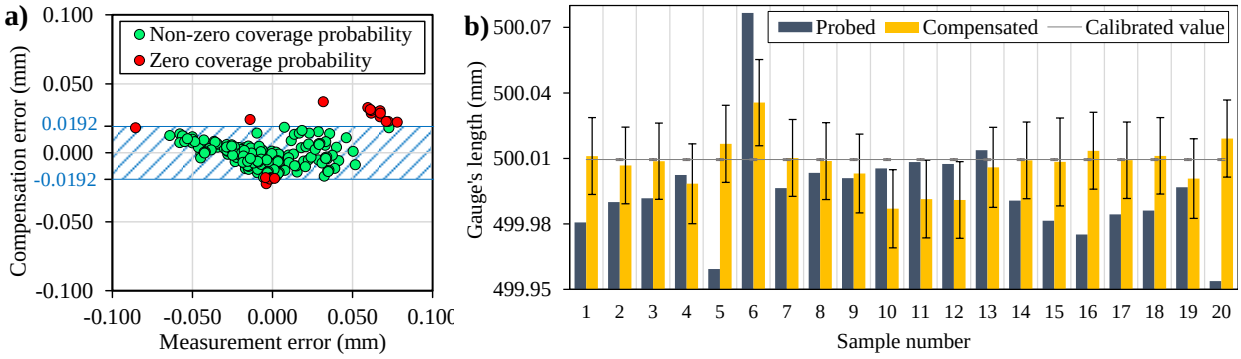

Figure 6-6: a) Compensation error versus measurement error for 225 measured gauge's lengths, where the average expanded uncertainty interval is denoted by the blue zone, and b) 20 (out of 225) samples of the probed (before compensation) and compensated gauge's lengths with the associated expanded uncertainty (shown by error bars) and the calibrated length.

6.5.2 Precision sphere

For small workpieces (relative to the machine's working volume) such as the precision sphere used in this work, the probed points share nearly the same axis positions. As a result, the machine's kinematic chain estimates similar volumetric error for the points, which mostly eliminates the need for error compensation for many geometric features, including diameter and sphericity. In other words, because of small distances within the points probed on such a relatively small sphere, the error compensation almost only translates the point set so that it barely changes the diameter of the sphere fitted in the least-square sense to the point set. This is evident for the 10 probed point sets (each including 25 measured points) whose calculated diameter and sphericity alter merely by 0.3 and 0.2 µm on average after the error compensation (Figure 6-7).

In the uncertainty evaluation of the sphere's geometric features (diameter and sphericity) indicated by each of the 10 collected point sets, the vector of input estimates $\boldsymbol{x}$ is of dimension 138×1 (including 125 axis positions, 5 for each of the 25 points measured, and 13 machine parameters). This vector along with covariance matrix $\boldsymbol{U_x}$ of dimension 138×138 result in a population of output vectors $\boldsymbol{y^{(1)}}$ (75×1) of compensated Cartesian coordinates of the point set in the workpiece frame. To simulate $\boldsymbol{U_x}$, the forward kinematic model evaluates Population I (125×10^4) and gives Population II (75×10^4) of compensated positions. Evaluating each member of the latter through the inverse kinematic model with only one member of Population III (13×10^4) yields Population IV (125×10^4). Combining Populations III and IV provides an assembled population (138×10^4) which provides full covariance matrix $\boldsymbol{U_x}$ (138×138).

The diameter and the sphericity of the least-square sphere outlined by each point set create two separate and independent populations of scalar output $y^{(2)}$, whose average and standard deviation give best estimate y and associated expanded uncertainty U_y for each feature. Repeating this procedure for each point set gives 10 best estimates for diameter (with an average of 19.0493 mm) and the associated expanded uncertainties (for a coverage factor of 2) which vary between 10.7 and 11.1 µm with an average of 10.9 µm (Figure 6-7a). The expanded uncertainties for the sphericity best estimates (with an average of 7.5 µm) vary between 10.9 and 11.2 µm, having an average of 11.1 µm (Figure 6-7b).

The diameter estimates (after compensation) differ from the calibrated diameter with a maximum of 2.0 µm and with an average of 1.1 µm so that all the 10 expanded uncertainty intervals encompass the calibrated diameter (Figure 6-7a). This demonstrates the machine's high accuracy in measuring the diameter of a small sphere. Although the sphericity estimates hold considerable offsets from the calibrated sphericity (up to twentyfold), each expanded uncertainty interval includes the calibrated value, owing to its relatively ample size that is even greater than the compensated sphericity (Figure 6-7b).

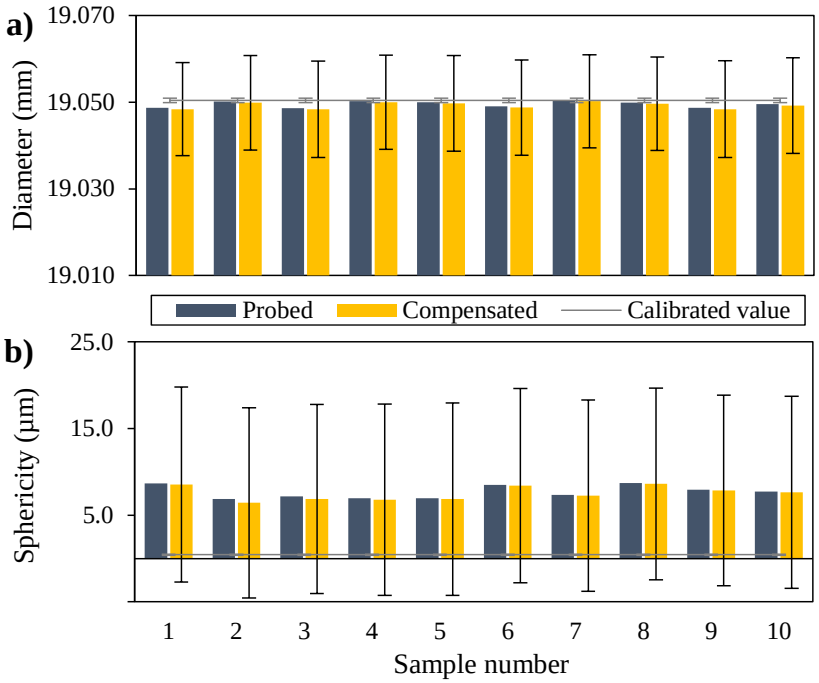

Figure 6-7: The compensated outputs with associated expanded uncertainties, the probed measurand (before compensation), and calibrated value of the measurand for a) the diameter and b) the sphericity of the precision sphere for each of 10 point sets.

For all the 10 point sets, although the expanded uncertainty intervals associated with the diameter and sphericity estimates comprise the corresponding calibrated value, validating the coverage probability provided by the uncertainty estimator requires a considerably larger number of point sets. For this purpose, first, k ($1 \leq k \leq 10$) out of the 10 point sets are pooled to build one set of size $25k$. Then, 25 random draws from the pool create one point set whose points are gathered

essentially from k random positions within the machine's working space. After drawing 200 point sets, which is an adequately large number for the validation purpose, the uncertainty estimator (Figure 6-2) quantifies best estimate and the associated standard uncertainty for the diameter and sphericity indicated by each point set. Then, for a coverage factor of 2, Eq. 6-16 gives the coverage probability offered by each expanded uncertainty.

Figure 6-8a shows the results for the diameter. The coverage probabilities calculated out of 200 point sets drawn at random from k pooled point sets collected experimentally on the precision sphere. Raising k increases the difficulty to compensate for systematic errors since this increases the diversity of the volumetric errors at the probed points. Drawing from the pool built by up to three point sets keeps the coverage probability of 100%. Although the average of the probed diameters (before the compensation for systematic effects) notably recedes from the calibrated value for k=2 and 3, the error compensation results in full coverage probabilities. By adding four more point sets to the pool (k=7), the coverage probability gradually drops to 95%, and then goes down to 90% by involving the eighth point set. Increasing the level of challenge more than this largely deteriorates the coverage probability so that it declines to about 60% after involving 9 and 10 point sets. The average of expanded uncertainties assigned to the point sets for each k varies between 8.9 and 9.7 µm (Figure 6-8a). After k=3, the effectiveness of error compensation gradually decreases so that after k=7 it even slightly worsens the average of probed diameters.

Figure 6-8b shows the results for the sphericity. The coverage probability immediately drops from 100% to 9% by pooling two point sets and it sinks to zero by further increasing k. For k=2, although the average of the probed sphericities (before the compensation for systematic effects) dramatically drifts away from the calibrated value and reaches 111.4 µm, it decreases almost twelvefold after the error compensation. However, such a considerable recovery is insufficient for keeping the coverage probability from the steep fall. For the full pool (including all the 10 point sets), the average sphericity estimate grows to 26.7 µm. The average of expanded uncertainties estimated for each k varies between 11.7 and 13.2 µm.

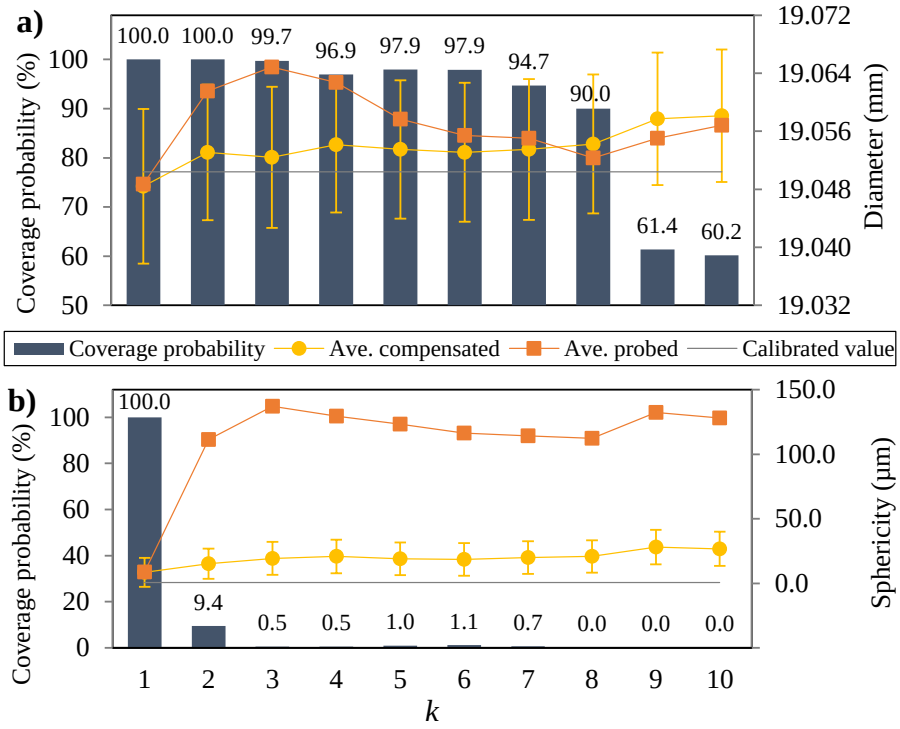

Figure 6-8: The coverage probability, the average of output estimates (after compensation) with the associated average expanded uncertainties, the average of probed measurands (before compensation), and the calibrated value of the measurand vs. the number of pooled point sets k, shown for a) the diameter and b) the sphericity of the precision sphere.

6.5.3 Verification of the uncertainty estimator

When expressed in mm, each compensated coordinate of a point set in the workpiece frame is regarded as having four significant decimal digits. Accordingly, the numerical tolerance for the MCM convergence is 0.05 µm [50]. The same numerical tolerance is considered for the geometric features. The MCM procedure (Figure 6-2) converges after h=10 sequences, including M=10^5 trails. For all the outputs, the numerical tolerance is larger than the standard deviation of ten values recorded for estimates $\boldsymbol{y}$, standard uncertainties $\boldsymbol{u}_{\boldsymbol{y}}$, maximum eigenvalue $\lambda_{\max}$ of the associated correlation coefficient matrix, and coverage factor k_p, which establishes the convergence of MCM. Table 6-2 lists these values for the six coordinates of a point set probed on the gauge block and for its length estimate.

Table 6-2: Standard deviation (Std.) of: estimates y, standard uncertainties u_y, maximum eigenvalue $\lambda_{\max}$ of the associated correlation coefficient matrix, and coverage factor k_p after h=10 sequences (M=10^5 trials) of MCM for the six coordinates of a point set collected on the gauge block and for its length estimate.

Measurand	Std. of estimates $\boldsymbol{y}$ (µm)	Std. of standard uncertainty $\boldsymbol{u_y}$ (µm)	Std. of coverage factor k_p	Std. of the maximum eigenvalue $\lambda_{\max}$ of correlation matrix
Coordinate X of point 1	0.02492	0.00867	0.00176	0.00252
Coordinate Y of point 1	0.01375	0.02838		
Coordinate Z of point 1	0.03048	0.00948		
Coordinate X of point 2	0.02175	0.01850		
Coordinate Y of point 2	0.01463	0.01854		
Coordinate Z of point 2	0.03217	0.03213		
Gauge's length	0.03371	0.03174	0.00000	0.00228

Incorporating a machine's error identifier (SAMBA) into the uncertainty estimator enables it to build the machine's kinematic chain at any target point and to compensate for the systematic effects irrespective of the positions of the machine's axes. This allows the uncertainty estimation of on-machine measurement based on the probed point set, unlike the task-specific method specified in ISO 15530-3 where the measurement function includes only the concerned geometric feature and the associated measurement bias as input quantities. ISO 15530-3 reduces the number of problem's dimensions to one, so the law of propagation of uncertainty becomes applicable. However, this simplification might cause the loss of some information encoded in the raw point set. Particularly, the covariance within the probed points and between them and the systematic error variables are the effects excluded in the task-specific technique. There might be certain change patterns in the shape of a point set that barely influence the geometric feature, such as the variations along the target surface in flatness measurement or any translation of the data set in many feature analyses such as form. If the probed points share an underlying systematic cause (such as a certain machine parameter) that accounts for such patterns, the covariance analysis allows considering them in the uncertainty assessment. Besides, the method proposed herein brings about flexibility in the strategy adopted for data acquisition and control over the input data such as combining and merging

separate point sets. This quality allows generating large diverse samples of probing data from the limited number of point sets, as done in this study for the gauge block and the sphere.

Although 5% less than the theoretical value for a coverage factor of 2, the coverage probability of 90% provided by the expanded uncertainty associated with the estimate for the gauge's length offers nevertheless a high level of confidence. Moreover, the coverage probability for sphericity remains over 94% for k=7, and it slightly decreases to 90% for k=8 (Figure 6-8a). This is despite the diversity of the axis positions included in each point set and the level of challenge imposed on the compensation capacity of the measurement function, which seem to be much more intense than what usually happens in practice.

As Figure 6-6 implies, the coverage probability is promising to be closer to 95% by improving the compensation for the measurement bias. This may become possible by a more accurate estimate for the machine parameters through a more elaborate error model, such as an 84-parameter model that includes more intra-axis errors, instead of the 13-parameter type used in this work. Such a modification should not only result in narrower offsets between a measurement result and the calibrated value of the measurand, but it reduces the uncertainty caused by the residual systematic errors. However, unlike the diameter estimation through a least-square sphere, which averages the unexplained volumetric errors, these effects directly influence the sphericity. Moreover, any estimate for the machine's geometric errors seems to be unable to explain the wide differences between the sphericity estimates and the calibrated value, even for k=1 (Figure 6-7b and Figure 6-8b). Because any compensation based on the machine's geometric errors, even via true machine parameters, would only translate the whole point set, due to the small distances within the points, which hardly affects the sphericity estimate. As a result, machine's imperfections other than its geometric errors, such as hysteresis errors and probe lobing errors, could in part account for such systematic errors observable in the sphericity analysis. Since the SAMBA method measures ball centres, any probe lobing or backlash of the linear axes is neither detected nor modelled and estimated. Identifying these errors and including their uncertainty in the uncertainty framework (Figure 6-2) could improve the error compensation and lead to a higher coverage probability with a smaller uncertainty interval.

6.6 Summary and conclusions

This study proposes a methodology for uncertainty evaluation in on-machine measurement. The measurement function receives the machine's axis positions at probe triggering and its geometric errors to build the kinematic chain for every measurement. The outputs are the compensated Cartesian positions of the probed point set in the workpiece frame. The uncertainty estimator assembles the covariance matrices associated with these two input vectors and triggers an adaptive MCM. The experimental validation of the uncertainty assessment includes the on-machine measurement of the length of a gauge block and the diameter and sphericity of a precision sphere. Various combinations of 15 point sets (bipoints) probed on the gauge block and random sampling from the pools built of up to 10 point sets collected on the sphere provide adequate data to calculate the coverage probability offered by the expanded uncertainty intervals. The following are the most important conclusions:

1. The multi-dimensional framework of the proposed uncertainty method preserves the important information about the random behaviour of a probed point set, encoded in the synthetized covariance matrix of the input quantities. This is unlike the task-specific method that functions based on the geometric feature measurement and its systematic bias.
2. The uncertainty scheme eliminates the need for any calibrated counterpart. The on-machine measurement function consists in the machine's kinematic model and can address any probed point set throughout the working volume of the machine.
3. The new method offers a coverage probability comparable to the theoretical level of confidence (95%). This metric is 90% for the gauge's length estimate and remains above 94% for the diameter estimates made by drawing at random from up to seven pooled point sets probed on the sphere. These are despite the disparate axis positions within each point set, which highly challenges the compensation competence of the on-machine measurement function.
4. The considerable contribution of unexplained volumetric errors to the uncertainty of on-machine measurement signifies the importance of the model sophistication in the identification of machine parameters.

6.7 Acknowledgements

This research was supported in part by the Natural Sciences and Engineering Research Council of Canada (NSERC) under the CANRIMT2 Strategic Research Network Grant NETGP 479639–15, and in part by the NSERC Discovery Grant of the third author. The authors would like to thank Mr. Guy Gironne and Mr. Vincent Mayer, the technicians of Virtual Manufacturing Research Laboratory (VMRL) at the mechanical engineering department of Polytechnique Montreal.

6.8 Annex A. Positions of the machine's rotary axes in validation experiments

Table A. 6-1: The positions of the machine's rotary axes during the on-machine measurement of the gauge's length.

		1	2	3	4	5	6	7	8	9	10	11	12	13	14	15
Side A	B	0	0	0	0	0	0	-42	-65	88	59	-1	51	-1	-82	42
	C	135	165	195	225	255	285	152	224	27	232	99	13	170	197	293
Side B	B	0	0	0	0	0	0	58	-15	22	-49	-27	-25	-4	-64	64
	C	135	165	195	225	255	285	210	4	64	18	9	16	244	329	124

Table A. 6-2: The positions of the machine's rotary axes during the on-machine measurement of the sphere's diameter and sphericity.

	1	2	3	4	5	6	7	8	9	10
B	55	-35	-40	-24	-11	19	32	-5	7	25
C	-22	-299	-171	-73	-9	-207	-254	-305	-132	-96

CHAPTER 7 : PROMPT UNCERTAINTY ESTIMATION WITH GUM FRAMEWORK FOR ON-MACHINE TOOL COORDINATE METROLOGY

When machine tools come to operation as measuring systems, they boost production efficiency because of the synergy between measurement and manufacture. Like in any other measurement procedure, the estimates for measurand obtained by these apparatus are complete only when they come with uncertainty metrics [42]. This is essential to establish the traceability of the measurement process.

On the other hand, generating an accurate uncertainty assessment is usually a time-consuming process. This stems from the computation cost of the propagation of uncertainty, which provides a basis for uncertainty estimators. The complexities associated with the analytical method for the propagation of uncertainty, known as the Markov formula [48], have brought about the development of numerical methods. The Monte Carlo method (MCM) is an iterative numerical approach to propagate distributions and is favourable for complex measurement functions or those with no closed-form mathematical expression. Moreover, according to the Central Limit Theorem [48], this method has promising convergence properties. Despite that, calling the measurement function once in every MCM trial highly increases the computation time, especially when it comes to an adaptive MCM where the convergence criteria require conducting an adequately large number of trials. Supplement 2 to GUM [50] specifies an alternative analytical solution for the propagation of uncertainty, referred to as the GUM uncertainty framework (GUF). Validated with an adaptive MCM, GUF is an efficient replacement for the inefficient MCM.

The GUF application in the metrology of machine tools has remained limited probably because of the convolutions of covariance analysis. These difficulties confine the GUF implementation to its single-output form, specified by GUM [42] as the law of propagation of uncertainty [44, 118]. In this study, however, a full covariance estimator allows for conducting GUF. Adhering to Supplement 2 to GUM [50], we then assess the validity of the GUF results by comparing them with the MCM estimates, considering predefined numerical tolerances. The conformity of GUF to the MCM results is also examined through ellipsoidal coverage regions and marginal probability density functions (PDFs).

7.1 Uncertainty evaluation

Two approaches evaluate the uncertainty associated with on-machine measurement results. An experimentally verified adaptive MCM provides uncertainty assessments against which the GUF results are validated.

7.1.1 Measurement function, input, and output quantities

The forward kinematic model of the machine serves as the on-machine measurement function. This model receives the probed axis positions and the machine parameters to calculate the compensated Cartesian coordinates in the workpiece frame using a chain of homogeneous transformation matrices that gives the relative position of the tool frame, as the stylus tip centre, with respect to the workpiece frame. When probing a point set of size n, like in estimating a ring's diameter by probing n points around its surface, the recorded $5n$ axis positions (five joint positions per probed point) together with 13 machine parameters, describing the geometric status of the machine, form the input data of uncertainty estimators. Therefore, the number of input quantities is $N = 5n + 13$. The 5×5 repeatability matrices of probed axis positions [103] and the 13×13 covariance matrix associated with the machine parameters [115] separately encode information on the correlations involved in on-machine measurement since the data on the machine parameters and the probed axis positions is acquired independently. As a result, the full covariance matrix of the input quantities is not directly obtainable from observations. To assemble these effects and obtain a single full covariance matrix $\boldsymbol{U_x}$ of dimension $(5n+13)\times(5n+13)$, a covariance estimator (6.3.2) simulates pseudo-repeatability tests as though the replicated tests of on-machine probing and those of geometric error indication (with SAMBA [26]) occur at the same time, which approximates the full covariance matrix of the input quantities.

The $3n$ compensated Cartesian coordinates of the probed points in the workpiece frame are the output quantities of the measurement function, thus the number of output quantities is $m = 3n$ and covariance matrix $\boldsymbol{U_y}$ is of dimension $3n\times3n$. When a probed point set is further processed to estimate the actual value of geometric feature attributes, the final covariance matrix diagonals are the scalar values (variance) associated with the estimates.

7.1.2 Monte Carlo method

MCM evaluates with the measurement function (the machine's forward kinematic model) an adequately large sample of input quantities $\boldsymbol{X}$, drawn at random from a joint distribution, resulting in a corresponding sample of output quantities $\boldsymbol{Y}$ [50, 79]. In an adaptive MCM, this procedure completes in h sequences, each including M=10^4 trials. During each sequence, matrix $\boldsymbol{G_X}$ accumulates M drawn input vectors $\boldsymbol{x}$ and matrix $\boldsymbol{G_Y}$ stores the corresponding evaluated output vectors $\boldsymbol{y}$ (Figure 7-1a). The latter provides essential statistical information to evaluate the uncertainty of the measurement function's outputs. As a result, regardless of the number of input and output quantities, an estimate for the joint PDF of the measurand is obtainable by MCM. Given a desirable coverage probability of p, the MCM simulator initially conducts $h_0 = 10$ sequences and then calculates output estimates $\boldsymbol{y}$, associated standard uncertainty $\boldsymbol{u_y}$, maximum eigenvalue $\lambda_{\max}$ of the output correlation matrix, and coverage factor k_p (Figure 7-1a). Comparing with predefined numerical tolerances, if convergence does not hold, it then conducts one more sequence and continues until the results converge. More details on the MCM procedure can be found in [115].

7.1.3 GUM uncertainty framework

The Taylor series of a function evaluates it with an infinite sum of the terms formed by the function's derivatives at a single point. Considering the first two terms of the Taylor series of a measurement function at the expectation values of the input quantities, GUM estimates the measurement function in a small neighbourhood of these expected values. Drawing an analogy between this neighbourhood and the standard uncertainty intervals of the input values, the law of propagation of uncertainty evaluates the standard uncertainty of the output quantities.

The GUF outcome is an estimate for the covariance matrix of the output variables. Then, compared with MCM, GUF reveals limited information about the measurand. Particularly, GUF does not provide any joint PDF for the output quantities. Nonetheless, fitting certain distributions, such as normal, to the obtained covariance matrix might approximate the true joint PDF of the output quantities.

Supplement 2 to GUM [50] develops this concept for multi-output measurement function $\boldsymbol{Y} = f(\boldsymbol{X})$, where $\boldsymbol{X} = [X_1, \dots, X_N]^{\mathrm{T}}$ is a vector of N input quantities and $\boldsymbol{Y} = [Y_1, \dots, Y_m]^{\mathrm{T}}$ is a vector of m output quantities. Covariance matrix $\boldsymbol{U_y}$ associated with output estimates $\boldsymbol{y}$ is

$$\boldsymbol{U_y} = \boldsymbol{C_x}\, \boldsymbol{U_x}\, \boldsymbol{C_x^{\mathrm{T}}} \tag{7-1}$$

where $\boldsymbol{U_x}$ is the covariance matrix associated with best estimates $\boldsymbol{x}$ of input quantities $\boldsymbol{X}$. In this equation, $\boldsymbol{C_x}$ is the sensitivity matrix at $\boldsymbol{X} = \boldsymbol{x}$ of dimension $m \times N$:

$$\boldsymbol{C_x} = \begin{bmatrix} \frac{\partial Y_1}{\partial X_1} & \cdots & \frac{\partial Y_1}{\partial X_N} \\ \vdots & \ddots & \vdots \\ \frac{\partial Y_m}{\partial X_1} & \cdots & \frac{\partial Y_m}{\partial X_N} \end{bmatrix} \tag{7-2}$$

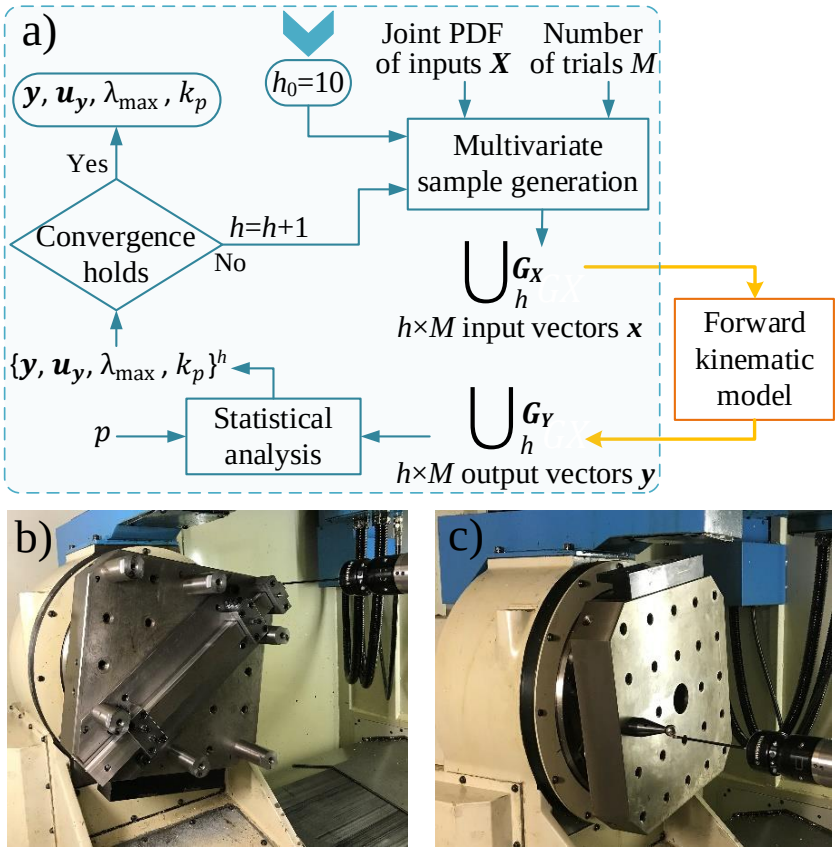

Figure 7-1: a) Data flow for uncertainty assessment in on-machine measurement using an adaptive Monte Carlo method, and on-machine measurement of b) gauge block and c) precision sphere.

Given the complexity of the on-machine measurement function, numerical differentiation is a suitable means to estimate the partial derivatives stored in the sensitivity matrix $\boldsymbol{C_x}$ given in Eq. 7-2. According to GUM [42], the step size for differentiating the measurement function with respect to the j^{th} input quantity X_j equals the corresponding standard uncertainty $u(x_j)$. Figure 7-2 illustrates the numerical differentiation procedure using the symmetric derivative.

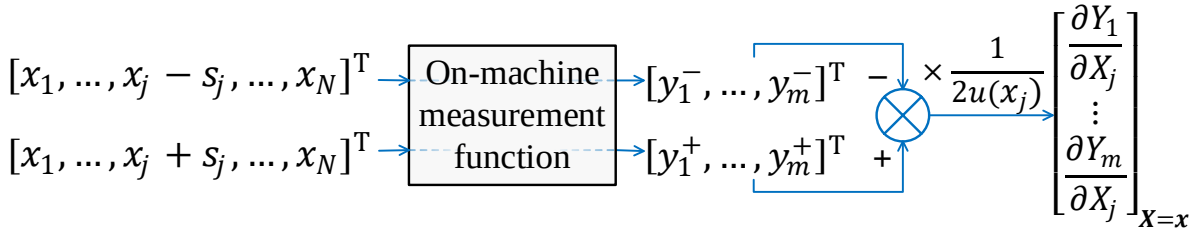

Figure 7-2: Numerical differentiation of the output quantities $\boldsymbol{Y}$ of on-machine measurement function at $\boldsymbol{X} = \boldsymbol{x}$ with respect to X_j, the j^{th} input quantity.

7.2 Validation of GUF with an adaptive Monte Carlo method

Supplement 2 to GUM [50] specifies the validation procedure of GUF using an adaptive MCM. After indicating the numerical tolerances for convergence criteria of the adaptive MCM, these metrics also define the required accuracy of the GUF results. This standard defines:

$$
\begin{aligned}
\boldsymbol{d_y} &= \left|\boldsymbol{y}^{\mathrm{GUF}} - \boldsymbol{y}^{\mathrm{MCM}}\right| \\
\boldsymbol{d_{u(y)}} &= \left|\boldsymbol{u(y)}^{\mathrm{GUF}} - \boldsymbol{u(y)}^{\mathrm{MCM}}\right| \\
d_{\lambda_{max}} &= \left|{\lambda_{max}}^{\mathrm{GUF}} - {\lambda_{max}}^{\mathrm{MCM}}\right| \\
d_{k_p} &= \left|{k_p}^{\mathrm{GUF}} - {k_p}^{\mathrm{MCM}}\right|
\end{aligned}
\qquad \text{7-3}
$$

where $\boldsymbol{d_y}$, $\boldsymbol{d_{u(y)}}$, $d_{\lambda_{\max}}$, and d_{k_p} are the absolute differences between the MCM and GUF results (denoted by the respective superscripts) respectively for best estimates $\boldsymbol{y}$, associated standard uncertainty $\boldsymbol{u(y)}$, the largest eigenvalue $\lambda_{\max}$ of the output correlation matrix, and coverage factor k_p. If numerical tolerance for $\boldsymbol{y}$ and $\boldsymbol{u(y)}$ is $\boldsymbol{\delta}$ and that for $\lambda_{\max}$ and k_p is ρ and κ_p, respectively,

the adaptive MCM validates the GUF results if all the absolute differences given by Eq. 7-3 are smaller than the corresponding numerical tolerances:

$$\begin{aligned} &\boldsymbol{d_y} \leq \boldsymbol{\delta} \\ &\boldsymbol{d_{u(y)}} \leq \boldsymbol{\delta} \\ &d_{\lambda_{max}} \leq \rho \\ &d_{k_p} \leq \kappa_p \end{aligned} \qquad \text{7-4}$$

7.3 Results and discussions

Experimental on-machine measurements on a gauge block (Figure 7-1b) and a precision sphere (Figure 7-1c) with a Mitsui Seiki HU40-T five-axis horizontal machining centre have already validated the MCM results by examining whether the uncertainty intervals provide the desired coverage probability. Each compensated coordinate of a probed point is regarded as having four significant decimal digits when expressed in mm. Then, the numerical tolerance for best estimates $\boldsymbol{y}$ and associated standard uncertainty $\boldsymbol{u}(\boldsymbol{y})$ is $\boldsymbol{\delta}$=0.05$\mathbf{1}_{3n\times1}$ μm, where $\mathbf{1}_{3n\times1}$ is a column vector of ones of length $3n$. The numerical tolerance for the largest eigenvalue $\lambda_{\max}$ of the output correlation matrix and coverage factor k_p is also ρ=κ_p=0.05. Table 7-1 includes the absolute differences for best estimates $\boldsymbol{y}$ and associated standard uncertainty $\boldsymbol{u}(\boldsymbol{y})$, determined for two points probed on the gauge block with a calibrated length of 500.0095 mm. For point 1, the probed positions for linear axes X, Y, and Z are -138.5650, 94.6560, and 196.2320 mm, and those for the rotary axes B and C are -42° and -293°, respectively. These values for point 2 are -61.2880, 48.3440, 246.8170 mm, -64°, and -124°, respectively. This table also includes the estimate for the gauge's length and its standard uncertainty along with the absolute differences between these quantities obtained with the two evaluation methods. The largest eigenvalue $\lambda_{\max}$ and coverage factor k_p given by GUF and their absolute difference are also presented in Table 7-2. All the absolute differences listed in these two tables are smaller than the stipulated numerical tolerances, which validates the GUF results. For best estimates $\boldsymbol{y}$, the maximum absolute difference is 72% of the specified numerical tolerance. This metric is 38% for standard uncertainty $\boldsymbol{u}(\boldsymbol{y})$. For maximum eigenvalue $\lambda_{\max}$ and coverage factor k_p, these differences are even smaller, that is, 1% and 9% of

the numerical tolerance, respectively. Verifying these criteria for different points probed at various positions on the machine tool holds the credibility of the GUF results.

For the three compensated coordinates of point 1, Figure 7-3a-c compare the ellipsoidal and rectangular coverage regions for coverage probability p=95% obtained with GUF and MCM, which encompass 2000 random output points. The smallest coverage region for each pair of output quantities is also estimated with a finite element method specified in Supplement 2 to GUM [50]. The difference between the coverage areas for coordinates X and Y does not exceed 1% for both the ellipsoidal and rectangular coverage regions. For these coordinates, the smallest coverage area is 982.8 μm^2, which is by less than 1% different from the GUF ellipsoidal coverage area. These differences for the X-Z and Y-Z pairs also do not exceed 1%, whose smallest areas of coverage region are 962.6 and 1178.5 μm^2, respectively. Figure 7-3d-f demonstrate the closeness between the MCM marginal PDFs for the compensated coordinates of point 1 and the normal PDFs fitted based on best estimates and the associated covariance matrix given by GUF.

For almost all the considered tasks, the adaptive MCM converges in h=10 sequences, including. M=10^5 trials. For the estimation of the gauge's length, where the probed point set includes two points (n=2), the adaptive MCM completes in 167 s, on a computer with an Intel i7 processor running at 4.2 GHz, 32 GB of RAM, and Windows 10. This time for GUF is 7 s, 24 times faster than the adaptive MCM. In a different task, the adaptive MCM estimates the diameter of a sphere and the associated uncertainty in 1967 s, whereas GUF completes in 12 s, being 164 times faster. Figure 7-4 compares the computation times between the adaptive MCM and GUF for the sphere's diameter obtained from the point sets with different sizes varying from n=10 to 25. The computation time of GUF increases almost linearly proportional to the size of point set n. On average, GUF is 249 times more efficient than MCM in the sphere identification. This notable reduction in the computation cost mainly originates from the costly covariance simulator that operates based on an MCM algorithm (for both the MCM and GUF uncertainty schemes) and has to recur every MCM trial, whereas this occurs only once in GUF. This difference is more evident for larger point sets, where the number of calls for the forward kinematic model rises.

Table 7-1: The adaptive MCM and GUF results for best estimates y and associated standard uncertainty $u(y)$ together with their absolute differences obtained for the compensated coordinates of two points probed on a gauge block and its estimated length.

	Best estimate $\boldsymbol{y}$ (mm)				Standard uncertainty $\boldsymbol{u(y)}$ (µm)			
	MCM	GUF	$\boldsymbol{d_y}$	$\boldsymbol{d_y/\delta}$ (%)	MCM	GUF	$\boldsymbol{d_{u(y)}}$	$\boldsymbol{d_{u(y)}/\delta}$ (%)
Coordinate X of point 1	-178.6461	-178.6462	2.89E-05	58	6.7	6.7	4.38E-03	9
Coordinate Y of point 1	-178.6461	-178.6461	3.61E-05	72	8.2	8.2	1.23E-02	25
Coordinate Z of point 1	53.1107	53.1107	2.54E-05	51	7.6	7.6	4.25E-03	9
Coordinate X of point 2	179.1009	179.1009	1.38E-05	28	6.8	6.8	1.71E-03	3
Coordinate Y of point 2	179.0881	179.0881	1.18E-05	24	8.4	8.4	1.20E-02	24
Coordinate Z of point 2	53.1067	53.1068	1.79E-05	36	7.7	7.7	1.91E-02	38
Gauge's length	499.9966	499.9966	1.21E-05	24	9.0	9.0	6.76E-03	14

Table 7-2: The adaptive MCM and GUF results for the largest eigenvalue $\lambda_{\max}$ of the output correlation matrix and coverage factor k_p along with their absolute differences obtained for the compensated coordinates of two points and the estimated length listed in Table 7-1.

	$\lambda_{\max}$				k_p			
	MCM	GUF	$d_{\lambda_{\max}}$	$d_{\lambda_{\max}}/\rho$ (%)	MCM	GUF	d_{k_p}	d_{k_p}/κ_p (%)
Point set (Table 7-1)	1.313	1.312	4.80E-04	1	3.55	3.55	4.50E-03	9
Length	1.000	1.000	0	0	1.96	1.96	8.45E-04	2

7.4 Summary and Conclusions

An adaptive MCM developed for uncertainty assessment in on-machine measurement examines the feasibility of GUF. We apply these methods to obtain the best estimates and the associated standard uncertainty of the length of a gauge block and the diameter of a precision sphere. The computation cost of the uncertainty evaluation is also measured for the sphere's diameter obtained from sets of n=10 to 25 points. The summarized conclusions are as follows:

1. The adaptive MCM validates the GUF application for uncertainty assessment in on-machine probing and part verification. For the studied case of the gauge block measurement, the maximum absolute differences between the MCM and the GUF results

are 72% and 38% of the specified numerical tolerance, respectively for best estimates and the associated standard uncertainty. These measures are 1% and 9% for maximum eigenvalue $\lambda_{\max}$ of the output correlation matrix and coverage factor k_p, respectively.

2. Besides complying with the criteria specified by Supplement 2 to GUM, the ellipsoidal and rectangular coverage regions as well as the marginal PDFs given by GUF closely approximate those obtained by MCM, which further validates GUF.

3. The GUF implementation dramatically decreases the uncertainty computation time. This method evaluates the uncertainty associated with a compensated bipoint probed on the gauge block and that with its length estimate in 7 s, which is 24 times faster than the adaptive MCM (167 s). For a point set of size 25 probed on the sphere, GUF gives the uncertainty associated with the compensated points and with the sphere's diameter in 12 s, whereas this time for MCM is 1967 s, i.e. 164 times longer. On average, GUF is 249 times more efficient in the sphere identification.

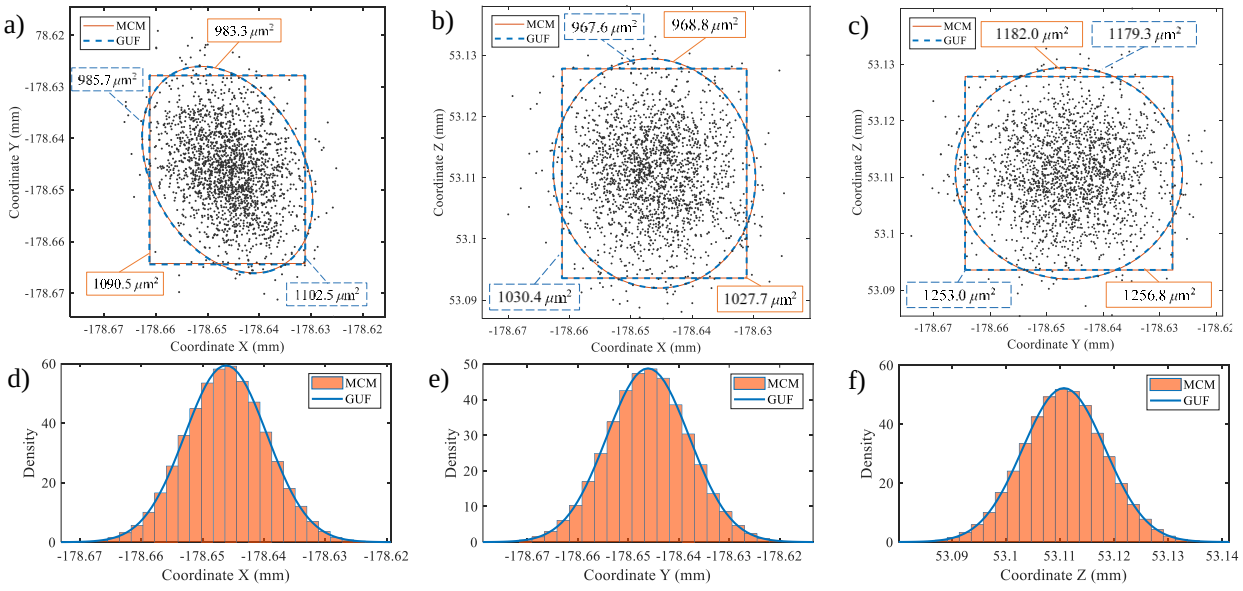

Figure 7-3: a-c) Ellipsoidal and rectangular coverage regions (for coverage probability p=0.95) obtained by the adaptive MCM and GUF for the compensated coordinates of a point probed on the gauge block. Also shown are 2,000 random output points. d-f) Comparison between the marginal histograms given by the adaptive MCM and GUF.

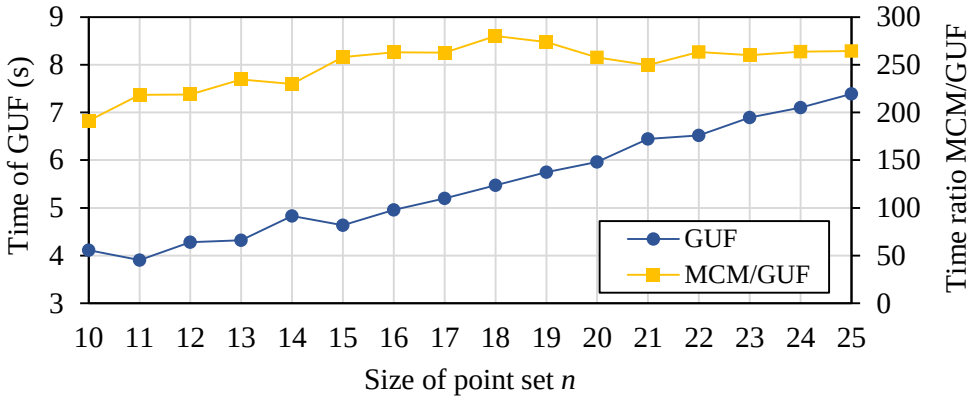

Figure 7-4: The computation time of GUF for uncertainty evaluation of the sphere's diameter from the point sets with different sizes and the time ratio of the adaptive MCM to GUF.

CHAPTER 8 : GENERAL DISCUSSION

The uncertainty evaluation of the on-machine probing results poses new challenges because of the uncontrolled environment of the shop floor and the unsteady status of machine tools. We can assume that most of the uncertainty components that originate from the measuring system (including the machine tool and probe) manifest themselves in the form of either probing repeatability or an imperfect compensation for the measurement bias. The former includes the random behaviour of the system, whereas the latter stands for the post-compensation residual systematic effects. Therefore, it is crucial to ensure the utmost randomness in the observations during the replicated probing tasks aimed at the quantification of the probing repeatability. This is obtainable by a visual inspection of the raw probing results to make sure they exclude any systematic trend. This most likely requires completing these tests in a short period to prevent the thermal systematic effects. Then, the repeatability obtained by this means inevitably includes the short-term variations of the probing results.

On the other hand, the data required to identify the variations of the machine's status (quantified by the machine parameters) should accumulate in the long-term, for example on a day-to-day basis, because of two main reasons. First, the machine's state is less likely to change over the short term and monitoring its condition over days or weeks gives a more complete picture of the range within which the machine alters. Second, knowing the machine's fluctuations over the long term helps anticipate the long-term repeatability of on-machine probing results, which can be difficult to determine directly.

Estimating the long-term repeatability of the on-machine probing results based on the machine's alternations has an important by-product: the covariance between these two sets of data. This covariance matrix gives an estimate for the full joint PDF of the input quantities of the on-machine measurement function. Since these input values possibly correlate, this covariance matrix increases the accuracy of the uncertainty estimates. This feature also allows for implementing GUF, developed for multi-output problems to compensate for the inefficiency of an adaptive MCM. Because the other existing uncertainty evaluators are lacking this important aspect, they reduce the problem dimensions by converting the acquired point set to the concerned geometric feature. This makes it possible to apply the law of propagation of uncertainty, which ignores the covariance effects.

The post-compensation residuals of the measurement bias mainly stem from two factors. First, the uncertainty associated with the machine parameters that can originate from the long-term repeatability of the SAMBA probing results, mostly caused by the evolution in the machine's state, directly contributes to the uncertainty of the calculated volumetric error. Second, the limitations of the SAMBA's error model and the unconsidered geometric errors, such as backlash, systematically falsify the estimated measurement bias. Moreover, the variations of these excluded errors can affect the repeatability of the SAMBA probing results. That is, even if all the machine's considered parameters remain unchanged from time to time, the probing results might fluctuate because of the variations in the unconsidered errors and, consequently, in the recorded volumetric error by the SAMBA method. This second portion of the residual systematic errors causes the unexplained volumetric errors captured through the validation of the SAMBA procedure. Therefore, as long as these unexplained volumetric errors exist, the uncertainty evaluated for the machine parameters (Chapter 5) might fail to encompass their true values with the expected coverage probability. Consequently, it is essential to determine the unexplained measurement bias and to involve them in the uncertainty scheme.

Benefiting from SAMBA, an indirect method to identify the machine parameters, enables the uncertainty estimator to evaluate the uncertainty associated with the first-hand probing outcomes, being the acquired point set. This is unlike the method given in ISO 15530-3, where the knowledge about the measurement bias and its uncertainty merely concerns a geometric feature defined by a probed point set and is limited to a certain set-up and probing task. Nevertheless, the main distinction of the developed uncertainty scheme lies in the covariance analysis. The major challenge in quantifying the input covariance matrix is that the on-machine probing and the identification of the machine parameters do not occur all at once. This makes it impossible to track the simultaneous variations of the two or more input quantities. To overcome this challenge, a simulation of the long-term replicated on-machine probing, conforming to the day-to-day monitoring of the machine, models the possible correlations between the inputs.

CHAPTER 9 : CONCLUSIONS AND FUTURE WORKS

Considering the whole study and the knowledge gained in the course of this research, this chapter lists some important conclusions and future works.

9.1 General conclusions

- Despite the highly diverse axis positions considered in the experimental validation of the proposed uncertainty scheme, the coverage probability remains comparable to the desired level of confidence. This proves the traceability of the on-machine measurement results obtained by the used machine tool. Implementing the uncertainty estimator allows for converting this machine tool to a traceable CMM.
- The capacity for a full covariance analysis makes a fundamental distinction between this scheme and the other uncertainty evaluators. This feature is expected to increase the accuracy of uncertainty estimates. The other methods reduce the problem's dimensions so that they can apply the law of propagation of uncertainty that excludes any covariance between the input quantities.
- For a multi-output measurement task as on-machine probing, having the covariance matrix of the inputs allows for conducting GUF. This approach considerably increases the efficiency of the uncertainty estimator without compromising accuracy. The high computation costs of calling the machine's forward kinematic model and the MCM-based covariance simulator are the main reasons for the inefficiency of the adaptive MCM.
- The proposed method eliminates the need for a calibrated counterpart. This competence is achievable by using SAMBA that indirectly identifies the machine parameters that are the underlying causes of the measurement bias and can estimate the volumetric error at any position on the machine tool.
- The repeatability of on-machine measurement is predictable for any position on the machine tool and any approach direction. This, besides using an indirect identifier for the machine parameters, accounts for the flexibility of the proposed method in addressing the

uncertainty of any probed point set regardless of its position and the adopted probing strategy.

- GUF can effectively replace the adaptive MCM in uncertainty estimation for the identified machine's geometric errors via SAMBA. A considerable improvement in the computation cost is obtainable, which can make a remarkable difference when optimizing the SAMBA strategy aiming at minimizing the uncertainty associated with the outputs.
- Unlike the feature-based uncertainty approaches, this methodology deals with the direct outcomes of an on-machine measurement, i.e. the probed points. This practice provides in-depth knowledge about the geometric features defined by an acquired point set. This also enables quantifying the sensitivity of the estimated feature with respect to the recorded joint positions and the geometric errors of the machine.
- Unlike the compensation for systematic errors, which might improve by using more elaborate error models, the random effects are inevitable. However, the high short-term on-machine probing repeatability of the used machine tool and the negligible effect of hysteresis prevent form considerable growth of the expanded uncertainty.
- The noticeable effects of the machine's resolution on the recorded coordinates and their variance show the importance of considering this factor in the design of the repeatability tests. Including the probing tasks with the approach directions slightly deviated from the prismatic axes can make this effect manifest itself in the probing results. Moreover, the inverse kinematic model should be able to map the calculated joint positions onto the machine's resolution grids.

9.2 Future works

Considering the assumptions made in the beginning and the limitations that arose during this research, addressing the following concerns in future works seems necessary:

- Because of the GD&T considerations, the uncertainty interval should be as small as possible while it holds the desired coverage probability. This calls for maximizing the compensation for measurement bias, which minimizes the systematic offset between true value of the measurand and its estimate. The forward kinematic model of the machine measures this

error based on the geometric errors identified by SAMBA. Therefore, the more accurate the machine parameters, the smaller the on-machine measurement uncertainty. This calls for adopting a more complete model by SAMBA and optimizing its strategy.

- One can categorize the uncertainty sources involved in on-machine measurement into three main components: the measuring system, part, and environment. Although through its systematic and random behaviour, the measuring system (the machine tool and probe) indirectly reveals some important environmental effects, such as thermal changes, the part's role requires separate attention. The effects of thermal deflections, surface finish, form errors, and clamping distortion are the potential uncertainty sources coming from the part.
- Implementing the proposed uncertainty scheme on other machine tools with different topologies can examine its reproducibility.
- More complex GD&T tasks, such as freeform measurements, can further challenge the developed methodology.

REFERENCES

[1] JSGM, "15530-3:2011; Geometrical product specifications (GPS) -- Coordinate measuring machines (CMM): Technique for determining the uncertainty of measurement -- Part 3: Use of calibrated workpieces or measurement standards," ed: Geneva: ISO, 2011.

[2] JSGM, "15530-4:2008; Geometrical Product Specifications (GPS) — Coordinate measuring machines (CMM): Technique for determining the uncertainty of measurement — Part 4: Evaluating task-specific measurement uncertainty using simulation," ed: Geneva: ISO, 2008.

[3] "International Vocabulary of Metrology–Basic and General Concepts and Associated Terms," vol. 30, ed: International Bureau of Weights and Measures (BIPM), 2012.

[4] U. Mutilba, E. Gomez-Acedo, G. Kortaberria, A. Olarra, and J. Yagüe-Fabra, "Traceability of On-Machine Tool Measurement: A Review," *Sensors,* vol. 17, p. 1605, 2017.

[5] P. Swann, "The Economics of Metrology and Measurement Report for National Measurement Office," Dep. Bus., Innov. Ski. Innov. Econ. Ltd2009.

[6] H. M. P. Lobato, "An investigation into coordinate measuring machine task specific measurement uncertainty and automated conformance assessment of airfoil leading edge profiles," Structural Materials Research Centre, School of Metallurgy and Materials, University of Birmingham, 2012.

[7] A. Weckenmann, T. Estler, G. Peggs, and D. McMurtry, "Probing Systems in Dimensional Metrology," *CIRP Annals,* vol. 53, pp. 657-684, 2004.

[8] M. R. Verma, E. Chatzivagiannis, D. Jones, and P. G. Maropoulos, "Comparison of the Measurement Performance of High Precision Multi-axis Metal Cutting Machine Tools," *Procedia CIRP,* vol. 25, pp. 138-145, 2014.

[9] F. Zhao, X. Xu, and S. Q. Xie, "Computer-Aided Inspection Planning—The state of the art," *Computers in Industry,* vol. 60, pp. 453-466, 2009.

[10] P. Saunders, N. Orchard, P. G. Maropoulos, and A. P. Graves, "Integrated design and dimensional measurement: A review of the state of the art," in *Int. Conf. Manuf. Res*, 2010.

[11] R. J. Hocken and P. H. Pereira, *Coordinate Measuring Machines and Systems, Second Edition (Manufacturing Engineering and Materials Processing)*, 2nd ed.: CRC Press, 2011.

[12] M.-W. Cho, H. Lee, G.-S. Yoon, and J.-H. J. K. I. J. Choi, "A computer-aided inspection planning system for on-machine measurement — Part II: Local inspection planning —," vol. 18, pp. 1358-1367, 2004.

[13] F. Keller, M. Franke, N. Gerwien, L. Groos, C. Held, and K. Wendt, "Traceability of on-machine measurements under a wide range of working conditions," in *Proceedings of the*

Traceable in-Process Dimensional Measurement Final Workshop, Physikalisch-Technische-Bundesanstalt (PTB), 2015.

[14] M. Shiraishi, "Scope of in-process measurement, monitoring and control techniques in machining processes—Part 2: In-process techniques for workpieces," *Precision Engineering*, vol. 11, pp. 27-37, 1989.

[15] T. Yandayan and M. Burdekin, "In-process dimensional measurement and control of workpiece accuracy," *International Journal of Machine Tools and Manufacture*, vol. 37, pp. 1423-1439, 1997.

[16] K. Vacharanukul and S. Mekid, "In-process dimensional inspection sensors," *Measurement*, vol. 38, pp. 204-218, 2005.

[17] M. Shiraishi, "Scope of in-process measurement, monitoring and control techniques in machining processes — Part 1: In-process techniques for tools," *Precision Engineering*, vol. 10, pp. 179-189, 1988.

[18] M. Shiraishi, "Scope of in-process measurement, monitoring and control techniques in machining processes—Part 3: In-process techniques for cutting processes and machine tools," *Precision Engineering*, vol. 11, pp. 39-47, 1989.

[19] T. Kohno, Y. Okazaki, N. Ozawa, K. Mitui, and M. Omoda, "In-process measurement and a workpiece-referred form accuracy control system (WORFAC): concept of the method and preliminary experiment," *Precision Engineering*, vol. 11, pp. 9-14, 1989.

[20] T. Yazawa, T. Yamazaki, and T. Kohno, "In-process measurement and workpiece-refered form accuracy control (7th report) : Controlled cutting with reference surface for central part and expansion to periphery," *the Japan Society for Precision Engineering*, vol. 64, pp. 1689-1693, 1998.

[21] Y. Takaya, "In-process and on-machine measurement of machining accuracy for process and product quality management: A review," *International Journal of Automation Technology*, vol. 8, pp. 4-19, 2014.

[22] S. Ibaraki and W. Knapp, "Indirect measurement of volumetric accuracy for three-axis and five-axis machine tools: A review," *International Journal of Automation Technology*, vol. 6, pp. 110-124, 2012.

[23] Y. Ihara, "Ball bar measurement on machine tools with rotary axes," *International Journal of Automation Technology*, vol. 6, pp. 180-187, 2012.

[24] S. Weikert, "R-Test, a New Device for Accuracy Measurements on Five Axis Machine Tools," *CIRP Annals*, vol. 53, pp. 429-432, 2004.

[25] T. Erkan, J. R. R. Mayer, and Y. Dupont, "Volumetric distortion assessment of a five-axis machine by probing a 3D reconfigurable uncalibrated master ball artefact," *Precision Engineering*, vol. 35, pp. 116-125, 2011.

[26] J. R. R. Mayer, "Five-axis machine tool calibration by probing a scale enriched reconfigurable uncalibrated master balls artefact," *CIRP Annals*, vol. 61, pp. 515-518, 2012.

[27] M. M. Rahman and J. R. R. Mayer, "Five axis machine tool volumetric error prediction through an indirect estimation of intra- and inter-axis error parameters by probing facets on a scale enriched uncalibrated indigenous artefact," *Precision Engineering*, vol. 40, pp. 94-105, 2015.

[28] A. D. Mazzeo, A. J. Stein, D. L. Trumper, and R. J. Hocken, "Atomic force microscope for accurate dimensional metrology," *Precision Engineering*, vol. 33, pp. 135-149, 2009.

[29] D. A. Lucca, Y. W. Seo, and R. Komanduri, "Effect of Tool Edge Geometry on Energy Dissipation in Ultraprecision Machining," *CIRP Annals*, vol. 42, pp. 83-86, 1993.

[30] T. Yamaguchi, M. Higuchi, S. Shimada, and T. Kaneeda, "Tool life monitoring during the diamond turning of electroless Ni–P," *Precision Engineering*, vol. 31, pp. 196-201, 2007.

[31] W. M. Mohammed, E. Ng, and M. A. Elbestawi, "Modeling the effect of compacted graphite iron microstructure on cutting forces and tool wear," *CIRP Journal of Manufacturing Science and Technology*, vol. 5, pp. 87-101, 2012.

[32] G. Zhang, S. To, and G. Xiao, "Novel tool wear monitoring method in ultra-precision raster milling using cutting chips," *Precision Engineering*, vol. 38, pp. 555-560, 2014.

[33] Y. Wang, N. Suzuki, E. Shamoto, and Q. Zhao, "Investigation of tool wear suppression in ultraprecision diamond machining of die steel," *Precision Engineering*, vol. 35, pp. 677-685, 2011.

[34] R. Karadayi, "Process Closed Loop Metrology for Adaptive Manufacturing," in *Proceedings of the Annual Workshop and Conference*, Toronto, ON, Canada, 10–15 March 2014.

[35] S. Nisch and R. Schmitt, "Production integrated 3D measurements on large machine tools," in *Proceedings of the Large Volume Metrology Conference (LVMC)*, Chester, UK, 2010.

[36] R. Schmitt, P. Jatzkowski, and M. Peterek, "Traceable measurements using machine tools," in *Proceedings of the Laser Metrology and Machine Performance X: 10th International Conference and Exhibition on Laser Metrology, Machine Tool, CMM and Robotic Performance, Lamdamap*, Buckinghamshire, UK, 2013, pp. 20-21.

[37] R. H. Schmitt, M. Peterek, E. Morse, W. Knapp, M. Galetto, F. Härtig, *et al.*, "Advances in Large-Scale Metrology – Review and future trends," *CIRP Annals*, vol. 65, pp. 643-665, 2016.

[38] T. Nomura, K. Yoshikawa, H. Tashiro, K. Takeuchi, N. Ozawa, Y. Okazaki, *et al.*, "On-machine shape measurement of workpiece surface with Fizeau interferometer," *Precision Engineering*, vol. 14, pp. 155-159, 1992.

[39] D. Ross-Pinnock and P. G. Maropoulos, "Identification of Key Temperature Measurement Technologies for the Enhancement of Product and Equipment Integrity in the Light Controlled Factory," *Procedia CIRP,* vol. 25, pp. 114-121, 2014.

[40] J. Bryan, "International Status of Thermal Error Research," *CIRP Annals,* vol. 39, pp. 645-656, 1990.

[41] J. Mayr, J. Jedrzejewski, E. Uhlmann, M. Alkan Donmez, W. Knapp, F. Härtig, *et al.*, "Thermal issues in machine tools," *CIRP Annals,* vol. 61, pp. 771-791, 2012.

[42] JSGM, "100:2008(E); Evaluation of measurement data — Guide to the expression of uncertainty in measurement (GUM)," ed: Geneva: ISO, 2008.

[43] JCGM, "ISO 14253-1:2013. Geometrical product specifications (GPS) -- Inspection by measurement of workpieces and measuring equipment -- Part 1: Decision rules for proving conformity or non conformity with specifications," ed: Geneva: ISO, 2013.

[44] U. Mutilba, E. Gomez-Acedo, A. Sandá, I. Vega, and J. A. Yagüe-Fabra, "Uncertainty assessment for on-machine tool measurement: An alternative approach to the ISO 15530-3 technical specification," *Precision Engineering,* vol. 57, pp. 45-53, 2019.

[45] U. Mutilba, A. Sandá, I. Vega, E. Gomez-Acedo, I. Bengoetxea, and J. A. Yagüe Fabra, "Traceability of on-machine tool measurement: Uncertainty budget assessment on shop floor conditions," *Measurement,* vol. 135, pp. 180-188, 2019.

[46] P. Pérez, S. Aguado, J. A. Albajez, J. Velazquez, J. Santolaria, and J. J. Aguilar, "Analysis of the measurement capacity of a machine tool," *Procedia Manufacturing,* vol. 13, pp. 434-441, 2017.

[47] R. Schmitt and M. Peterek, "Traceable Measurements on Machine Tools - Thermal Influences on Machine Tool Structure and Measurement Uncertainty," *Procedia CIRP,* vol. 33, pp. 576-580, 2015.

[48] M. G. Cox and B. R. L. Siebert, "The use of a Monte Carlo method for evaluating uncertainty and expanded uncertainty," *Metrologia,* vol. 43, pp. S178-S188, 2006.

[49] G. C. Maurice and R. L. S. Bernd, "The use of a Monte Carlo method for evaluating uncertainty and expanded uncertainty," *Metrologia,* vol. 43, p. S178, 2006.

[50] JCGM, "102:2011(E); Evaluation of measurement data – Supplement 2 to the "Guide to the expression of uncertainty in measurement" – Extension to any number of output quantities," ed: Geneva: ISO, 2011.

[51] J. A. Rice, *Mathematical Statistics and Data Analysis*: Cengage Learning, 2007.

[52] P. M. Harris and M. G. Cox, "On a Monte Carlo method for measurement uncertainty evaluation and its implementation," *Metrologia,* vol. 51, pp. S176-S182, 2014.

[53] A. Balsamo, M. Di Ciommo, R. Mugno, B. I. Rebaglia, E. Ricci, and R. Grella, "Evaluation of CMM Uncertainty Through Monte Carlo Simulations," *CIRP Annals - Manufacturing Technology,* vol. 48, pp. 425-428, 1999.

[54] G. Belforte, B. Bona, E. Canuto, F. Donati, F. Ferraris, I. Gorini, *et al.*, "Coordinate Measuring Machines and Machine Tools Selfcalibration and Error Correction," *CIRP Annals,* vol. 36, pp. 359-364, 1987.

[55] H. Schwenke, B. R. L. Siebert, F. Wäldele, and H. Kunzmann, "Assessment of Uncertainties in Dimensional Metrology by Monte Carlo Simulation: Proposal of a Modular and Visual Software," *CIRP Annals,* vol. 49, pp. 395-398, 2000.

[56] J. Sładek and A. Gąska, "Evaluation of coordinate measurement uncertainty with use of virtual machine model based on Monte Carlo method," *Measurement,* vol. 45, pp. 1564-1575, 2012.

[57] X.-l. Wen, Y.-b. Zhao, D.-x. Wang, and J. Pan, "Adaptive Monte Carlo and GUM methods for the evaluation of measurement uncertainty of cylindricity error," *Precision Engineering,* vol. 37, pp. 856-864, 2013.

[58] J.-P. Kruth, N. Van Gestel, P. Bleys, and F. Welkenhuyzen, "Uncertainty determination for CMMs by Monte Carlo simulation integrating feature form deviations," *CIRP Annals,* vol. 58, pp. 463-466, 2009.

[59] M. Ren, C. Cheung, L. Kong, and S. Wang, "Quantitative Analysis of the Measurement Uncertainty in Form Characterization of Freeform Surfaces Based on Monte Carlo Simulation," *Procedia CIRP,* vol. 27, pp. 276-280, 2015.

[60] B. Bringmann and W. Knapp, "Model-based 'Chase-the-Ball' Calibration of a 5-Axes Machining Center," *CIRP Annals,* vol. 55, pp. 531-534, 2006.

[61] B. Bringmann and W. Knapp, "Machine tool calibration: Geometric test uncertainty depends on machine tool performance," *Precision Engineering,* vol. 33, pp. 524-529, 2009.

[62] L. Andolfatto, J. R. R. Mayer, and S. Lavernhe, "Adaptive Monte Carlo applied to uncertainty estimation in five axis machine tool link errors identification with thermal disturbance," *International Journal of Machine Tools and Manufacture,* vol. 51, pp. 618-627, 2011.

[63] A. Los and J. R. R. Mayer, "Application of the adaptive Monte Carlo method in a five-axis machine tool calibration uncertainty estimation including the thermal behavior," *Precision Engineering,* vol. 53, pp. 17-25, 2018.

[64] JSGM, "ISO 230-2:2014; Test code for machine tools --Part 2: Determination of accuracy and repeatability of positioning of numerically controlled axes," ed: Geneva: ISO, 2014.

[65] JSGM, "ISO 230-6:2002 ; Test code for machine tools --Part 6: Determination of positioning accuracy on body and face diagonals (Diagonal displacement tests)," ed: Geneva: ISO, 2002.

[66] H. F. F. Castro and M. Burdekin, "Dynamic calibration of the positioning accuracy of machine tools and coordinate measuring machines using a laser interferometer," *International Journal of Machine Tools and Manufacture,* vol. 43, pp. 947-954, 2003.

[67] M. Paweł and P. Bartosz, "Rapid method to determine accuracy and repeatability of positioning of numerically controlled axes," *International Journal of Machine Tools and Manufacture,* vol. 137, pp. 1-12, 2019.

[68] JSGM, "230-10:2016; Test code for machine tools --Part 10: Determination of the measuring performance of probing systems of numerically controlled machine tools," ed: Geneva: ISO, 2016.

[69] A. Woźniak and M. Jankowski, "New method of testing of the repeatability of CMM articulating heads," *The International Journal of Advanced Manufacturing Technology,* vol. 56, pp. 677-682, 2011.

[70] A. Woźniak, "Study of the repeatability of the magnetic joint in the probes used in coordinate measuring machines," *The International Journal of Advanced Manufacturing Technology,* vol. 47, pp. 1209-1216, 2010.

[71] H. W. Lee, J. R. Chen, S. P. Pan, H. C. Liou, and P. E. Hsu, "Relationship between ISO 230-2/-6 Test Results and Positioning Accuracy of Machine Tools Using LaserTracer," *Applied Sciences,* vol. 6, p. 105, 2016.

[72] M. Jankowski, A. Woźniak, and J. R. R. Mayer, "On-machine and In-laboratory Investigation of Errors of Probes for CNC Machine Tools: Proceedings of the International Conference," in *ICERA*, 2019, pp. 433-439.

[73] M. Jankowski and A. Wozniak, "Mechanical model of errors of probes for numerical controlled machine tools," *Measurement,* vol. 77, pp. 317-326, 2016.

[74] A. Piratelli-Filho and B. Di Giacomo, "CMM uncertainty analysis with factorial design," *Precision Engineering,* vol. 27, pp. 283-288, 2003.

[75] A. Weckenmann, M. Knauer, and H. Kunzmann, "The Influence of Measurement Strategy on the Uncertainty of CMM-Measurements," *CIRP Annals,* vol. 47, pp. 451-454, 1998.

[76] S. D. Phillips, B. Borchardt, W. T. Estler, and J. Buttress, "The estimation of measurement uncertainty of small circular features measured by coordinate measuring machines," *Precision Engineering,* vol. 22, pp. 87-97, 1998.

[77] L. Zhong, Q. Bi, N. Huang, and Y. Wang, "Dynamic accuracy evaluation for five-axis machine tools using S trajectory deviation based on R-test measurement," *International Journal of Machine Tools and Manufacture,* vol. 125, pp. 20-33, 2018.

[78] L. Zhong, Q. Bi, and Y. Wang, "Volumetric accuracy evaluation for five-axis machine tools by modeling spherical deviation based on double ball-bar kinematic test," *International Journal of Machine Tools and Manufacture,* vol. 122, pp. 106-119, 2017.

[79] JCGM, "101:2008(E); Evaluation of measurement data — Supplement 1 to the “Guide to the expression of uncertainty in measurement” — Propagation of distributions using a Monte Carlo method," ed: Geneva: ISO, 2008.

[80] K.-C. Fan, H. Wang, F.-J. Shiou, and C.-W. Ke, "Design analysis and applications of a 3D laser ball bar for accuracy calibration of multiaxis machines," *Journal of Manufacturing Systems,* vol. 23, pp. 194-203, 2004.

[81] J. Gu, J. S. Agapiou, and S. Kurgin, "Error compensation and accuracy improvements in 5-axis machine tools using the global offset method," *Journal of Manufacturing Systems,* vol. 44, pp. 324-331, 2017.

[82] A. Woźniak and M. Dobosz, "Research on hysteresis of triggering probes applied in coordinate measuring machines," *Metrology and Measurement Systems,* vol. 12, pp. 393-412, 2005.

[83] P. A. C. Miguel, T. King, and A. J. Abackerli, "CMM touch trigger performance verification using a probe test apparatus," *Journal of the Brazilian Society of Mechanical Sciences and Engineering,* vol. 25, pp. 147-153, 2003.

[84] A. Woźniak and K. Męczyńska, "Measurement hysteresis of touch-trigger probes for CNC machine tools," *Measurement,* p. 107568, 2020.

[85] Y.-L. Shen and X. Zhang, "Modelling of pretravel for touch trigger probes on indexable probe heads on coordinate measuring machines," *The International Journal of Advanced Manufacturing Technology,* vol. 13, pp. 206-213, 1997.

[86] Z. Bohan, G. Feng, and L. Yan, "Study on Pre-travel Behaviour of Touch Trigger Probe under Actual Measuring Conditions," *Procedia CIRP,* vol. 27, pp. 53-58, 2015.

[87] A. Wozniak and M. Jankowski, "Random and Systematic Errors Share in Total Error of Probes for CNC Machine Tools," *Journal of Manufacturing and Materials Processing,* vol. 2, p. 17, 2018.

[88] J. Neter, M. H. Kutner, C. J. Nachtsheim, and W. Wasserman, *Applied linear statistical models* vol. 4: Irwin Chicago, 1996.

[89] F. Khameneifar and H.-Y. Feng, "Airfoil profile reconstruction under the uncertainty of inspection data points," *The International Journal of Advanced Manufacturing Technology,* vol. 71, pp. 675-683, 2014.

[90] F. Khameneifar and H.-Y. Feng, "A new methodology for evaluating position and orientation errors of airfoil sections," *The International Journal of Advanced Manufacturing Technology,* vol. 83, pp. 1013-1023, 2016.

[91] H. Schwenke, W. Knapp, H. Haitjema, A. Weckenmann, R. Schmitt, and F. Delbressine, "Geometric error measurement and compensation of machines—An update," *CIRP Annals,* vol. 57, pp. 660-675, 2008.

[92] S. Sartori and G. X. Zhang, "Geometric Error Measurement and Compensation of Machines," *CIRP Annals*, vol. 44, pp. 599-609, 1995.

[93] F. Zheng, Q. Feng, B. Zhang, and J. Li, "A Method for Simultaneously Measuring 6DOF Geometric Motion Errors of Linear and Rotary Axes Using Lasers," *Sensors*, vol. 19, p. 1764, 2019.

[94] JCGM, "ISO 230-4 ; Test code for machine tools — Part 4: Circular tests for numerically controlled machine tools.," ed: Geneva: ISO, 2005.

[95] N. Zimmermann and S. Ibaraki, "Self-calibration of rotary axis and linear axes error motions by an automated on-machine probing test cycle," *The International Journal of Advanced Manufacturing Technology*, vol. 107, pp. 2107-2120, 2020.

[96] M. Nara, M. Abbe, and K. Takamasu, "Uncertainty Estimation Using Monte-Carlo Method Constrained by Correlations of the Data," *Key Engineering Materials*, vol. 381-382, pp. 587-590, 2008.

[97] H. Li, X. Chen, Y. Cheng, H. Liu, H. Wang, Z. Cheng, *et al.*, "Uncertainty Modeling and Evaluation of CMM Task Oriented Measurement Based on SVCMM," *Measurement Science Review*, vol. 17, 2017.

[98] D. Heiβelmann, M. Franke, K. Rost, K. Wendt, T. Kistner, and C. Schwehn, "Determination of measurement uncertainty by Monte Carlo simulation," in *Advanced Mathematical and Computational Tools in Metrology and Testing XI*, ed: World Scientific, 2018, pp. 192-202.

[99] B. Štrbac, B. Ačko, S. Havrlišan, I. Matin, B. Savković, and M. Hadžistević, "Investigation of the effect of temperature and other significant factors on systematic error and measurement uncertainty in CMM measurements by applying design of experiments," *Measurement*, vol. 158, p. 107692, 2020.

[100] M. Slamani, R. Mayer, M. Balazinski, S. H. H. Zargarbashi, S. Engin, and C. Lartigue, "Dynamic and geometric error assessment of an XYC axis subset on five-axis high-speed machine tools using programmed end point constraint measurements," *The International Journal of Advanced Manufacturing Technology*, vol. 50, pp. 1063-1073, 2010.

[101] J. Nocedal and S. Wright, *Numerical optimization*: Springer Science & Business Media, 2006.

[102] JCGM, "ISO 230-1: 2012. Test code for machine tools-Part 1: Geometric accuracy of machines operating under no-load or quasi-static conditions," ed, 2012.

[103] S. Sepahi-Boroujeni, J. R. R. Mayer, and F. Khameneifar, "Repeatability of on-machine probing by a five-axis machine tool," *International Journal of Machine Tools and Manufacture*, vol. 152, p. 103544, 2020.

[104] D. Hajdu, F. Borgioli, W. Michiels, T. Insperger, and G. Stepan, "Robust stability of milling operations based on pseudospectral approach," *International Journal of Machine Tools and Manufacture,* vol. 149, p. 103516, 2020.

[105] E. Mizrachi, S. Basovich, and S. Arogeti, "Robust time-delayed H∞ synthesis for active control of chatter in internal turning," *International Journal of Machine Tools and Manufacture,* vol. 158, p. 103612, 2020.

[106] G. Totis and M. Sortino, "Polynomial Chaos-Kriging approaches for an efficient probabilistic chatter prediction in milling," *International Journal of Machine Tools and Manufacture,* vol. 157, p. 103610, 2020.

[107] S. Ibaraki and R. Okumura, "A machining test to evaluate thermal influence on the kinematics of a five-axis machine tool," *International Journal of Machine Tools and Manufacture,* vol. 163, p. 103702, 2021.

[108] M. Deng, H. Li, S. Xiang, P. Liu, X. Feng, Z. Du, *et al.*, "Geometric errors identification considering rigid-body motion constraint for rotary axis of multi-axis machine tool using a tracking interferometer," *International Journal of Machine Tools and Manufacture,* vol. 158, p. 103625, 2020.

[109] Y. B. Huang, K. C. Fan, Z. F. Lou, and W. Sun, "A novel modeling of volumetric errors of three-axis machine tools based on Abbe and Bryan principles," *International Journal of Machine Tools and Manufacture,* vol. 151, p. 103527, 2020.

[110] S. Shi, H. Zhang, J. Qu, G. Jin, R. Kuschmierz, and J. Czarske, "Measurement uncertainty propagation in spindle error separation techniques - Investigation by means of stochastic spectral method," *International Journal of Machine Tools and Manufacture,* vol. 141, pp. 36-45, 2019.

[111] P. Fernandez-Zelaia and S. N. Melkote, "Statistical calibration and uncertainty quantification of complex machining computer models," *International Journal of Machine Tools and Manufacture,* vol. 136, pp. 45-61, 2019.

[112] M. Mussatayev, M. Huang, and S. Beshleyev, "Thermal influences as an uncertainty contributor of the coordinate measuring machine (CMM)," *The International Journal of Advanced Manufacturing Technology,* vol. 111, pp. 537-547, 2020.

[113] W. Harmatys, A. Gąska, P. Gąska, M. Gruza, and J. Sładek, "Impact of warm-up period on optical coordinate measuring machine measurement accuracy," *Measurement,* vol. 172, p. 108913, 2021.

[114] P. Gąska, A. Gąska, J. Sładek, and J. Jędrzejewski, "Simulation model for uncertainty estimation of measurements performed on five-axis measuring systems," *The International Journal of Advanced Manufacturing Technology,* vol. 104, pp. 4685-4696, 2019.

[115] S. Sepahi-Boroujeni, J. R. R. Mayer, and F. Khameneifar, "Efficient uncertainty estimation of indirectly measured geometric errors of five-axis machine tools via Monte-Carlo validated GUM framework," *Precision Engineering*, vol. 67, pp. 160-171, 2021.

[116] W. H. Greene, *Econometric Analysis*: Pearson/Prentice Hall, 2008.

[117] JCGM, "ISO 10360-12:2016. Geometrical product specifications (GPS) — Acceptance and reverification tests for coordinate measuring systems (CMS) — Part 12: Articulated arm coordinate measurement machines (CMM)," ed, 2016.

[118] S. Wang, B. Cheung, and M. Ren, "Uncertainty analysis of a fiducial-aided calibration and positioning system for precision manufacturing of optical freeform optics," *Measurement Science and Technology*, vol. 31, p. 065012, 2020.